Report No. K-TRAN: KU-19-4 ▪ FINAL REPORT ▪ March 2023

Field Monitoring of Wicking Geotextile for Moisture Reduction in Pavements

Jie Han, Ph.D., P.E.
Hao Liu, Ph.D.
Mahdi Al-Naddaf, Ph.D.
Robert L. Parsons, Ph.D., P.E.
Jamal Ismail Kakrasul, Ph.D.

The University of Kansas

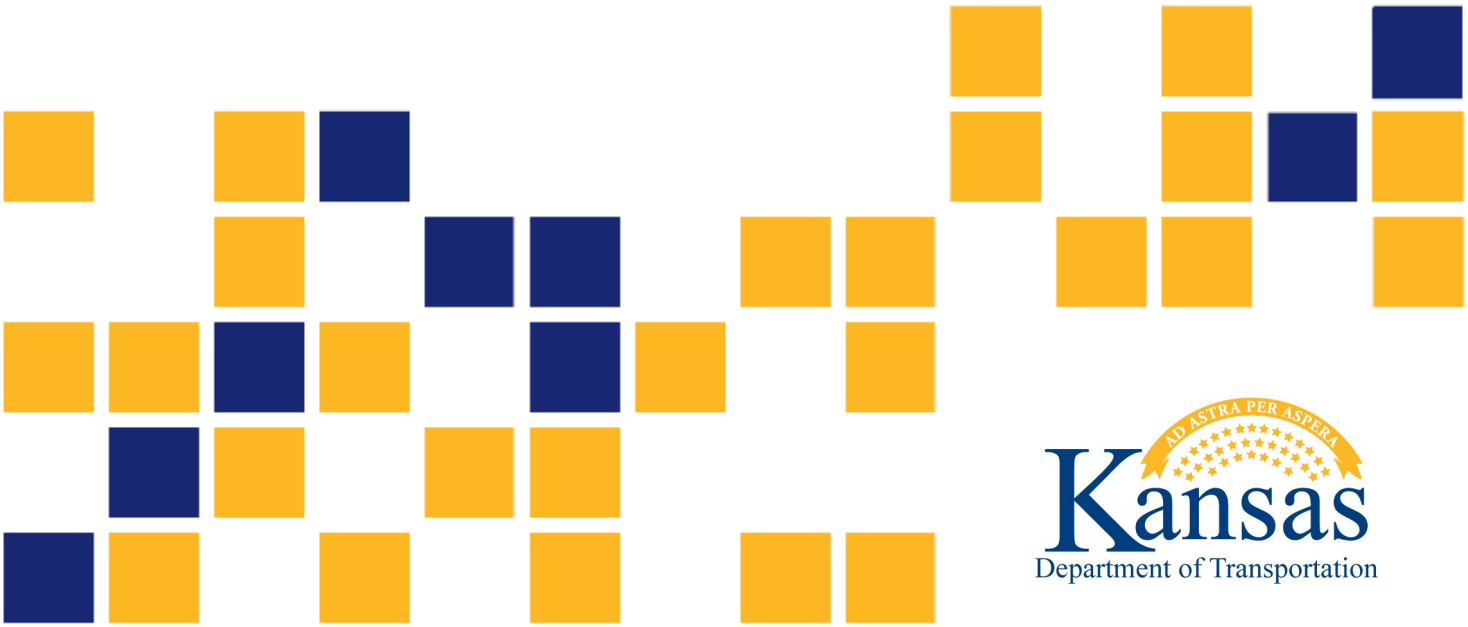

Kansas Department of Transportation

1 Report No. K-TRAN: KU-19-4	**2 Government Accession No.**	**3 Recipient Catalog No.**
4 Title and Subtitle Field Monitoring of Wicking Geotextile for Moisture Reduction in Pavements		**5 Report Date** March 2023 **6 Performing Organization Code**
7 Author(s) Jie Han, Ph.D., P.E.; Hao Liu, Ph.D.; Mahdi Al-Naddaf, Ph.D.; Robert L. Parsons, Ph.D., P.E.; Jamal Ismail Kakrasul, Ph.D.		**8 Performing Organization Report No.**
9 Performing Organization Name and Address The University of Kansas Department of Civil, Environmental & Architectural Engineering 1530 West 15th St Lawrence, Kansas 66045-7609		**10 Work Unit No. (TRAIS)** **11 Contract or Grant No.** C2125
12 Sponsoring Agency Name and Address Kansas Department of Transportation Bureau of Research 2300 SW Van Buren Topeka, Kansas 66611-1195		**13 Type of Report and Period Covered** Final Report June 2018–May 2021 **14 Sponsoring Agency Code** RE-0755-01
15 Supplementary Notes For more information write to address in block 9.		

16 Abstract

Water is often detrimental to the performance of pavements since it reduces soil strength and modulus and provides sources for erosion and freeze-thaw of base courses and subgrade. A common approach to removing water within pavements is to provide a drainage system, which is effective only when the soil beneath the pavement is saturated or nearly saturated and water drains out under a hydraulic gradient. However, a majority of subgrade soils and aggregate bases beneath pavements are unsaturated during their service life. Therefore, the traditional drainage method becomes ineffective in removing water from pavements under undrained conditions. A wicking geotextile product available in the market that includes wicking fibers has been proven effective in removing water under both saturated and unsaturated conditions due to its wicking ability in limited laboratory tests and field projects.

The field study in this project consisted of three sections with tests designed to answer the following:

1. Whether the wicking geotextile can replace cement treatment of the natural subgrade to minimize capillary rise,
2. Whether the wicking geotextile can maintain low water content in the aggregate base, and
3. Whether the aggregate type affects the effectiveness of the wicking geotextile.

To evaluate the effectiveness of the wicking geotextile, moisture sensors were installed in these three sections to monitor their water content changes for two and a half years. The monitoring data showed that the wicking geotextiles with the natural subgrade was more effective to remove water from the aggregate base than the non-woven geotextile with the cement-treated subgrade and maintain the aggregate base at a low water content during the dry period. The wicking geotextile could not stop the rise of the groundwater table and was not effective in performing the wicking function when the groundwater table was above the wicking geotextile; however, it became effective when the groundwater table was below the wicking geotextile. Further verification of its effectiveness to reduce water contents of soils in concrete pavements in the field is necessary before its widespread applications.

17 Key Words Geosynthetics, Geotextiles, Capillary Water, Subgrade (Pavements), Infiltration		**18 Distribution Statement** No restrictions. This document is available to the public through the National Technical Information Service www.ntis.gov.	
19 Security Classification (of this report) Unclassified	**20 Security Classification (of this page)** Unclassified	**21 No. of pages** 113	**22 Price**

Form DOT F 1700.7 (8-72)

This page intentionally left blank.

Field Monitoring of Wicking Geotextile for Moisture Reduction in Pavements

Final Report

Prepared by

Jie Han, Ph.D., P.E.
Hao Liu, Ph.D.
Mahdi Al-Naddaf, Ph.D.
Robert L. Parsons, Ph.D., P.E.
Jamal Ismail Kakrasul, Ph.D.

The University of Kansas

A Report on Research Sponsored by

THE KANSAS DEPARTMENT OF TRANSPORTATION
TOPEKA, KANSAS

and

THE UNIVERSITY OF KANSAS
LAWRENCE, KANSAS

March 2023

PREFACE

The Kansas Department of Transportation's (KDOT) Kansas Transportation Research and New-Developments (K-TRAN) Research Program funded this research project. It is an ongoing, cooperative, and comprehensive research program addressing transportation needs of the state of Kansas utilizing academic and research resources from KDOT, Kansas State University and the University of Kansas. Transportation professionals in KDOT and the universities jointly develop the projects included in the research program.

NOTICE

The authors and the state of Kansas do not endorse products or manufacturers. Trade and manufacturers names appear herein solely because they are considered essential to the object of this report.

This information is available in alternative accessible formats. To obtain an alternative format, contact the Office of Public Affairs, Kansas Department of Transportation, 700 SW Harrison, 2nd Floor – West Wing, Topeka, Kansas 66603-3745 or phone (785) 296-3585 (Voice) (TDD).

DISCLAIMER

The contents of this report reflect the views of the authors who are responsible for the facts and accuracy of the data presented herein. The contents do not necessarily reflect the views or the policies of the state of Kansas. This report does not constitute a standard, specification, or regulation.

Abstract

Water is often detrimental to the performance of pavements since it reduces soil strength and modulus and provides sources for erosion and freeze-thaw of base courses and subgrade. A common approach to removing water within pavements is to provide a drainage system, which is effective only when the soil beneath the pavement is saturated or nearly saturated and water drains out under a hydraulic gradient. However, a majority of subgrade soils and aggregate bases beneath pavements are unsaturated during their service life. Therefore, the traditional drainage method becomes ineffective in removing water from pavements under undrained conditions. A wicking geotextile product available in the market that includes wicking fibers has been proven effective in removing water under both saturated and unsaturated conditions due to its wicking ability in limited laboratory tests and field projects.

The field study in this project consisted of three sections with tests designed to answer the following:

1. Whether the wicking geotextile can replace cement treatment of the natural subgrade to minimize capillary rise,
2. Whether the wicking geotextile can maintain low water content in the aggregate base, and
3. Whether the aggregate type affects the effectiveness of the wicking geotextile.

To evaluate the effectiveness of the wicking geotextile, moisture sensors were installed in these three sections to monitor their water content changes for two and a half years. The monitoring data showed that the wicking geotextiles with the natural subgrade was more effective to remove water from the aggregate base than the non-woven geotextile with the cement-treated subgrade and maintain the aggregate base at a low water content during the dry period. The wicking geotextile could not stop the rise of the groundwater table and was not effective in performing the wicking function when the groundwater table was above the wicking geotextile; however, it became effective when the groundwater table was below the wicking geotextile. Further verification of its effectiveness to reduce water contents of soils in concrete pavements in the field is necessary before its widespread applications.

Acknowledgments

This research project was financially sponsored by the Kansas Department of Transportation (KDOT) through the Kansas Transportation Research and New-Developments (K-TRAN) Program. Mr. Luke Metheny, Chief Geotechnical Engineer, KDOT Bureau of Structures & Geotechnical Services, and Mr. Ryan Barrett, formerly Pavement Design Leader, KDOT Bureau of Road Design, were the monitors for this project. Mr. Steve Gibson, formerly KDOT District 4 Field Engineer, provided great coordination and support for this field study. Former Ph.D. students: Dr. Saif Mohammed Jawad, Dr. Tanya Nicole Walkenbach, and Dr. S. Mustapha Rahmaninezhad, former M.S. students: Zexia Li and Md Rejwanur Rahman, and current Ph.D. student: Md Wasif Zaman, from the Civil, Environmental & Architectural Engineering (CEAE) Department at the University of Kansas provided their assistance in installing moisture sensors, performing field tests, and collecting field data. All the above support and assistance are greatly appreciated.

Table of Contents

Abstract v
Acknowledgments vi
Table of Contents vii
List of Tables ix
List of Figures x
Chapter 1: Introduction x
1.1 Background 1
1.2 Problem Statement 1
1.3 Research Objectives 2
1.4 Research Methodology 3
1.5 Report Organization 3
Chapter 2: Literature Review 4
2.1 Introduction 4
2.2 Detrimental Effects of Water in Pavements 4
2.2.1 Sources of Water 4
2.2.2 Pavement Distresses 5
2.3 Wicking Geotextile 7
2.3.1 Product 7
2.3.2 Laboratory Evaluation 8
2.3.3 Applications 11
2.3.3.1 Daniel Boone Bridge, Missouri 12
2.3.3.2 Garwood Railroad Siding, Idaho 13
2.3.3.3 Pioneer Mountain Scenic Byway, Montana 13
2.3.3.4 State Highway 21, Texas 14
2.3.3.5 State Route 12, California 14
2.3.3.6 Dalton Highway, Alaska 15
2.3.3.7 I-44 Highway, Missouri 15
Chapter 3: Test Sections and Instrumentation 16
3.1 Introduction 16
3.2 Project Information 16
3.2.1 Background 16
3.2.2 Test Sections 17

3.3 Instrumentation 19
3.3.1 Test Section I 19
3.3.2 Test Section II 21
3.3.3 Test Section III 23
3.3.4 Sensor Installation and Datalogger 23
3.4 Construction of Test Sections 25
Chapter 4: Laboratory and Field Material Evaluations 28
4.1 Introduction 28
4.2 Laboratory Tests 28
4.3 Field Tests 31
4.3.1 Nuclear Gauge Test 31
4.3.2 Lightweight Deflectometer Test 33
4.3.3 Dynamic Cone Penetration Test 34
Chapter 5: Monitoring Data and Analysis 39
5.1 Introduction 39
5.2 Weather Condition 39
5.3 Temperature Variations in Pavement 42
5.3.1 Hot Air Temperature Condition 43
5.3.2 Cold Air Temperature Condition 48
5.4 Water Content Variations in Pavement 52
5.4.1 Causes for Water Content Variations 52
5.4.2 Short-term Performance of the Wicking Geotextile 54
5.4.2.1 During and Right after Pavement Construction 54
5.4.2.2 Continuous and Heavy Precipitations 62
5.4.2.3 Snowfall and Snow Melting 71
5.4.3 Long-term Performance of Wicking Geotextile 79
Chapter 6: Conclusions and Recommendations 92
6.1 Conclusions 92
6.2 Recommendations 95
References 96

List of Tables

Table 2.1: Asphalt Pavement Distresses and Their Groups 6
Table 2.2: Properties of the Wicking Geotextile 8
Table 2.3: Applications of Wicking Geotextile in Pavements 12
Table 3.1: International Roughness Index (IRI) before Construction 16
Table 3.2: Gradation and Atterberg Limits of AB-1 and AB-3 18
Table 3.3: Properties of the AB-3 Aggregate 18
Table 3.4: Sensor Label, Location, and Material in Section I 22
Table 3.5: Sensor Label, Location, and Material in Section II 23
Table 3.6: Timeline for Pavement Construction 26
Table 4.1: Results of Atterberg Limit Tests 29
Table 4.2: Results of Nuclear Gauge Tests 32
Table 4.3: Results of LWD Tests 34
Table 4.4: DPI from the DCP Tests 38
Table 4.5: California Bearing Ratio (%) of the Subgrade Soil and the Aggregate Bases 38
Table 4.6: Elastic Modulus (psi) of the Subgrade Soil and the Base Material 38
Table 5.1: Weather Condition for the Days with Daily Precipitation Heavier than 1 inch 41

List of Figures

Figure 2.1: Sources of Water 5
Figure 2.2: Cross-Sections of Fibers in Geotextiles 8
Figure 2.3: New Drainage Design Concept for Pavement Structure 11
Figure 3.1: Test Sections on the US-169, Allen County, KS 17
Figure 3.2: Joints of the Pavement Section 19
Figure 3.3: Sensors in Section I 21
Figure 3.4: Sensors at Section II 22
Figure 3.5: Sensor and Data Collection System 24
Figure 3.6: Construction of the Test Section 25
Figure 3.7: Construction of the Concrete Pavement 26
Figure 3.8: Road Condition on April 1st, 2021 (after approximately two years of being open to traffic) 27
Figure 4.1: Sieve Analysis Results 29
Figure 4.2: Proctor Compaction and CBR Test Results of the Subgrade Soil 30
Figure 4.3: Proctor Compaction and CBR Test Results of the Base Materials 30
Figure 4.4: Locations of Field Tests in Each Section 31
Figure 4.5: DCP Test Results for the Subgrade Soil in Section III 36
Figure 4.6: DCP Test Results for the AB-1 Aggregate Bases in Section I and Section II 36
Figure 4.7: DCP Test Results for the AB-3 Aggregate Base in Section III 37
Figure 5.1: Weather Condition in Humboldt, KS from July 2017 to March 2021 40
Figure 5.2: Variations of Air and Pavement Temperatures from July 2018 to March 2021 43
Figure 5.3: Air and Soil Surface Temperatures in July 2019 44
Figure 5.4: Temperature Readings from the Sensors in July 2019 45
Figure 5.5: Change of Temperature Readings at Different Distances in Section III 46
Figure 5.6: Change of Temperature Readings at Different Distances from Transverse Joint in Section III 47
Figure 5.7: Temperature Distributions in the Pavement Sections at 12 p.m. on July 20th, 2019 47
Figure 5.8: Air Temperature and Temperature under the Soil Surface in February 2021 48
Figure 5.9: Temperature Readings of the Sensors in the Three Sections 50
Figure 5.10: Temperature Variations with Depths in Section III during February 2021 50

Figure 5.11: Temperature Variations with Distances from the Transverse Joint in Section III during February 2021 51
Figure 5.12: Temperature Distributions in the Pavement at 12 p.m. on February 15th, 2021 52
Figure 5.13: Cross Sections and Sensors in the Pavement Sections 53
Figure 5.14: Weather Condition from July 24th to December 1st, 2018 55
Figure 5.15: VWC Readings in Section I from July 24th to December 1st, 2018 56
Figure 5.16: VWC Readings in Section II from July 24th to December 1st, 2018 59
Figure 5.17: The VWC Readings in Section III for July 31st to December 1st, 2018 60
Figure 5.18: VWC Readings in the Three Sections from July 24th to December 1st, 2018 62
Figure 5.19: Weather Condition from May 18th to June 21st, 2019 63
Figure 5.20: VWC and Temperature Readings of the Sensor under the Soil Surface 64
Figure 5.21: VWC Changes in Section I from May 18th to June 22nd, 2019 65
Figure 5.22: VWC Changes in Section II from May 18th to June 22nd, 2019 67
Figure 5.23: VWC Changes in Section III from May 18th to June 22nd, 2019 69
Figure 5.24: VWC Readings in the Three Sections from May 18th to June 23rd, 2019 70
Figure 5.25: Weather Condition from January 26th to March 11th, 2021 71
Figure 5.26: VWC and Temperature Readings of the Sensor under the Soil Surface from January 26th to March 11th, 2021 73
Figure 5.27: VWC Readings in Section I from January 26th to March 10th, 2021 73
Figure 5.28: VWC Reading Changes in Section II from January 26th to March 11th, 2021 75
Figure 5.29: VWC Readings in Section III from January 26th to March 11th, 2021 76
Figure 5.30: Comparison of the VWC Readings in the Three Sections from January 26th to March 11th, 2021 78
Figure 5.31: VWC Readings of the Sensors under the Soil Surface from December 2018 to March 2021 79
Figure 5.32: VWC Readings of Sensors in Section I from December 2018 to March 2021 82
Figure 5.33: VWC Readings of Sensors in Section II from December 2018 to March 2021 86
Figure 5.34: VWC Readings of Sensors in Section III from December 2018 to March 2021 89

Chapter 1: Introduction

1.1 Background

Water is well recognized as one of the main factors causing pavement distresses. Water can come into the pavement system in different ways, for example: infiltration, capillary rise, and seepage. Infiltration often occurs through joints and existing cracks on pavements after rainfalls. Capillary rise happens when there is a high groundwater table and a high percentage of fines in a base course and/or subgrade. Seepage water may enter the pavement system from side slopes. An increase of water content in the base course and/or the subgrade reduces their strengths and resilient moduli, thus accelerating the deterioration of the pavement. Excessive water in the base course and the subgrade promotes migration or erosion of fines from these layers under traffic loading and/or freeze-thaw problems during winter and spring. As a result, the pavement may lose foundation support so that permanent deformations and cracks develop during the service time. Several measures have been used in the practice to mitigate these problems, including but not limited to: pavement sloping and joint/crack sealing to prevent water infiltration due to precipitations; installation of open-graded aggregate and geocomposite drainage layers to remove water from the pavement system; chemical treatment of base and subgrade; and lowering of groundwater table. The traditional drainage method relies on gravitational drainage that is effective under a saturated or nearly saturated condition. However, base courses and subgrade are often unsaturated during the pavement service, especially during dry periods; therefore, the traditional drainage system may not be effective in removing excessive water when the soil becomes unsaturated.

1.2 Problem Statement

A manufacturer's developed geosynthetic product (also called a wicking geotextile) has been introduced into the market and used in Alaska, Wisconsin, Missouri, and other states to effectively solve freeze-thaw problems in aggregate bases in pavements. Limited studies have been done on the use of this product in rigid pavements; therefore, it is important to verify its effectiveness to reduce water contents of soils in concrete pavements in the field. In the past, the research team at the University of Kansas has conducted a series of laboratory tests to evaluate the

effectiveness of the wicking geotextile to remove water from the Kansas aggregate base material (specifically the AB-3 aggregate) (Guo, Wang, Zhang, & Han, 2017; Han, Zhang, & Guo, 2017). The test results verified the effectiveness of the wicking geotextile in reducing water content in aggregate base. The aggregate bases with water content reduction by the wicking geotextile performed much better than those without the water content reduction in terms of base course deformations under cyclic plate loading (Guo, Han, Zhang, & Li, 2021). Other researchers have also conducted laboratory tests (Lin and Zhang, 2018; Lin, Zhang, & Han, 2019) and limited field studies (Connor & Zhang, 2015) to evaluate the effectiveness of this wicking geotextile. Zornberg, Azevedo, Sikkema, and Odgers (2017) and Han, Zhang, and Guo (2017) provided summaries of the use of the wicking geotextile for roadway applications. Most of the above studies were focused on the use of the wicking geotextile in unpaved and asphalt paved roads. Before this product is widely used in actual projects for moisture reduction of subgrade soil and aggregate base, the Kansas Department of Transportation (KDOT) decided to use this wicking geotextile as a field trial in the re-construction of concrete pavements on the US-169 Highway in Allen County, Kansas. There was a need for field monitoring and evaluation of test sections with the wicking geotextile to verify its performance and benefits in moisture reduction in pavements.

1.3 Research Objectives

The objective of this research was to verify the effectiveness of the wicking geotextile to minimize capillary rise and reduce water content in concrete pavements in the field with high groundwater tables. The test sections for the field trial were designed to answer three important questions: whether the wicking geotextile can replace cement treatment of the natural subgrade; whether the wicking geotextile can maintain low water content in the aggregate base; and whether the aggregate type affects the effectiveness of the wicking geotextile. To answer these questions, moisture sensors were installed in the test sections to monitor the water content changes during the two and a half year monitoring period.

1.4 Research Methodology

The field study consisted of three test sections:

Section I - a wicking geotextile layer was placed at the interface between the natural (untreated) subgrade and the aggregate base – AB-1;

Section II - a non-woven geotextile layer was placed at the interface between the cement-treated subgrade and the aggregate base – AB-1; and

Section III - a wicking geotextile layer was placed at the interface between the natural (untreated) subgrade and the aggregate base AB-3. Both AB-1 and AB-3 are commonly used by KDOT as aggregate base materials, but the AB-3 aggregate had more fine particles than the AB-1 aggregate.

During construction, subgrade soil and base course materials were sampled and nuclear gauge tests, dynamic cone penetration (DCP) tests, and lightweight deflectometer (LWD) tests were performed to evaluate the density and stiffness of the subgrade and the base course. Moisture sensors with temperature measurement were installed in the subgrade and/or base course in these test sections and monitored for two and a half years. The collected data were used to evaluate the performance of the wicking geotextile in moisture reduction in concrete pavements.

1.5 Report Organization

This report includes six chapters. Chapter 1 presents a brief introduction to this study, which comprises background, problem statement, research objective, research methodology, and report organization. Chapter 2 provides a literature review on past research work related to this study, which includes detrimental effects of water on pavement structures, laboratory tests evaluating the characteristics and wicking ability of the wicking geotextile, and applications of the wicking geotextile in several field projects to mitigate water-induced problems. Chapter 3 describes the pavement construction, field testing, and instrumentation. Chapter 4 presents the results from laboratory and field tests of the base materials and the subgrade soil. Chapter 5 presents and analyzes the monitoring data of temperature and volumetric water contents from the sensors in the test sections. Chapter 6 presents the conclusions and recommendations based on the test results and analyses.

Chapter 2: Literature Review

2.1 Introduction

It is well known that water adversely affects pavement performance. Water can enter pavement structures through water infiltration into existing joints and cracks, capillary rise from a high groundwater table, seepage from side slopes, and freeze-thaw cycles. Different types of drainage measures are adopted in the practice to mitigate water-related problems including the use of the wicking geotextile in recent years. This chapter first reviews the detrimental effects of water in pavements, discusses the traditional drainage measures and their drawbacks, and then focuses on the wicking geotextile including the characteristics and laboratory evaluation of the wicking geotextile and its applications for mitigating water-induced problems in actual projects.

2.2 Detrimental Effects of Water in Pavements

2.2.1 Sources of Water

Figure 2.1 shows that water may enter a pavement system in different ways: infiltration, rise of the groundwater table, seepage from higher ground, capillary action, and vapor movement (FHWA, 1992). Water from a precipitation may infiltrate into the pavement system through joints and existing cracks in the pavement and unpaved shoulders or side slopes. Precipitations include rainfalls and snowfalls. Snow after melting becomes water that can also become a source for water infiltration. FHWA (1992) considered water infiltration to be the major water source for pavements. Groundwater table varies with precipitations and a high level of water table can submerge subgrade and/or base courses. When a soil contains fines or fine particles, capillary forces may develop and suck water upward from the water table. When excessive water remains in the soil, it may be frozen in winter, thus inducing frost heave that causes damage to pavements. Temperature difference within the pavement system may induce vapor movement and water accumulation below the pavement surface. Four forms of water including vapor, bounded water, capillary water, and gravitational water exist in the pavement system (Guo, 2017). Vapor and bounded water are hard to be removed from the soil; therefore, they are often treated as part of the soil. The height of

capillary water rise depends on the effective pore size of the soil. The most common form of water in the pavement system is gravitational water, which obeys Darcy's Law when saturated.

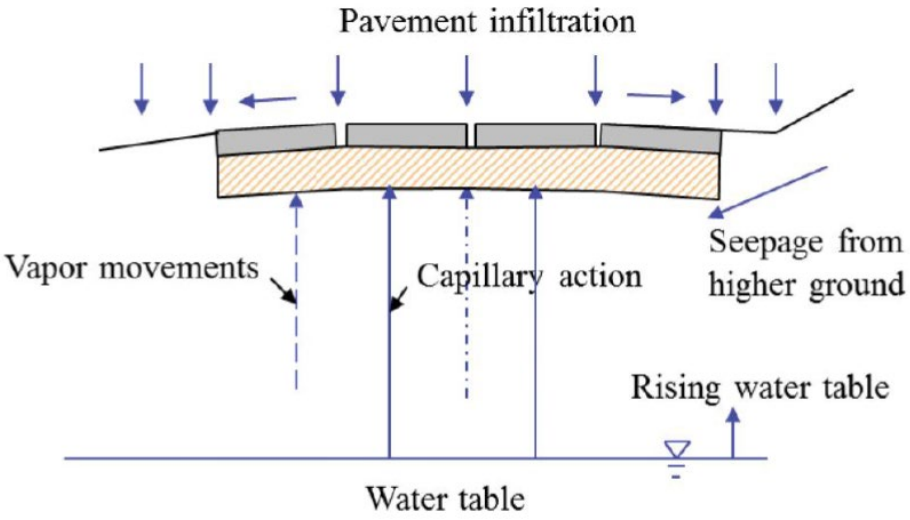

Figure 2.1: Sources of Water
Source: FHWA (1992)

2.2.2 Pavement Distresses

Pavement distresses depend on pavement type. For asphalt pavements, the distresses can be grouped into four categories: cracking, viscoplastic deformations, surface defects, and miscellaneous distresses (Shahin, 1994; ASTM, 2018; Miller & Bellinger, 2014; Ragnoli, De Blasiis, & Di Benedetto, 2018). Table 2.1 lists the asphalt pavement distresses in these four groups. The National Cooperative Highway Research Program (NCHRP, 2004) indicated that some surface deformations of asphalt pavements including bump, striping, rutting, potholes, and some fatigue and slippage cracking are water-related issues. Water also contributes to some surface deformations of concrete pavements including diagonal, transverse, and longitudinal cracking. Although not all the pavement distresses are caused by water, the existence of water exacerbates the pavement distresses (Rokade, Agarwal, & Shrivastava, 2012). Han (2015) concluded that the detrimental effects of water on pavement structures include reduction in geomaterial strength and stiffness, expansion of geomaterial, erosion of soil particles and rock, migration of fines, freeze-thaw, stripping of asphalt mixture, and durability cracking of concrete.

Table 2.1: Asphalt Pavement Distresses and Their Groups

#	Cracking	Viscoplastic deformations	Surface deflects	Miscellaneous distresses
1	Fatigue cracking	Bumps and sags	Bleeding	Patching-utility cut patching
2	Block cracking	Rutting	Polished aggregate	Railroad crossing
3	Edge cracking	Corrugations	Raveling	Manhole
4	Longitudinal and transverse cracking	Depressions		
5	Joint reflective cracking	Potholes		
6	Slippage cracking	Swell		
7		Lane/shoulder drop off		
8		Shoving		

Pavement design methods including the 1993 AASHTO Pavement Design Guide and the AASHTO Mechanistic-Empirical Pavement Design Guide (NCHRP, 2004) consider adverse effects of water on the performance of pavement structures. In the 1993 AASHTO Pavement Design Guide, seasonally-dependent (also water-dependent) resilient moduli of a soil are used to estimate an equivalent resilient modulus based on accumulated damages over a one-year period. The 1993 AASHTO Pavement Design Guide also considers the water effect through a drainage coefficient for both asphalt and concrete pavements and loss of support for concrete pavements. The AASHTO Mechanistic-Empirical Pavement Design Guide considers water effects through the enhanced integrated climatic model including rainfall and groundwater table.

It is well known that water plays a critical role in pavement performance and causes or exacerbates pavement distresses if not properly handled. Different measures have been taken during pavement design and/or maintenance: to prevent or minimize water from entering the pavement system (e.g., joint and crack sealing, sloping pavement surface, trench, dewatering, and geomembrane barrier); to remove water entering the pavement system (e.g., subsurface granular and geocomposite drains); and to use materials insensitive to water (e.g., asphalt treated base, cement treated base, and aggregate with small fines content) (NCHRP, 2004; FHWA, 1992; and AASHTO, 1993). However, traditional subsurface drainage systems including longitudinal drains, transverse and horizontal drains, drainage blankets, and well systems are only effective in removing gravitational water following Darcy's Law under saturated or nearly saturated conditions.

They are not effective in removing excessive water in soils under unsaturated conditions or stopping capillary rise of water from a groundwater table. Under certain situations, excessive water is still problematic to pavement performance, for example, freeze-thaw problems. Therefore, a more effective way is needed to overcome these problems. Wicking geotextile, as discussed in the next section, may fulfill this need.

2.3 Wicking Geotextile

2.3.1 Product

The wicking geotextile available in the market contains high modulus polypropylene yarns and deep-grooved nylon wicking yarns (i.e., 4DG^{TM} fibers). The wicking fiber has a specific surface area of 1782 ft^2/lb (0.365 m^2/g) and the wicking geotextile has a permittivity of 0.24 s^{-1} (Connor & Zhang, 2015). Figure 2.2 shows the magnified views of a typical monofilament non-woven geotextile and the wicking geotextile. Clearly the grooved fiber in the wicking geotextile has a much larger surface area than the regular fiber in the non-woven geotextile. The large surface area and the small channels on the wicking fiber can develop large surface tension when the fiber is in contact with water. This surface tension can suck water into the channels. It is known that the non-woven geotextile is a good drainage material under a saturated condition; however, the wicking geotextile is a better material to provide drainage under an unsaturated condition. Han and Zhang (2014) and Han et al. (2018) pointed out that deep grooves of approximately 8 μm in diameter in the wicking fiber of the wicking geotextile function as capillary tubes to suck water in unsaturated soils out from the pavement system.

Table 2.2 summarizes the properties of the wicking geotextile currently available in the market. This geotextile has tensile strengths of 480 lb/ft (7.0 kN/m) and 1083 lb/ft (15.8 kN/m) at 2% strain in the machine and cross-machine directions, respectively and its permittivity of 0.4 s^{-1} (corresponds to the flow rate at 4.0 ft^3/min/ft^2 or 1222 L/min/m^2). This table also provides the wet front movements horizontally and vertically under a laboratory environment with a relative humidity of 50%.

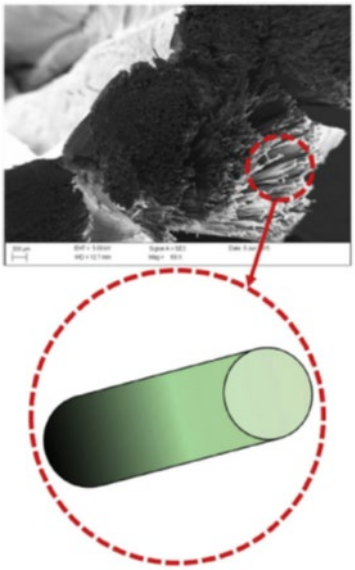

(a) Regular Fiber in a Non-Woven Geotextile

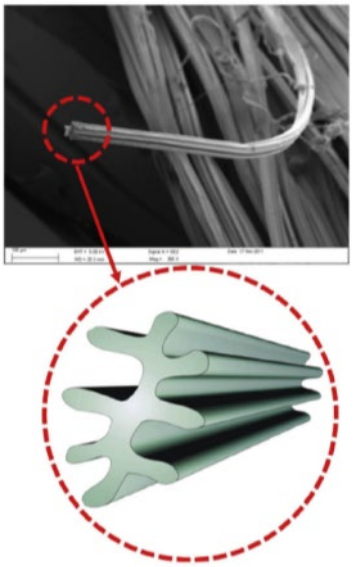

(b) Grooved Fiber in the Wicking Geotextile

Figure 2.2: Cross-Sections of Fibers in Geotextiles

Source: Zornberg et al. (2017)

Table 2.2: Properties of the Wicking Geotextile

Properties	Unit	Minimum average roll value	
		MD	CD
Tensile strength (2% strain)	lb/ft	480	1083
Flow rate	$ft^3/min/ft^2$	4.0	
Permittivity	sec^{-1}	0.4	
Pore size (O_{50})	in	0.00335	
Pore size (O_{95})	in	0.00768	
Apparent opening size (AOS)	in	0.0167	
Wet front movement (24 min)	in	6.0 (vertical direction)	
Wet front movement (983 min) zero gradient	in	73.3 (horizontal direction)	

Note: MD=machine direction and CD=cross-machine direction. Source: TenCate (2015)

2.3.2 Laboratory Evaluation

Several laboratory studies have been conducted in the past few years to evaluate the behavior of the wicking geotextile and its interaction with water and soil considering different influence factors. For example, Guo et al. (2017) conducted 12 laboratory tests in a controlled room to investigate the water removal ability of the wicking geotextile in water tanks with sufficient water supply under different temperature and relative humidity conditions. The test

results showed that the wicking geotextile could effectively wick water out of the water tank and its water removal rate increased as the temperature increased but decreased as the relative humidity increased. Wang et al. (2017) investigated the wicking ability of the wicking geotextile placed between an aggregate base and a subgrade soil subjected to rainfall. The test results showed that the removal of water from the soils started with gravitational drainage and then wicking drainage, and the wicking drainage was slower than the gravitational drainage. The test results also showed that the wicking geotextile could even wick water out of the soil when it was prepared at its optimum water content. Wang et al. (2017) found that the amounts of water reduction in the base and subgrade were different at different distances to the geotextile, indicating the wicking geotextile has an influence distance.

Following one of the findings from Wang et al. (2017), the wicking geotextile had an influence distance to wick water out of the soil. Researchers Guo, Han, Zhang, and Li (2019b) conducted the soil column tests to evaluate the effective distance of the wicking geotextile in the AB-3 aggregate base. These soil column tests indicated that the effective wicking zone for the AB- 3 base material ranged from 7 to 10 in. (180 and 250 mm), and the wicking zone increased as the drainage time increased.

Lin et al. (2019) conducted several laboratory tests; specifically, the pressure plate test, the capillary rise test, the modified pressure plate test, the salt concentration test, the large-scale direct shear test, and the constant head test to investigate the behavior of the wicking geotextile and its interaction with soil. Based on the capillary rise, pressure plate, and salt concentration tests, they developed drying Geotextile Water Characteristic Curves (GWCC). The test results showed that the wicking geotextile had a much higher in-plane drying GWCC than the cross-plane GWCC. This indicates that the wicking geotextile has a much higher capacity to hold water under unsaturated conditions in the machine direction than that in the cross-machine direction. In addition, the wicking geotextile could remove the water out of the pavement structure efficiently within a suction pressure range of 0 to 36.8 psi (254 kPa). Lin et al. (2019) also investigated the interaction between the wicking geotextile and the AB-3 aggregate at different water contents using large-scale direct shear tests. They found that the interface frictional angle between the AB- 3 aggregate and the wicking geotextile decreased from 47.5° at the water content of 2% to 39.4° at

the water content of 10.5% with an assumed cohesion of zero. The higher frictional angle was attributed to the higher soil suction at a lower water content, which increased the effective stress on the wicking geotextile. Lin et al. (2019) measured the average in-plane saturated hydraulic conductivity of the wicking geotextile, which was approximately 2.44×10^{-2} in./s (6.2×10^{-4} m/s) using the constant head tests.

Lin and Zhang (2018) conducted the wicking and wetting tests to evaluate the drainage efficiency of the wicking geotextile in different types of soil. They discovered that the wicking geotextile could take advantage of the suction gradient between the two ends of the wicking geotextile to drain both gravitational and capillary water out of the pavement structure. The tests showed that the wicking geotextile could remove capillary water out of the soil with 14.5% fines, even though the drainage process was relatively slow. Lin and Zhang (2018) examined possible clogging effects on the wicking geotextile by collecting the geotextile samples from the field and the laboratory and performing the scanning electron microscope (SEM) tests. The SEM images showed that soil particles floated on the channels of wicking fibers but did not clog the channels.

Since the wicking geotextile can wick water out of a soil under an unsaturated condition, the water content of the soil in the pavement structure is maintained at a relatively low level so that the modulus of the soil is maintained at a relatively high level and the performance of the pavement is improved. Yuan (2017) conducted eight repeated plate loading tests of aggregate bases with the wicking or non-wicking geotextile placed at the bottom of the aggregate base. These tests had four different test conditions: (1) aggregate base compacted at its optimum moisture content, (2) saturated base without drainage, (3) saturated base with drainage, and (4) saturated base with a drainage and freeze-thaw process. The test results showed that both wicking and non-wicking geotextiles effectively reduced the permanent deformations of the bases; moreover, the wicking geotextile-stabilized base courses, after drainage, had smaller displacements than other base courses because the removal of water from the base courses by the wicking geotextile increased the base strength and modulus and minimized the freeze-thaw potential of the bases.

To investigate the effectiveness of the wicking geotextile under the simulated field condition, Guo (2017), Guo, Han, & Zhang (2019a), and Guo et al. (2021) conducted six large-scale cyclic plate loading tests. The six model tests indicated that the wicking geotextile reduced

the water content in the base course during the drying period following the rainfall simulation and reduced the permanent deformation of the modeled road section due to cyclic plate loading. In addition, the effectiveness of the wicking geotextile in reducing the permanent deformation was more significant when the subgrade was weak.

2.3.3 Applications

The wicking geotextile has been used to successfully mitigate water-related pavement problems. This section provides reviews of several field projects involving the wicking geotextile. Figure 2.3 shows a typical pavement section involving the wicking geotextile (Connor & Zhang, 2015). In this cross section, the wicking geotextile is used to stop capillary rise of water from the groundwater table and remove the water infiltrated from the pavement surface. Due to the relative humidity of air lower than that in the wicking geotextile, water evaporates from the surface of the wicking geotextile and water in soil is sucked into the channels of the wicking geotextile and transported to the exposed portion of the geotextile until the suction in the geotextile is the same as that in the soil. As a result, the water content of the soil above and below the wicking geotextile is reduced.

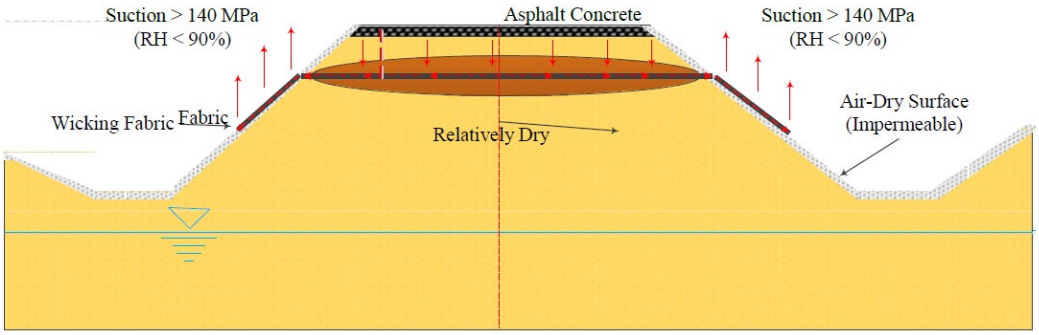

Figure 2.3: New Drainage Design Concept for Pavement Structure
Source: Connor and Zhang (2015)

Table 2.3 lists the field projects in which the wicking geotextile was used. These field projects are discussed in the following section.

Table 2.3: Applications of Wicking Geotextile in Pavements

No.	Reference	Goal	Project Location
1	Azevedo (2016); Zornberg et al. (2017)	To prevent capillary rise of water from high water table	Daniel Boone Bridge, Missouri, USA
2	Azevedo (2016); Zornberg et al. (2017)	To remove infiltration water downward from the surface	Garwood Railroad Siding, Idaho, USA
3	Sikkema and Carpita (2014)	To prevent capillary rise of water from high water table; to prevent frost heave	Pioneer Mountain Scenic Byway, Montana, USA
4	Azevedo (2016); Zornberg et al. (2017)	To minimize pavement damage due to expansive clay subgrade	State Highway 21, Texas, USA
5	Azevedo (2016); Zornberg et al. (2017)	To provide lateral drainage of water from vertical drains for soil improvement	State Route 12, California, USA
6	Zhang, Presler, Li, Jones, & Odgers (2014); Lin, Zhang, & Presler (2015); Lin, Presler, Zhang, Jones, & Odgers (2017)	To remove infiltration water; to prevent capillary rise of water from high water table; to prevent frost boil	Dalton Highway, Alaskan, USA
7	Zhang and Galinmoghadam (2020); Galinmoghadam and Zhang (2020)	To mitigate water pumping	I-44 Highway, Missouri, USA

2.3.3.1 Daniel Boone Bridge, Missouri

The Daniel Boone Bridge built near St. Louis, Missouri in 2013, as reported by Zornberg et al. (2017), was the expansion of an existing bridge constructed along I-64 crossing the Missouri River in the 1930s. The subgrade of the new pavement approaching the Daniel Boone Bridge was nearly saturated due to a high-water table. A 4-in. (100-mm) thick, drainage aggregate layer was required to be placed below the 4-in. (100-mm) thick aggregate base layer to remove the water from the high-water table. To reduce the cost of expensive drainage aggregate, a wicking geotextile was adopted to replace a 2-in. (50-mm) thick drainage aggregate layer. The wicking geotextile also provided separation and stabilized the subgrade. The wicking geotextile was extended to the shoulder of the road and then was covered by aggregate at the edge so that the water in the wicking geotextile was released through evaporation or into a trench drain. After the road was open to the traffic, the new pavement showed good performance; therefore, indicating that the wicking geotextile was a good substitute for the 2-in. (50-mm) thick aggregate drainage layer.

2.3.3.2 Garwood Railroad Siding, Idaho

Zornberg et al. (2017) reported that Garwood Railroad Siding in Idaho was 2.1 miles long and connected to the existing Union Pacific Railroad track through two turnouts. The siding track was supported by a minimum 12-in. (0.30-m) thick ballast on top of a 6-in. (0.15-m) sub-ballast. The geotechnical investigation indicated that the subgrade was a mixture of silty gravel and sand, and the groundwater table was deep. To mitigate the frost heave problem due to water infiltration from the ballast and sub-ballast layers, a wicking geotextile was placed after removing the 6-in. (0.15-m) thick topsoil and then covered by the sub-ballast and ballast gravel layers. The wicking geotextile was extended under the access road and then to the drainage ditch; therefore, the water collected by the siding track could be released into the drainage ditch. Post-construction evaluation showed an excellent early performance, as indicated by the evidence of drainage through the geotextile after one year of service time.

2.3.3.3 Pioneer Mountain Scenic Byway, Montana

The Pioneer Mountain Scenic Byway (a seasonally open road), as reported by Sikkema and Carpita (2014), serves as a connection between Polaris and Wise River, Montana. The most severe freeze-thaw cycles induced a 755 ft (230 m) long and 8 in. (0.2 m) wide longitudinal crack in the Moose Park location. This pavement at the Moose Park location was re-constructed in 2004; specifically, the reconstruction included sub-excavation, placement of a non-wicking geotextile, and installation of a drain system. Unfortunately, the freeze-thaw-induced cracks reappeared in 2008 and developed seasonally from 2009 to 2013. This outcome indicated that the non-wicking geotextile was not effective in stopping capillary rise of water from the groundwater table and mitigating the freeze-thaw problem. In 2013, the Scenic Byway was re-constructed by placing a wicking geotextile layer on top of the subgrade and a non-wicking geotextile layer under the aggregate base. The wicking geotextile was placed to stop the capillary rise of water from the groundwater table; meanwhile, the non-wicking geotextile was placed to provide stabilization of the base course. So far, this design has proved to be effective by mitigating the freeze-thaw problem.

2.3.3.4 State Highway 21, Texas

Pavement performance conducted by TxDOT revealed that 74% of the road on State Highway 21 (just north of Bastrop, TX) had obvious distresses, such as edge cracking, patches, level-ups, and longitudinal cracks within lanes (Zornberg et al., 2017). The site investigation showed that the subgrade soil contained the Montmorillonite mineral and had a plasticity index of 30 to 53 and percent of fines from 73% to 100%, respectively. The distresses were mainly caused by the expansive subgrade. This highway was rehabilitated in 2013 by milling the top 3 in. (76 mm) of pavement surface, partially excavating the outside lane, and widening the shoulder. This field study had different test sections. The cross-section of the re-constructed road included a wicking geotextile layer placed between the subgrade and the base course, and two biaxial geogrid layers within the base course. Moisture sensors installed in the subgrade under the shoulder revealed that the wicking geotextile was effective in generating a uniform distribution of water contents across the pavement section so that differential movement of the subgrade was avoided.

2.3.3.5 State Route 12, California

This project involved a special application of the wicking geotextile (Zornberg et al., 2017). Due to the existence of highly compressible foundation soil, the 4-mile (6.4 km) long segment of State Route 12 (SR12) suffered considerable settlement-related damages, including significant cracking (e.g., longitudinal cracks), edge failure, and excessive roughness. The site investigation revealed that the foundation soil consisted of 4.9-20.0 ft (1.5-6.1 m) thick, soft, to very soft, clayey peat and a 9.8-35.1 ft (3.0-10.7 m) thick clay layer, underlain by a medium-dense to dense, coarse-grained, and silty sand. Prefabricated vertical drains (PVDs) were installed in a triangular pattern with spacing of 5 ft (1.5 m) and to a depth of 61 ft (18.3 m) to accelerate primary and secondary consolidation of the foundation soil under surcharge. The wicking geotextile was placed on the top of PVDs to provide lateral drainage of the water from PVDs. The wicking geotextile also served the functions of separation and subgrade stabilization before placement of the embankment and temporary surcharge.

2.3.3.6 Dalton Highway, Alaska

This is one of the early uses of the wicking geotextile reported by Zhang et al. (2014). As part of the Dalton Highway, an unpaved road on the Beaver Slide was on a side hill. In each spring, groundwater emerging from a shallow depth of the road embankment running down the slope created water-rich soft spots on the road and subsequently caused road distresses due to frost heave and thaw-weakening during the seasonal changes. The cross section of a 61 ft (18.1 m) long test section had two wicking geotextile layers installed to solve the frost boil problem. The lower wicking geotextile was used to stop capillary rise of water from the shallow groundwater while the upper wicking geotextile was used to remove the infiltrating water from the road surface. This road section has been performing well since the re-construction with the wicking geotextiles.

2.3.3.7 I-44 Highway, Missouri

Zhang and Galinmoghadam (2020) reported the use of the wicking geotextile to fix pavement shoulder pumping problems. Water pumping along the joint between the pavement and the shoulder was observed on the eastbound I-44 Highway in Missouri. Large deflection of the pavement, water in the pavement, and material susceptible to pumping are the three necessary conditions for ejection of water and migration of fines (often referred to as pumping) from pavement joints. A segment of the eastbound I-44 Highway was reconstructed by including the wicking geotextile to investigate its effectiveness to mitigate the water pumping problem. The field monitoring data indicated that the wicking geotextile effectively removed water from the pavement section after rainfalls, thus reducing the chance of water pumping.

Chapter 3: Test Sections and Instrumentation

3.1 Introduction

This chapter describes the project information on the re-construction of the concrete pavement on the US-169 Highway in Allen County, Kansas; additionally, it presents three test sections with and without the wicking geotextile. Including the layouts and installation of moisture sensors, this section also discusses the pavement conditions right after the construction and after opening of the pavement to traffic for approximately two years.

3.2 Project Information

3.2.1 Background

U.S. Route 169 (US-169) is a major north–south U.S. Highway that runs from US-64 in Tulsa, Oklahoma to US-53 near Virginia, Minnesota passing through Kansas. The Kansas Department of Transportation (KDOT) pavement management system indicated that the performance of the pavement section in Allen County, Kansas accelerated its deterioration with time as shown in Table 3.1 based on the International Roughness Index (IRI) and other performance indices (not shown). The 7-mile-long U.S. 169 pavement reconstruction project in Allen County began in May 2018 with an entire budget of $16 million. All concrete on the mainline highway pavement and ramps was replaced along with the reestablishment of a new subgrade base for the highway. The deterioration of the pavement was related to a high groundwater table. KDOT decided to use the wicking geotextile in the road reconstruction as a field trial to verify the benefits of the wicking geotextile to mitigate the high groundwater table problems and reduce the water content of the base course in the pavement section. For comparison purposes, three test sections were selected for this research.

Table 3.1: International Roughness Index (IRI) before Construction

Year	2014	2015	2016	2017	2018
IRI (in./mi)	55	68	82	88	119

3.2.2 Test Sections

Figure 3.1 shows the locations of the three test sections (Section I, Section II, and Section III from north to south), which are located between the interchange of the US-169 and Iowa road and the interchange of US-169 and Hawaii Road, near Humboldt, KS. Section II served as the control section with a non-woven geotextile placed between the subgrade and the base course, which was the pavement section used for the reconstruction of the road. Section I and Section III had the wicking geotextile at the interface between the subgrade and the base course. Aggregate base course Class 1 (AB-1) was used as the base material in Section I and Section II while aggregate base course Class 3 (AB-3) was used as the base material in Section III. It should be pointed out that the cross section of Section II was different from that of Section I and Section II.

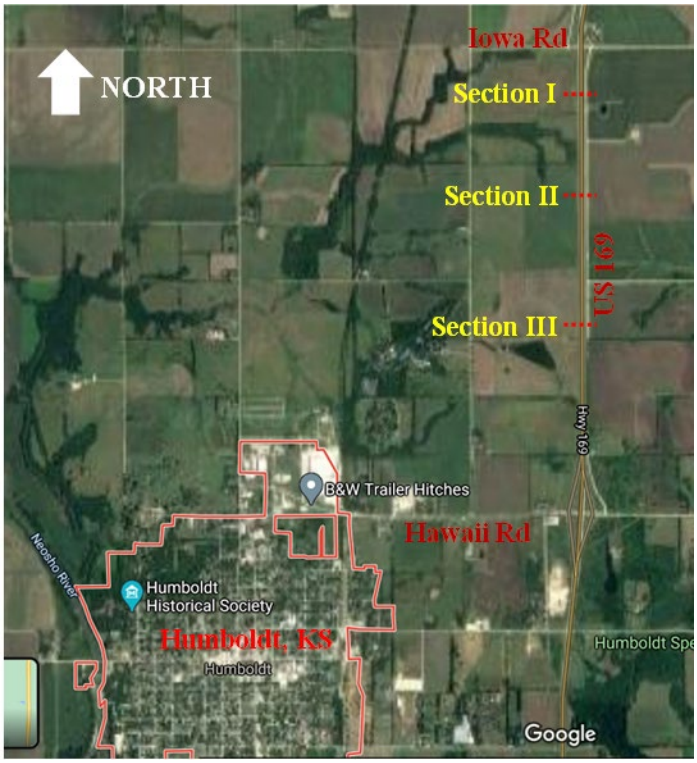

Figure 3.1: Test Sections on the US-169, Allen County, KS

Source: Revised from Google Maps

Both AB-1 and AB-3 aggregates are commonly used by KDOT as base course materials for highway construction. The AB-1 aggregate can be any combinations of crushed stone, crushed or uncrushed gravel, sand, sand-gravel, or limestone gravel while the AB-3 aggregate should have

at least 85% mechanically crushed limestone or dolomite. Table 3.2 provides the specifications of these two aggregates including their gradations and Atterberg limits. Table 3.2 shows that the AB- 3 aggregate typically has more fines (particles passing US No. 200 sieve) and higher Atterberg limits. Table 3.3 provides the properties of the AB-3 aggregate from Wang et al. (2017). The material properties of these materials in this project are presented in Chapter 4.

Table 3.2: Gradation and Atterberg Limits of AB-1 and AB-3

Type	% Retained-square mesh sieves									Plastic index	Liquid limit (max.)
	2"	1.5"	1"	0.75"	0.375"	No.4	No.8	No.40	No. 200		
AB-1	0	0-10		5-40		35-75	54-85	78-95	90-98	0-6	25
AB-3	0	0-5		5-30		35-60	45-70	60-84	80-92	2-8	30

Source: KDOT (2007)

Table 3.3: Properties of the AB-3 Aggregate

Properties	Value
Coefficient of uniformity, C_u	50
Coefficient of curvature, C_c	2.88
Fine content (%)	10
Liquid limit (%)	20
Plasticity index	7
Unified Soil Classification System (USCS)	CL-ML (fine particle), GW-GC (well-graded gravel)
Optimum moisture content (%)	8.3
Maximum dry density, $\gamma_{d\text{-}max}$ (lb/ft^3)	131
Permeability (ft/s)	3.1×10^{-6}

Source: Wang et al. (2017)

The test sections had a jointed concrete pavement, jointed concrete shoulders, and gravel slopes with a rock stone cover. Water infiltration is expected to occur at joints and gravel slopes. Figure 3.2 shows the photo of one of the test sections on the US-169 after opening to traffic for approximately two years. Each direction of the road had one 12-ft (3.6-m) wide traffic lane and one 10-ft (3.0-m) wide shoulder. This highway had five longitudinal joints including one joint between the left lane and the right lane, one joint between the lane and the shoulder in each direction, and another joint between the shoulder and the gravel slope in each direction. In addition, there were transverse joints that crossed the two traffic lanes and the two shoulders, and their spacing of transverse joints was 15.3 ft (4.6 m).

Figure 3.2: Joints of the Pavement Section

3.3 Instrumentation

To investigate the effectiveness of the wicking geotextile to stop capillary rise of water and wick infiltration water from the pavement structure, 42 moisture sensors were installed within these three test sections during pavement construction. Each sensor could record four data points, including volumetric water content (VWC, typically 5% to 50%), electrical conductivity (EC, typically 0 to 8 dS/m), temperature (T, typically -14 to 158 °F), and relative dielectric permittivity (Perm, typically 1 to 81). Volumetric water contents and temperatures are valuable for the analysis of the data for this project; therefore, they will be discussed later.

3.3.1 Test Section I

Figure 3.3 shows the layout of 18 moisture sensors within Section I. The concrete pavement in this section consisted of a subgrade, an 18-in. (0.45-m) thick AB-1 aggregate base, a 4-in. (0.10- m) cement treated base (CTB), and a 9.6-in. (0.24-m) thick Portland Cement Concrete Pavement (PCCP). However, the shoulder consisted of a subgrade, a 26-in. (0.65-m) thick AB-1 aggregate, and a 6-in. (0.15-m) thick PCCP. The transverse slopes for the lane and the shoulder

were 1.6% and 4.2%, respectively to remove water on the pavement lanes and shoulders quickly. The moisture sensors were installed at three levels: (1) Level 1 (bottom level): 6 in. (0.15 m) below the wicking geotextile; (2) Level 2 (middle level): 6 in. (0.15 m) above the wicking geotextile; and (3) Level 3 (top level): 12 in. (0.3 m) above the wicking geotextile. The sensors at Level 1 were installed inside the subgrade soil and the sensors at Level 2 and Level 3 were installed inside the AB-1 aggregate. To evaluate possible water content variations, seven moisture sensors (labeled as A, B, C, D, E, F, and G) were installed at the distances of 0, 6, 12, 17, 22, 25, and 30 ft (0, 1.8, 3.6, 5.1, 6.6, 7.5, and 8.9 m) from the centerline of the road. At Level 2 and Level 3, another two sensors were installed at Distance B (6 ft or 1.8 m away from the centerline of the road) with the offsets 1 and 2 (5 and 10 ft or 1.5 and 3.0 m from the transverse joint, respectively) to investigate the water content variation with the distance from the transverse joint. For easy presentation, each moisture sensor is labeled in a form as Section-Level-Distance-Offset, for example, Sensor I-3-B1 means the sensor corresponding to Level 3 (12 in. or 0.30 m above the wicking geotextile), Distance B (12 ft or 3.6 m away from the centerline) with Offset 1 (5 ft or 1.5 m from the transverse joint) in Section I. Offset was omitted in the label if the sensor had zero offset. Table 3.4 provide the label, the distance, the depth, and the material in which each sensor was installed in Section I.

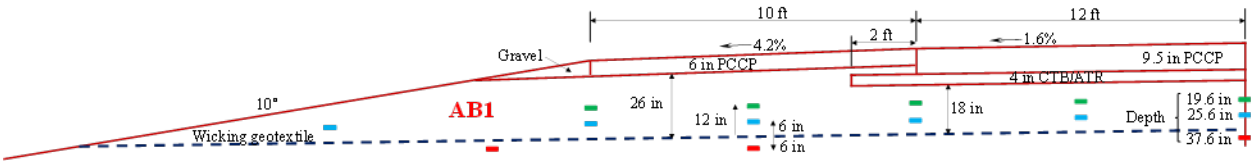

(a) Cross Section

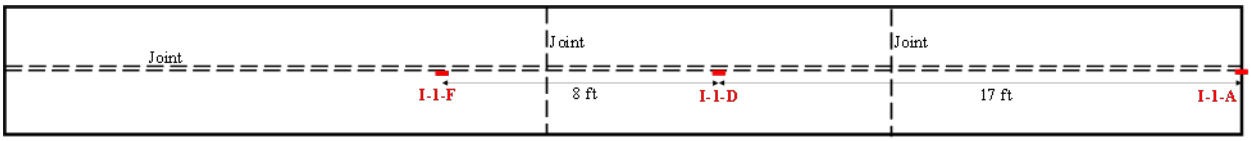

(b) Plan View at Level 1

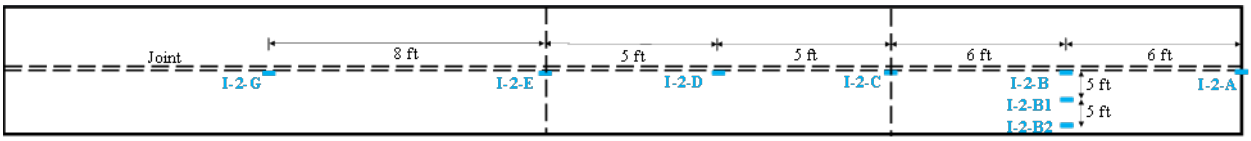

(c) Plan View at Level 2

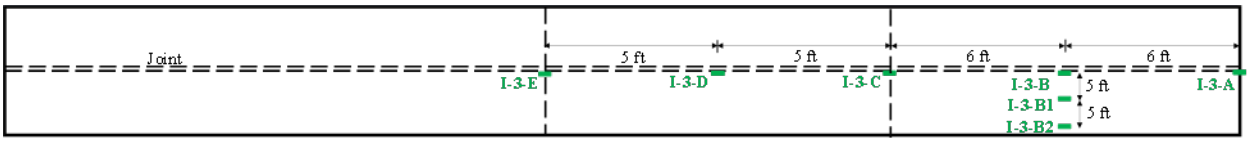

(d) Plan View at Level 3

Figure 3.3: Sensors in Section I

3.3.2 Test Section II

Figure 3.4 shows the layout of four sensors in Section II (control section). In this section, the pavement lane consisted of a subgrade, a 12-in. (0.3-m) thick cement treated subgrade, a 6-in. (0.15-m) thick AB-1 aggregate base, and a 9.6-in. (0.24-m) thick PCCP while the shoulder consisted of a subgrade, a 12-in. (0.3-m) cement treated subgrade, a 13.6-in. (0.34-m) thick AB-1 aggregate base, and a 6-in. (0.15-m) PCCP. Four moisture sensors were installed in the AB-1 aggregate base. In addition to these four sensors shown in Figure 3.4, on November 6th, 2018, two more sensors (Ref. 1 and Ref. 2) were installed at a depth of approximately 2 in. (50 mm) under the soil surface adjacent to the drainage ditch of the road to monitor precipitations in Section II. Unfortunately, one of the sensors broke on October 25th, 2019 (a few months after the installation).

Table 3.5 provides the label, the distance, the depth, and the soil in which each sensor was installed in Section II.

Table 3.4: Sensor Label, Location, and Material in Section I

#	Sensor	Distance, X (ft)	Distance, Y (ft)	z (in.)	Material
1	I-1-A	0.0	0.0	-6	Subgrade
2	I-1-D	17.0	0.0	-6	Subgrade
3	I-1-F	25.0	0.0	-6	Subgrade
4	I-2-A	0.0	0.0	6	AB-1
5	I-2-B	6.0	0.0	6	AB-1
6	I-2-B1	6.0	5.0	6	AB-1
7	I-2-B2	6.0	10.0	6	AB-1
8	I-2-C	12.0	0.0	6	AB-1
9	I-2-D	17.0	0.0	6	AB-1
10	I-2-E	22.0	0.0	6	AB-1
11	I-2-G	30.0	0.0	6	AB-1
12	I-3-A	0.0	0.0	12	AB-1
13	I-3-B	6.0	0.0	12	AB-1
14	I-3-B1	6.0	5.0	12	AB-1
15	I-3-B2	6.0	10.0	12	AB-1
16	I-3-C	12.0	0.0	12	AB-1
17	I-3-D	17.0	0.0	12	AB-1
18	I-3-E	21.7	0.0	12	AB-1

Note: X = the distance from the centerline of the road, Y = the distance from the transverse joint, z = the distance or elevation from the wicking geotextile layer (a positive means the sensor was above the geotextile).

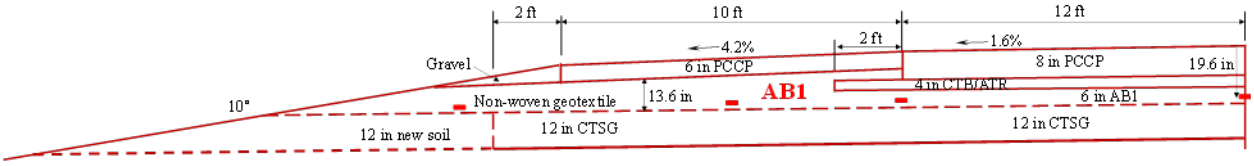

(a) Cross Section

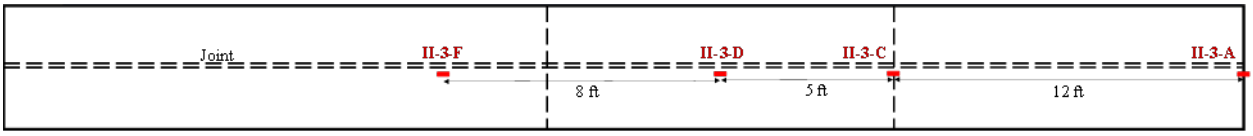

(b) Plan View of Level 3

Figure 3.4: Sensors at Section II

Table 3.5: Sensor Label, Location, and Material in Section II

#	Sensor	Distance, X (ft)	Distance, Y (ft)	z (in.)	Material
1	II-1-A	0.0	0.0	3.0	AB-1
2	II-1-C	12.0	0.0	3.0	AB-1
3	II-1-D	17.0	0.0	3.0	AB-1
4	II-1-F	15.0	0.0	3.0	AB-1
5	Ref-1	To monitor rainfalls			
6	Ref-2				

3.3.3 Test Section III

Section III had the same cross section of materials and layout of sensors as those in Section I except that Section III used the AB-3 aggregate base instead of the AB-1 aggregate base. The sensor labels in Figure 3.3 should be changed from I to III for those in Section III.

3.3.4 Sensor Installation and Datalogger

To install a moisture sensor, a small hole was dug in the soil and then two needles of the sensor were carefully pushed into the soil horizontally to ensure good contact between the sensor and the soil. After the installation of the sensor, the hole was backfilled with the same soil and some compaction was applied. Figure 3.5(a) shows a moisture sensor was installed in the subgrade at the depth of 6 in. (0.15 m) below the designed elevation of the wicking geotextile. After installation of all the sensors in one section, they were connected to a multiplexer (AM 16/32) and the data were automatically collected and stored in a CR1000 or CR1000X datalogger. The datalogger was powered by a 12 V battery, which was charged by a solar panel at daytime. Each section had one data collection system in the box to protect the battery, the multiplexer, and the datalogger from adverse weather conditions (e.g., rainfall) as shown in Figure 3.5.

(a) Installed Sensor

(b) Solar Panel

(c) Datalogger and Battery

(d) Data Collection System in Section I

Figure 3.5: Sensor and Data Collection System

3.4 Construction of Test Sections

After all the sensors in the subgrade were installed, the wicking geotextile was placed, followed by the placement of aggregate, watering, and compaction as shown in Figure 3.6.

(a) Placement of the Wicking Geotextile

(b) Placement of the Aggregate

(c) Adding Water for Easy Compaction

(d) Compaction

Figure 3.6: Construction of the Test Section

Figure 3.7 shows the construction process of the concrete pavement including placement of dowel bars, concrete casting, concrete surface smoothening, and concrete curing.

Table 3.6 lists the dates to complete the pavement construction in these three sections. The Cement Treated Subgrade (CTSG) was completed on July 16th, 2018, for Section II. The base course in Section I was finished on July 23rd, 2018, while the base course in Section II was finished on August 1st and 2nd, 2018. The base course in Section III was finished on July 20th and 23rd, 2018.

The Cement Treated Base (CTB), lane paving, and shoulder paving were finished on August 13th and 14th, August 21st and 22nd, and November 2nd, 2018, respectively, for all three sections.

(a) Placement of Dowel Bars

(b) Concrete Casting

(c) Concrete Surface Smoothing

(d) Concrete Pavement Curing

Figure 3.7: Construction of the Concrete Pavement

Table 3.6: Timeline for Pavement Construction

Construction Process	Section I	Section II	Section III
CTSG	/	July 16th, 2018	/
AB-1 base	July 23rd, 2018	August 1st, 2018, and August 2nd, 2018	/
AB-3 base	/	/	July 20th, 2018, and July 23rd, 2018
CTB	August 13th, 2018, and August 14th, 2018		
Lane paving	August 21st, 2018, and August 22nd, 2018		
Shoulder paving	November 2nd, 2018		

Figure 3.8 shows the road condition on April 1st, 2021.

(a) Road Condition Looking North

(b) Road Condition Looking South

Figure 3.8: Road Condition on April 1st, 2021 (after approximately two years of being open to traffic)

Chapter 4: Laboratory and Field Material Evaluations

4.1 Introduction

This chapter summarizes the results obtained from laboratory and field tests to evaluate the properties of the materials used in this study. The laboratory tests included sieve analysis, Atterberg limit, Proctor compaction tests, and California Bearing Ratio tests to quantify the characteristics of the subgrade and the base material collected from the field. During the pavement construction, field tests were conducted including Nuclear Gauge (NG), Dynamic Cone Penetration (DCP), and Light Weight Deflectometer (LWD) tests.

4.2 Laboratory Tests

Sieve analysis, Atterberg limit, Proctor compaction, and California Bearing Ratio (CBR) tests were conducted for the subgrade soil, AB-1, and AB-3 aggregates in the laboratory at the University of Kansas. Figure 4.1 shows the sieve analysis results for the subgrade and the base materials. The subgrade soil, AB-1, and AB-3 aggregates had 2.8%, 56.5%, and 45.5% of particles retained on the U.S. No. 4 sieve (i.e., gravel), respectively, and 88.6%, 12.5%, and 13.5% of particles passing the U.S. No. 200 sieve (i.e., fines), respectively. Therefore, the AB-1 and AB-3 aggregates had similar fines contents, but the AB-3 aggregate had more small particles than AB-1 as shown in Figure 4.1(b).

Table 4.1 provides the liquid limits (LL), the plastic limits (PL), and the plasticity indices (PI) for the subgrade soil, AB-1, and AB-3 aggregates. The Atterberg limit tests were conducted on the soil particles passing the U.S. No. 40 sieve size. Based on the USCS, the subgrade soil is classified as a high plasticity clay (CH) while the particles of the AB-1 and AB-3 aggregates passing the No. 40 sieve are classified as low-plasticity silt (ML).

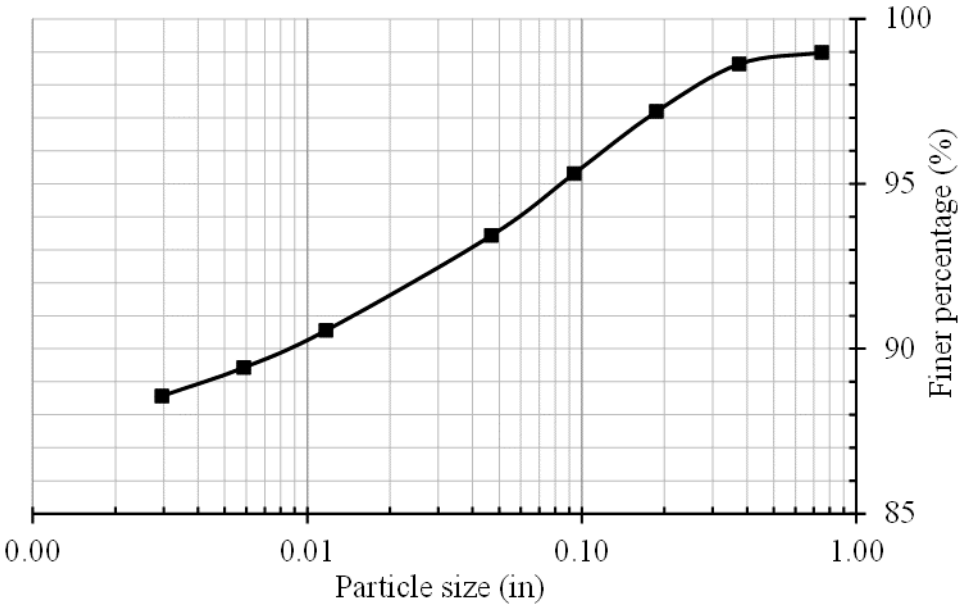

(a) Subgrade Soil

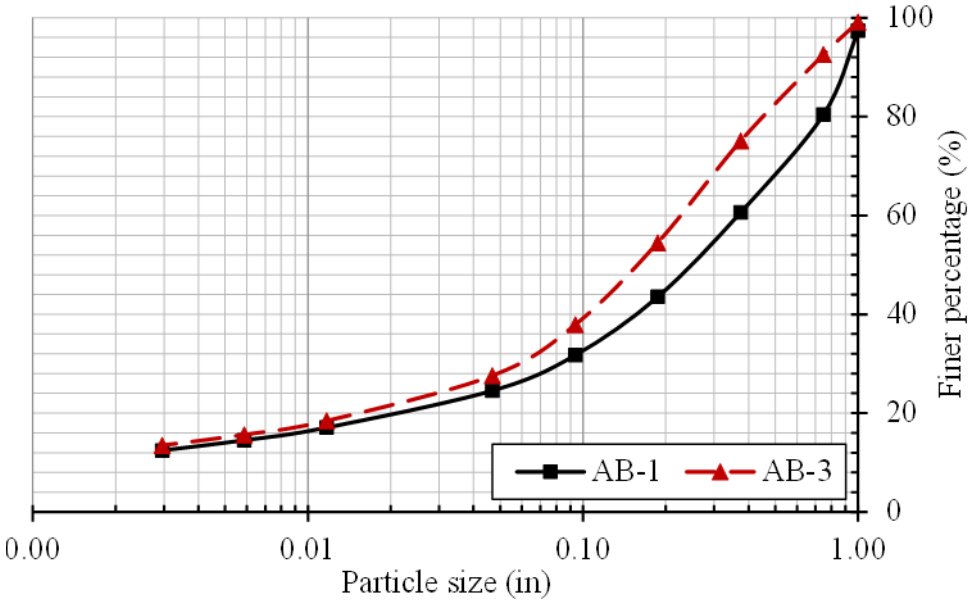

(b) Base Material

Figure 4.1: Sieve Analysis Results

Table 4.1: Results of Atterberg Limit Tests

Material	Liquid limit (%)	Plastic limit (%)	Plasticity index
AB-1	18.6	15.7	2.9
AB-3	19.9	16.8	3.1
Subgrade	61.7	26.5	35.2

Figure 4.2 shows the results of the standard Proctor compaction and CBR tests for the subgrade soil while Figure 4.3 shows the test results for the AB-1 and AB-3 aggregates without the over-sized particles. The CBR values of the subgrade soil decreased with the gravimetric water content while its dry density increased first and then decreased with the gravimetric water content with the optimum water content of 20.2% and the maximum dry density of 105 lb/ft^3 (1677 kg/m^3). The AB-1 and AB-3 aggregates had their optimum water contents of 7.7% and 7.6%, and their corresponding maximum dry densities of 142 lb/ft^3 (2273 kg/m^3) and 140 lb/ft^3 (2247 kg/m^3), respectively after the corrections of over-sized particles. Figure 4.3 also shows that the AB-3 aggregate had a higher maximum density and maximum CBR value than the AB-1 aggregate because the AB-3 aggregate had more small particles that enabled the aggregate to be compacted at a denser condition. At the same time, the CBR value of the AB-3 aggregate was more sensitive to the change of the water content.

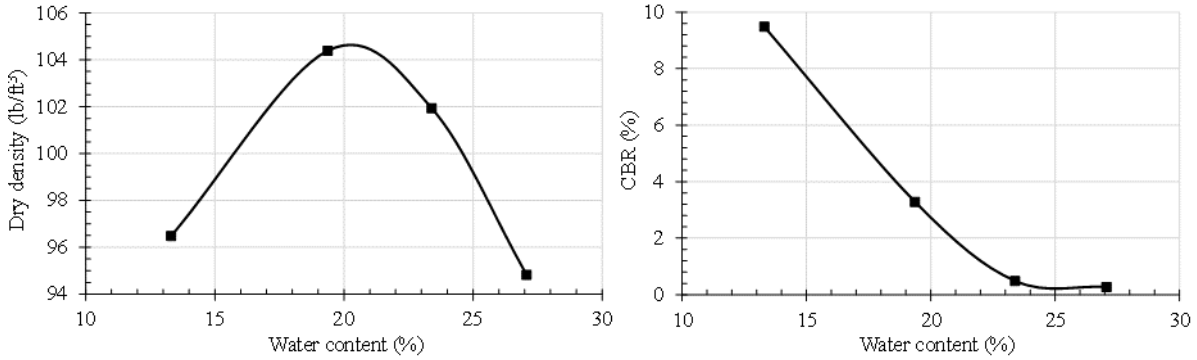

Figure 4.2: Proctor Compaction and CBR Test Results of the Subgrade Soil

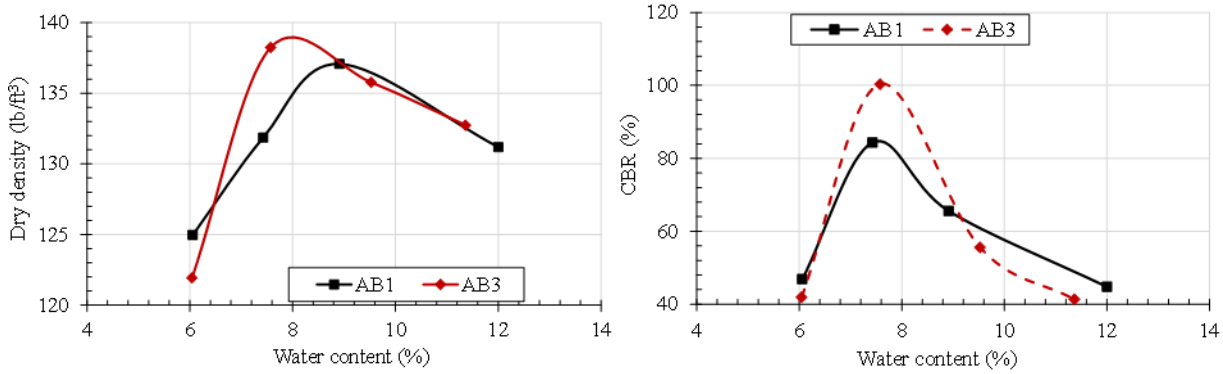

Figure 4.3: Proctor Compaction and CBR Test Results of the Base Materials

Based on the information provided by KDOT, the 12-in. (0.3-m) thick Cement Treated Subgrade (CTSG) was made in place by mixing 4% cement in the first spread and 3% kiln dust in the second spread with the natural subgrade soil within a short time frame. The Cement Treated Base contained 2.7% cement and 2.7% fly ash with a required unconfined, compressive strength for Cement Treated Base (CTB) that was 650 to 1,600 psi (4.5 to 11.0 MPa).

4.3 Field Tests

During the pavement construction, Nuclear Gauge (NG) tests were conducted by the KDOT representative to evaluate the densities and the water contents of the AB-1 and AB-3 aggregates after compaction as part of the quality assurance. The Light Weight Deflectometer (LWD) tests and the Dynamic Cone Penetration (DCP) tests were conducted by the research group to evaluate the properties of the subgrade soil, the AB-1, and AB-3 aggregates. The NG, LWD, and DCP tests were conducted at three locations (i.e., center of the road, middle of the lane, and edge of the road) along the road as shown in Figure 4.4. The center of the road corresponds to the location of the joint between the left lane and the right lane, the middle of the lane corresponds to the centerline of the lane, and the edge of the road corresponds to the edge of the lane away from the centerline of the road.

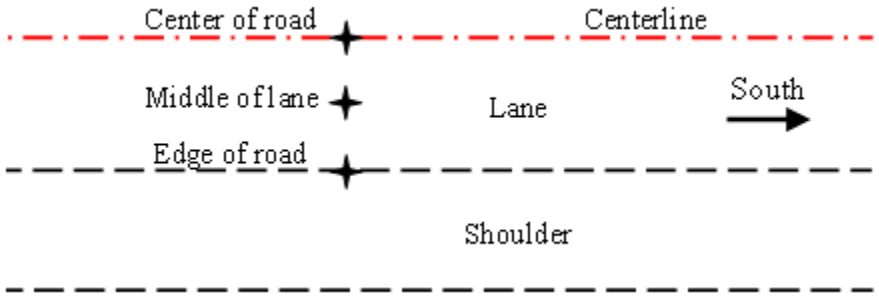

Figure 4.4: Locations of Field Tests in Each Section

4.3.1 Nuclear Gauge Test

The Nuclear Gauge (NG) test uses low-level radiation to measure wet density and water content of a soil so that dry density can be calculated. Table 4.2 shows the results of the NG tests conducted for the AB-1 and AB-3 aggregates. The average water content and dry density of the

AB-1 aggregate were 6.3% and 134 lb/ft^3 (2145 kg/m^3) respectively while the average water content and dry density of AB-3 were 6.2% and 132 lb/ft^3 (2119 kg/m^3), respectively.

The volumetric water content (VWC) is the ratio of the volume of water to the total volume of soil, while the gravimetric water content (w) is the ratio of the mass of water to the mass of the soil. Therefore, Equation 4.1 could be derived to calculate VWC based on *w*. In addition, the saturated VWC could be calculated from the void ratio by Equation 4.2.

$$VWC = \frac{M_w/\rho_w}{M_s(1+e)/\rho_s} = \frac{M_w}{M_s(1+e)} \cdot \frac{\rho_s}{\rho_w} = \frac{wG_s}{(1+e)} = wG_sV_s = \frac{w\rho_d}{\rho_w}$$

Equation 4.1

$$VWC_{sat} = \frac{e}{1+e} = 1 - \rho_d/(G_s\rho_w)$$

Equation 4.2

Where:

ρ_w = density of water,

ρ_d = dry density of soil, and

G_s = specific gravity of soil.

According to the average measured dry density values for the AB-1 aggregate and the AB-3 aggregate and a specific gravity of 2.70, their saturated VMCs are 20.6% for the AB-1 aggregate and 21.5% for the AB-3 aggregate, respectively. These VWCs will be used to evaluate the monitoring data from the field later. Due to the variations of actual density of the aggregates, the measured VMCs of the aggregates at saturated conditions may be higher or lower than these calculated values.

Table 4.2: Results of Nuclear Gauge Tests

Material	Location	Water content, w_c (%)	Dry density (lb/ft^3)	Moist density (lb/ft^3)
AB-1	Center of road	6.0	133	141
	Middle of lane	6.5	137	146
	Edge of road	6.5	132	140
	Average	6.3	134	142
AB-3	Center of road	6.5	137	146
	Middle of lane	6.1	133	141
	Edge of road	5.9	127	135
	Average	6.2	132	141

4.3.2 Lightweight Deflectometer Test

The Lightweight Deflectometer (LWD) is used to measure the surface modulus of a soil layer for ensuring construction quality. The device ZFG 3000 with the drop weight of 22 lb and the load plate of 12 in. in diameter was used for the LWD tests (three drops at each location). Table 4.3 lists the results of the LWD tests. On average, the LWD modulus of the subgrade soil was 4235 psi (29.2 MPa) at the time of testing. The average LWD modulus of the AB-1 aggregate over the subgrade was 4989 psi (34.4 MPa), while the moduli of the AB-3 aggregate after the placement of the second and third lifts were 5120 and 8035 psi (35.3 and 55.4 MPa), respectively. It should be noted that the LWD modulus depends on several factors, such as the mechanical properties and the water content of a soil and the thickness of the base.

Table 4.3: Results of LWD Tests

Material	Lifts of base finished	Location	Elastic modulus, E (psi)	Average settlement, s_{avg} ($\times 10^{-3}$ in.)	Date
AB-1	3	Center of road	4438	29.0	8/1/2018
			4032	31.9	8/1/2018
		Middle of lane	4830	26.6	8/1/2018
			5018	25.6	8/1/2018
		Edge of road	5686	22.6	8/1/2018
			5889	21.8	8/1/2018
AB-3	2	Center of road	4859	26.5	7/20/2018
			8470	15.1	7/20/2018
			6599	18.9	7/20/2018
		Middle of lane	3466	37.1	7/20/2018
			6570	19.6	7/20/2018
			2103	61.3	7/20/2018
			6382	20.1	7/20/2018
		Edge of road	5062	25.4	7/20/2018
			5352	24.0	7/20/2018
			2306	55.8	7/20/2018
	3	Center of road	6164	20.8	7/20/2018
			5773	22.2	7/20/2018
		Middle of lane	11211	11.4	7/20/2018
			6730	19.1	7/20/2018
			7078	18.1	7/20/2018
		Edge of road	8282	15.5	7/20/2018
			6512	19.7	7/20/2018
			12502	10.3	7/20/2018
Subgrade	0	Center of road	4989	25.7	8/1/2018
			4206	30.6	8/1/2018
			3815	33.7	8/1/2018
			4235	30.3	8/1/2018
		Middle of lane	4047	31.7	8/1/2018
			4931	26.0	8/1/2018
			7063	18.2	8/1/2018
			5352	24.0	8/1/2018
		Edge of road	3974	32.4	8/1/2018
			4163	30.9	8/1/2018
			1958	65.6	8/1/2018
			2161	59.3	8/1/2018

4.3.3 Dynamic Cone Penetration Test

Dynamic cone penetration (DCP) test is commonly used to estimate the mechanical properties (strength and stiffness) of a soil. During the pavement construction, a Humboldt dual-mass (DCP Model K100 INT) was used for the DCP tests conducted in this study to evaluate the mechanical properties of the subgrade near Section III, the AB-1 aggregates near Section I and Section II, and the AB-3 aggregate near Section III. Figure 4.6 shows the penetration depth versus

the number of blows for the subgrade soil. Dynamic Penetration Index (DPI in mm/blow) is defined as the penetration depth divided by the number of blows (i.e., the slope of the curve). An increase of DPI or slope indicates a soft response. Figure 4.5 indicates that the mechanical response of the subgrade soil became softer with the depth. This phenomenon can be explained as a result of the increase of the water content with the depth. After the pavement construction, the subgrade soil was covered by the aggregate base and the concrete pavement. However, water infiltration through the joints and water rise from the high water table might increase the water content of the subgrade soil. For an evaluation purpose, the DPI for the subgrade soil at the depth of 2 in. (50 mm) was chosen to represent the mechanical properties of the subgrade soil. Figure 4.6(a) shows the results of the DCP tests conducted after compaction of all the three lifts of the AB-1 aggregate base (in total, 18 in., or 0.45 m thick) in Section I, while Figure 4.6(b) shows the DCP test results for the AB-1 aggregate base (6 in. or 0.15 m thick) in Section II. Figure 4.6(a) shows that the aggregate base near the surface (within the depth from 0 to 10 in. or 0 to 0.25 m) was softer than that at the greater depth. It is well known that the strength and modulus of a granular material increase with the confining stress or depth. Water loss due to evaporation during the placement and compaction of each lift may contribute to this response as well. Figure 4.7 shows the DCP test results after the placement of the first lift of the AB-3 aggregate base material in Section III.

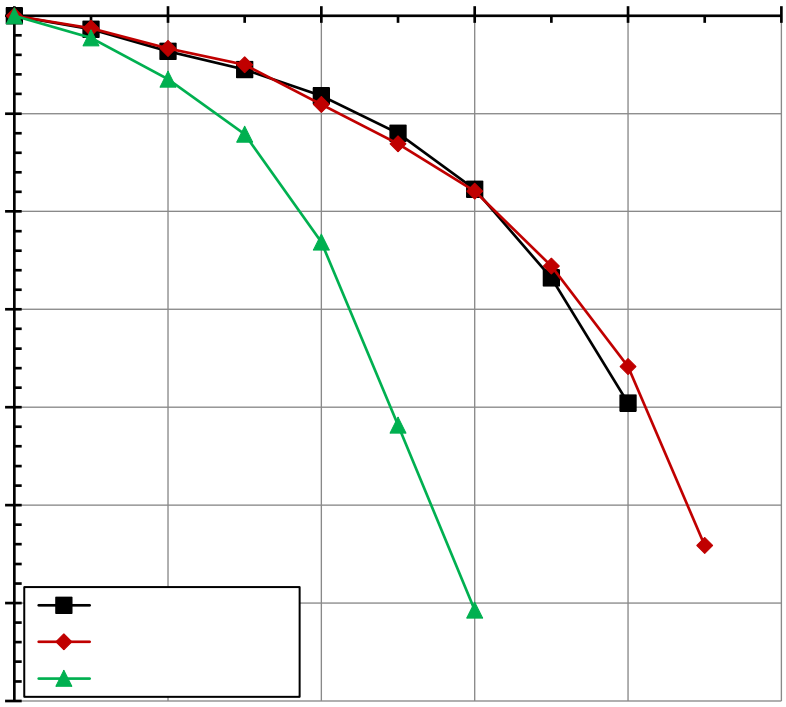

Figure 4.5: DCP Test Results for the Subgrade Soil in Section III

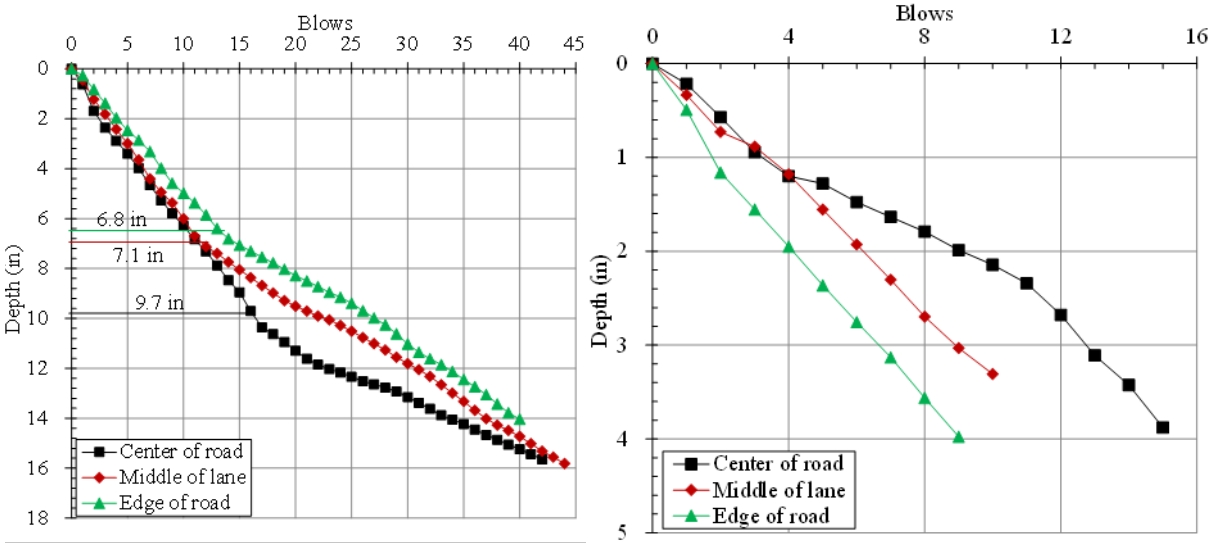

a. After Three Lifts in Section I

b. After One Lift in Section II

Figure 4.6: DCP Test Results for the AB-1 Aggregate Bases in Section I and Section II

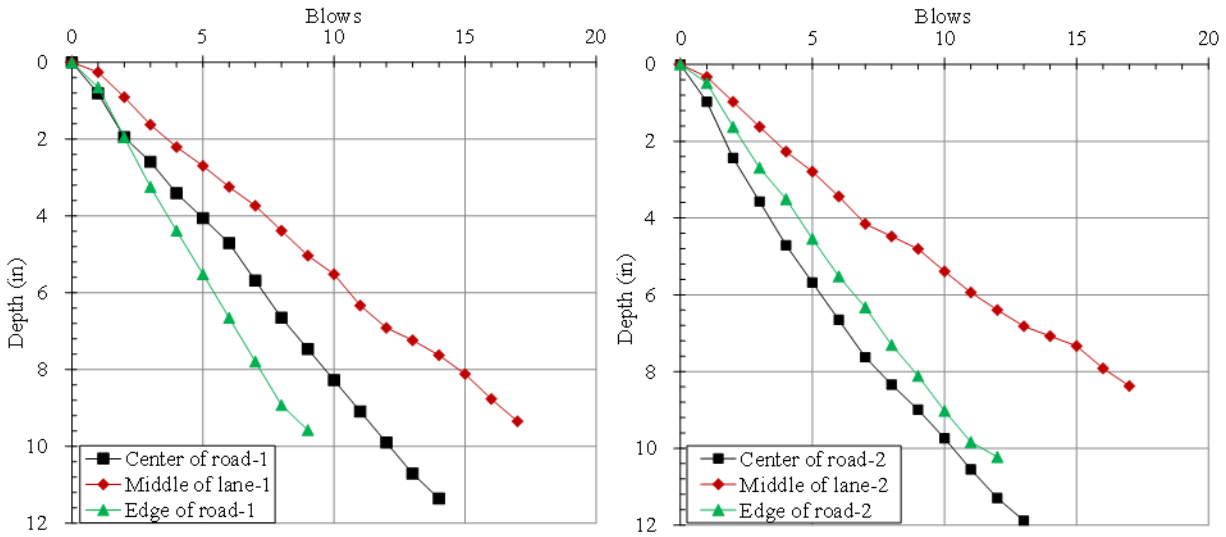

Figure 4.7: DCP Test Results for the AB-3 Aggregate Base in Section III

Table 4.4 summarizes the DCP penetration indices calculated from the DCP test data as presented above. Based on the correlations developed by Webster, Grau, and Williams (1992) and Webster, Brown, and Porter (1994), California Bearing Ratio (CBR) could be estimated using DPI with Equation 4.3 and Equation 4.4. When CBR is less than 10%, Equation 4.3 should be used; otherwise, Equation 4.4 is preferred:

$$\mathrm{CBR}(\%) = \frac{292}{\mathrm{DPI}^{1.12}}$$

Equation 4.3

$$\mathrm{CBR}(\%) = \frac{1}{(0.017019\mathrm{DPI})^2}$$

Equation 4.4

In addition, the elastic modulus of a soil (E) could be estimated using DPI with Equation 4.5 (Powell, Potter, Mayhew, & Nunn, 1984):

$$\mathrm{E(MPa)} = 17.6\mathrm{CBR}^{0.64}$$

Equation 4.5

Table 4.5 and Table 4.6 list the calculated CBR and elastic modulus values, respectively, using Equation 4.3 through Equation 4.5. On average, the CBRs for the subgrade soil, the AB-1 aggregate, the AB-3 aggregate were 3.2%, 55.1%, and 29.1%, respectively, while the elastic moduli for the subgrade, the AB-1 aggregate, and the AB-3 aggregate were 5323, 31328, and 21234 psi (36.7, 216.0, and 146.4 MPa), respectively.

Table 4.4: DPI from the DCP Tests

Section	Location	AB-1		AB-3		Subgrade
		0-6 in.	10-16 in.	0-6 in. (1)	0-6 in. (2)	
I	Center of road	12.7	5.1	/	/	/
	Middle of lane	15.4	6.8	/	/	/
	Edge of road	15.1	7.1	/	/	/
II	Center of road	6.1	/	/	/	/
	Middle of lane	8.6	/	/	/	/
	Edge of road	10.9	/	/	/	/
III	Center of road	/	/	12.5	14.0	46.6
	Middle of lane	/	/	8.6	7.7	50.8
	Edge of road	/	/	17.2	13.8	83.6

Table 4.5: California Bearing Ratio (%) of the Subgrade Soil and the Aggregate Bases

Section	Location	AB-1		AB-3		Subgrade
		0-6 in.	10-16 in.	0-6 in. (1)	0-6 in. (2)	
I	Center of road	21.4	132.7	/	/	/
	Middle of lane	14.6	74.7	/	/	/
	Edge of road	15.1	68.5	/	/	/
II	Center of road	92.8	/	/	/	/
	Middle of lane	46.7	/	/	/	/
	Edge of road	29.1	/	/	/	/
III	Center of road	/	/	22.1	17.6	4.0
	Middle of lane	/	/	46.7	58.2	3.6
	Edge of road	/	/	11.7	18.1	2.1

Table 4.6: Elastic Modulus (psi) of the Subgrade Soil and the Base Material

Section	Location	AB-1		AB-3		Subgrade
		0-6 in.	10-16 in.	0-6 in. (1)	0-6 in. (2)	
I	Center of road	18136	58305	/	/	18136
	Middle of lane	14170	40345	/	/	14170
	Edge of road	14531	38176	/	/	14531
II	Center of road	46364	/	/	/	46364
	Middle of lane	29870	/	/	/	29870
	Edge of road	22054	/	/	/	22054
III	Center of road	/	/	17095	6151	/
	Middle of lane	/	/	31748	5782	/
	Edge of road	/	/	14053	4046	/

Chapter 5: Monitoring Data and Analysis

5.1 Introduction

This chapter provides and analyzes the monitoring data of the Volumetric Water Contents (VWC) from the moisture sensors in three test sections. Since weather condition, such as precipitation, temperature, and relative humidity, is a vital factor affecting groundwater table, water contents in pavements, evaporation, and wicking ability of the wicking geotextile, the weather condition in Humboldt, Kansas is introduced first. The temperature variations in the pavements and the VWC variations to examine the short-term and long-term performance of the wicking geotextile are analyzed and discussed later in this chapter.

5.2 Weather Condition

Precipitation (either rainfall or snowfall) changes water contents of soils in pavement structures. In this report, precipitation is mostly referred to as rainfall unless noted for snowfall. First, water from rainfalls infiltrating through joints, existing cracks, and side slopes increases water contents of soils in the pavement structure. Second, precipitations raise the groundwater table, which may submerge part of the pavement structure. Third, water may migrate into the pavement structure by capillary action from a high-water table, drainage ditches, and shoulders. Temperature, wind speed, and relative humidity affect evaporation of water and performances of the wicking geotextile (Guo et al., 2017). Consequently, the weather condition, such as precipitation, temperature, relative humidity, and wind speed, is vital to the analysis of water content changes of the soils in the pavement structure.

Figure 5.1 shows the daily air temperature, precipitation, relative humidity, and wind speed from July 15th, 2018, to March 31st, 2021, in Humboldt, KS, which corresponded to the period of field monitoring for this project. Different from random variations of precipitation, relative humidity, and wind speed during this period, the air temperature increased from February to August and then decreased from August to next February. The highest and lowest daily temperatures were 87.3 °F (30.7 °C) on July 20th, 2019, and -3.6 °F (-19.8 °C) on February 15th, 2021. While the highest precipitation and wind speed were 3.56 in. (90.4 mm) on May 20th, 2019, and 39.2 mph (62.7 km/h) on May 6th, 2019, respectively. The lowest relative humidity was 32.4%

on October 15th, 2020. Table 5.1 lists the weather conditions for the days with a precipitation heavier than 1.0 in. (25.4 mm). The month of May 2019 had the most days (May 7th, 20th, 21st, and 24th) with the precipitation heavier than 1 in. (25.4 mm).

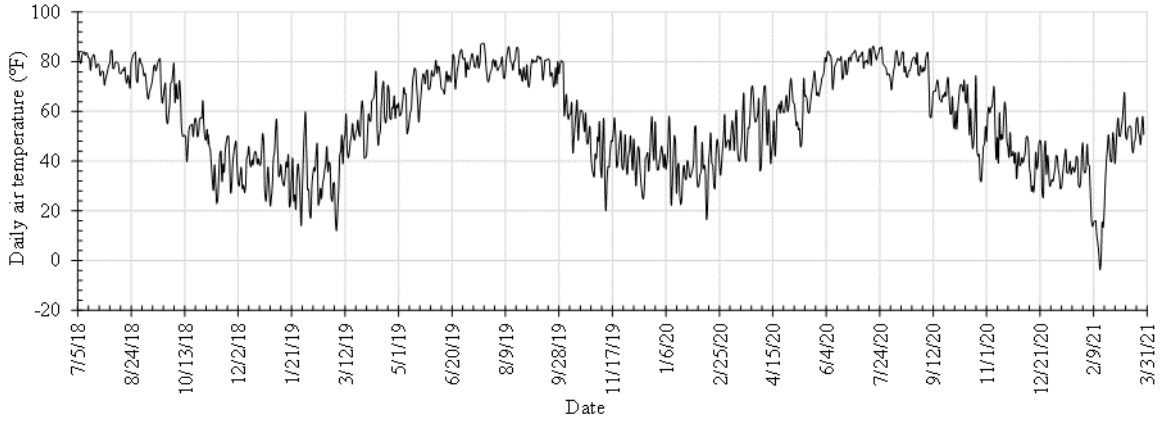

(a) Daily Air Temperature

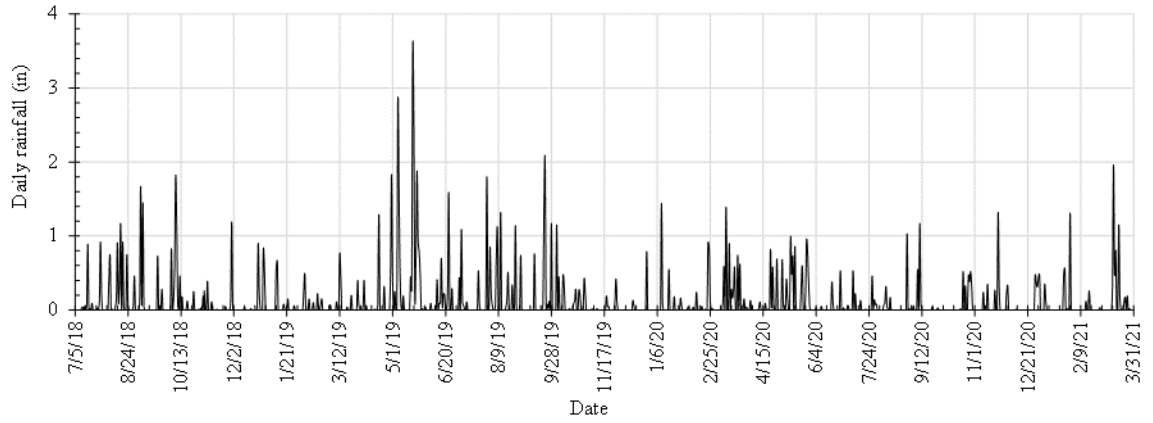

(b) Daily Precipitation

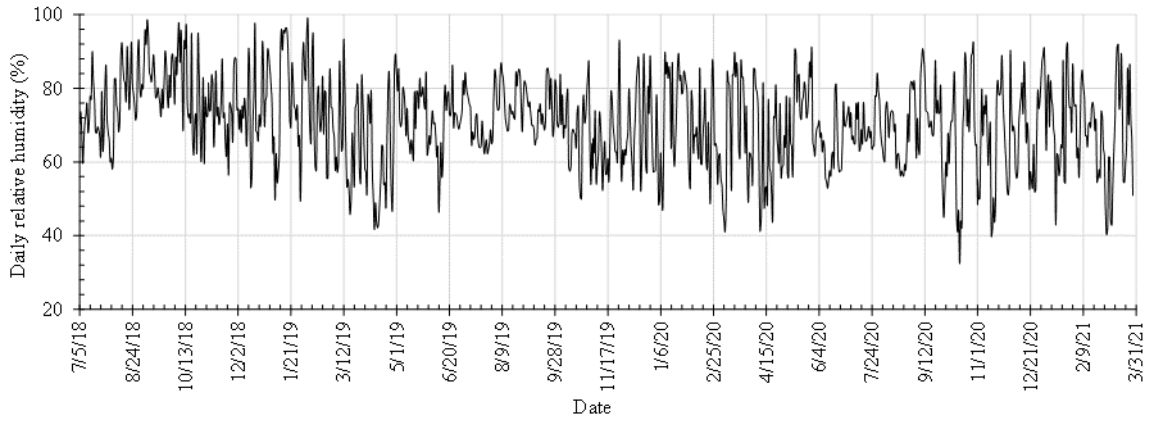

(c) Daily Relative Humidity

Figure 5.1: Weather Condition in Humboldt, KS from July 2017 to March 2021

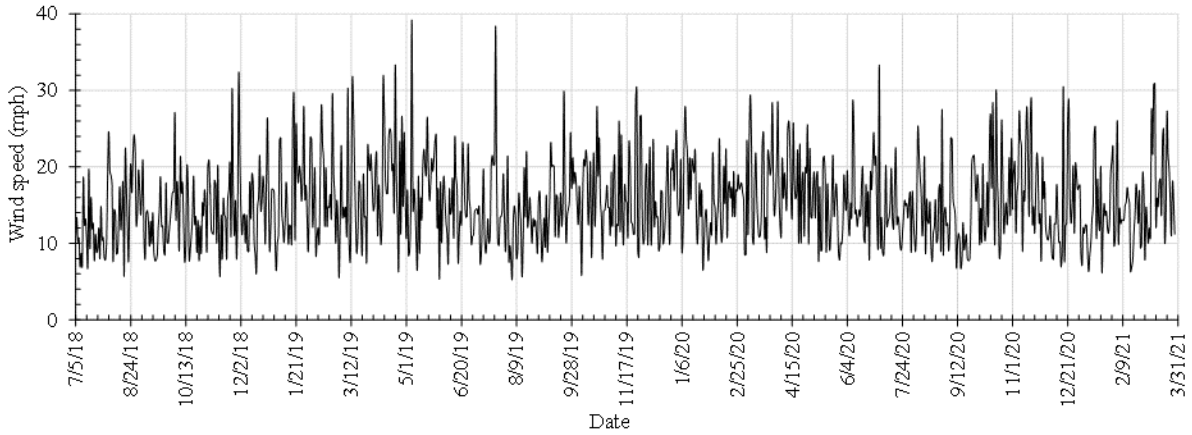

(d) Daily Wind Speed

Figure 5.1: Weather Condition in Humboldt, KS from July 2017 to March 2021 (Continued)

Source: https://www.visualcrossing.com (n.d.)

Table 5.1: Weather Condition for the Days with Daily Precipitation Heavier than 1 inch

No.	Date	Air temperature (°F)	Precipitation (in.)	Relative humidity (%)	Wind speed (mph)
1	8/17/2018	76.4	1.17	81.4	17.8
2	9/5/2018	74.3	1.67	95.9	11
3	9/7/2018	72	1.45	98.6	13.9
4	10/8/2018	72.5	1.81	87.0	21.2
5	10/9/2018	67.6	1.16	95.8	16.6
6	11/30/2018	47.9	1.19	87.9	32.3
7	4/18/2019	57.9	1.29	64.2	19.5
8	4/30/2019	61.5	1.83	89.3	16.2
9	5/6/2019	69.6	2.84	71.4	39.2
10	5/7/2019	67.1	1.56	80.1	14.4
11	5/20/2019	55.7	3.56	79.3	26.5
12	5/21/2019	61.7	2.48	78.7	19.9
13	5/24/2019	75.1	1.88	77.8	21.1
14	6/23/2019	69.3	1.59	86.2	15.8
15	7/5/2019	77	1.09	84.3	13.8
16	7/29/2019	80.9	1.8	68.7	13.2
17	8/8/2019	73.1	1.1	87.0	13.4
18	8/11/2019	84.1	1.32	77.9	16.4
19	8/25/2019	72.1	1.14	85.2	12.2
20	9/21/2019	75.7	1.36	85.5	29.9
21	9/22/2019	75	2.04	83.7	17.6
22	9/28/2019	75.1	1.17	82.1	17.2
23	10/3/2019	58.6	1.15	83.8	14.8
24	1/10/2020	49.7	1.44	89.3	23.5
25	3/11/2020	55.6	1.39	80.8	9.9
26	8/29/2020	74.9	1.03	79.4	27.5
27	9/10/2020	57.5	1.17	90.7	13.6
28	11/23/2020	51.6	1.32	80.5	21.8
29	1/30/2021	47.2	1.31	86.5	20.9
30	3/12/2021	48.7	1.96	84.6	15.9
31	3/17/2021	45.8	1.15	89.5	23.7

5.3 Temperature Variations in Pavement

Temperatures in pavement structures depend on heat conductivity of pavement layers. The moisture sensors at Level 3 (top level) in Section I and Section III were 19.3 in. (0.49 m) deep from the pavement surface while the sensors at Level 3 in Section II (the control section) was 16.5 in. (0.42 m) deep from the pavement surface; therefore, they were at approximately the same depth from the pavement surface and their readings can be compared. Figure 5.2 shows the changes of the temperature readings of the sensors under the centerline of the road (Sensor I-3-A, Sensor II-3-A, and Sensor III-3-A) with the air temperatures from July 1st, 2018, to March 27th, 2021. The temperature in the pavement changed with the air temperature seasonally, and the temperature in the pavement was higher than the air temperature in summer. Conduction, radiation, convection, and vapor diffusion affect heat transfer in pavement structures (Dawson, 2009). The temperatures of these three sensors fluctuated less significantly after September 2018, due to the completion of the lane pavement. A concrete pavement can impede heat transfer through radiation from sunlight and convection between air in the atmosphere and air in a base course. As a result, the temperature readings of the sensors in the pavement became less sensitive to the air temperatures. The temperature of the pavement surface became much higher than the air temperature due to radiation from sunlight at daytime, and the higher temperature of the concrete pavement than the temperature in the aggregate base transferred heat downward, increasing the temperature in the aggregate base so that it was higher than the air temperature. Since thermal capacities for concrete, soil, and water are much higher than the thermal capacity of air (Dawson, 2009), dispersal of heat in the atmosphere was much quicker than that in the aggregate base covered by the concrete pavement. This resulted in higher temperature in the aggregate base than that of air at night. The months of July 2019 and February 2021 were chosen to study the temperature variations in the pavement structure under the hot and cold air temperature conditions, respectively.

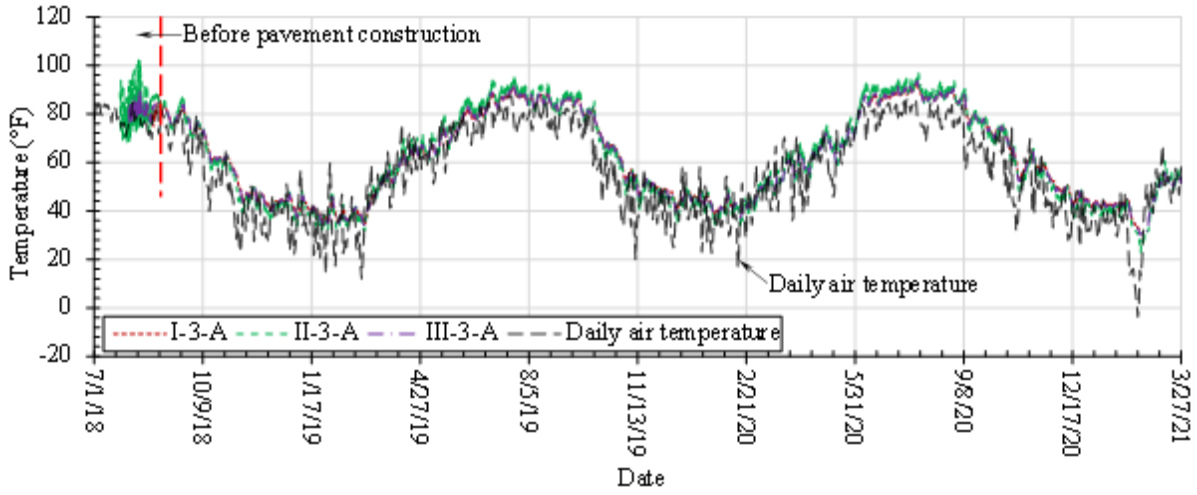

Figure 5.2: Variations of Air and Pavement Temperatures from July 2018 to March 2021

5.3.1 Hot Air Temperature Condition

Figure 5.3 shows the air and soil surface temperatures in July 2019. The soil surface temperature was obtained as the temperature from one surviving reference sensor installed under the soil surface in Section II. The highest and lowest temperatures under the soil surface were higher than those of air, respectively. The higher temperature under the soil surface might be caused by radiation from sunlight and higher thermal capacity of the soil than that of air. In addition, the soil surface temperature lagged three hours behind the air temperature. The air temperature increased from 7 a.m. to 3 p.m. and then decreased until 7 a.m. in the next morning, while the soil surface temperature increased from 10 a.m. to 6 p.m., and then decreased until 10 a.m. in the next morning. Since the thermal capacity of soil was much higher than that of air in the atmosphere, it took longer time to accumulate enough heat to increase the temperature of the soil than that of air. In other words, the soil reacted more slowly to sunrise and sunset than air.

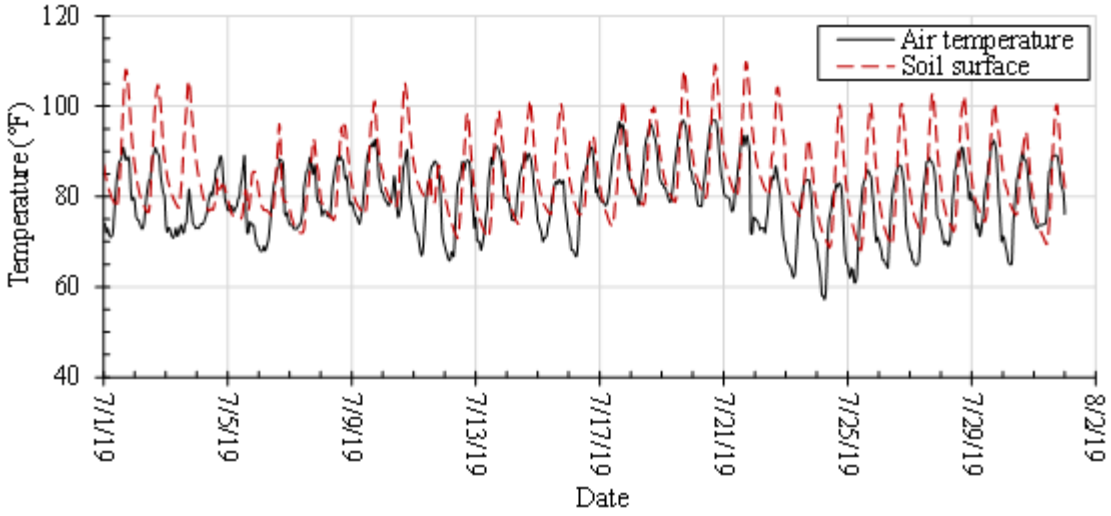

Figure 5.3: Air and Soil Surface Temperatures in July 2019

Figure 5.4 shows the temperatures measured by the sensors at Level 3 in Section I, Section II, and Section III. Since the aggregate base was covered by the concrete pavement, the temperature readings of the sensors in the aggregate base were less affected by the air temperature and radiation as compared with the temperature readings from the sensor installed under the soil surface and the sensor not covered by the concrete pavement (II-1-F). In addition, another lag effect between the temperature under the soil surface and the temperatures in the aggregate base existed, and the temperature lag effect for Sensor II-1-F was less significant than other sensors. The reason was that Senor II-1-F, not covered by the concrete pavement, could interact with the air temperature much more easily than other sensors covered by the concrete pavement. Since the concrete pavement could absorb radiation much more easily than the soil, heat transferred from the concrete pavement to the aggregate base, resulting in higher temperature readings of the sensors under the pavement than the temperature readings of the sensor under the soil surface.

The temperature readings of the sensors in Section II varied more significantly than those in other two sections, and the temperature readings of the sensors located at the distances of A, C, and D in Section II were higher than those at the same distances in Section I and Section III. This difference may be because the depth of the sensors in Section II (16.5 in. or 0.42 m from the pavement surface) was smaller than the depth of the sensors in the other two sections (19.3 in. or 0.49 m from the pavement surface). In addition, the temperature readings of the sensors under the

centerline of the road (Distance A) were higher than those of the sensors under the joint between the lane and the shoulder (Distance C) and the sensors under the centerline of the shoulder (Distance D). Due to radiation and air temperature, the temperature of the concrete pavement increased, and then the heat was transferred to the aggregate base. The temperatures corresponding to the sensors at Distance A could become higher because of its higher elevation than the sensors at Distance C and Distance D. Another reason is that the sensors at Distance A (farther away from the drainage ditch laterally than the sensors at Distance C and Distance D) were not cooled by air or wind as those at Distance C and Distance D.

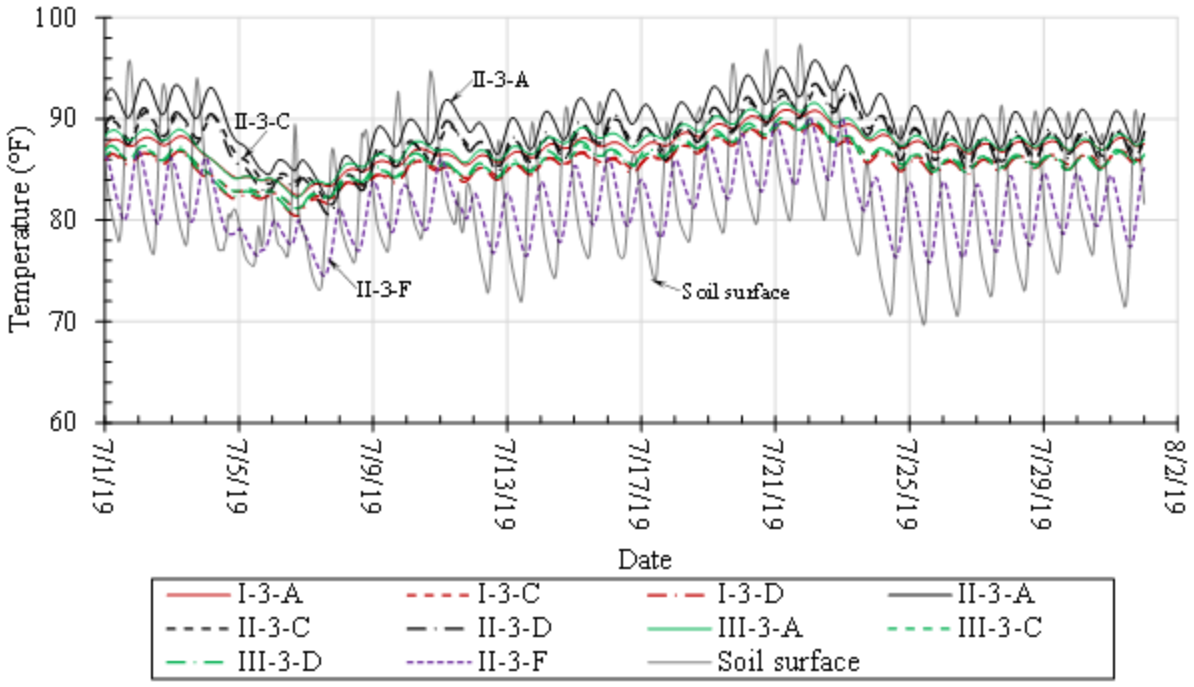

Figure 5.4: Temperature Readings from the Sensors in July 2019

Figure 5.4 shows that the three sections had the similar temperature variation patterns in July 2019; therefore, Section III was chosen as an illustration to analyze the temperature changes with the depth from the pavement surface and the distance from the transverse joint. Figure 5.5 shows that the temperature decreased with the depth and the hourly temperature variations became less significant as the depth increased. With an increase of the depth of the sensors from the pavement surface, less heat from the pavement was transferred to the aggregate base at daytime

and less heat from the aggregate base was transferred to the concrete pavement at night as well; therefore, the temperatures and the hourly temperature variations in the aggregate bases decreased as the depth from the pavement surface increased. Furthermore, the temperature in the subgrade soil did not change hourly with the air temperature. The hourly temperature changes at the concrete pavement surface could not affect the temperature in the subgrade soil because the sensor was 31.1 in. (0.79 m) away from the pavement surface. In addition, the aggregate base with relatively large porosity performed as an insulation layer for the subgrade soil. However, all the temperature readings of the sensors in the pavement generally changed daily with the air temperature. Figure 5.6 shows that the transverse joint had negligible effects on the temperature changes in the pavement structure.

Figure 5.7 shows the temperature distributions in the pavement structure in Section I and Section III at 12:00 p.m. on July 20th, 2019. The temperature distributions indicated that the two sections had similar temperature distribution patterns. The temperature decreased with an increase of the depth from the pavement surface and the distance from the centerline of the pavement. In addition, the temperatures in Section III were slightly higher than the temperatures in Section I. This difference might result from different fine contents and water contents in the aggregate bases in these two sections.

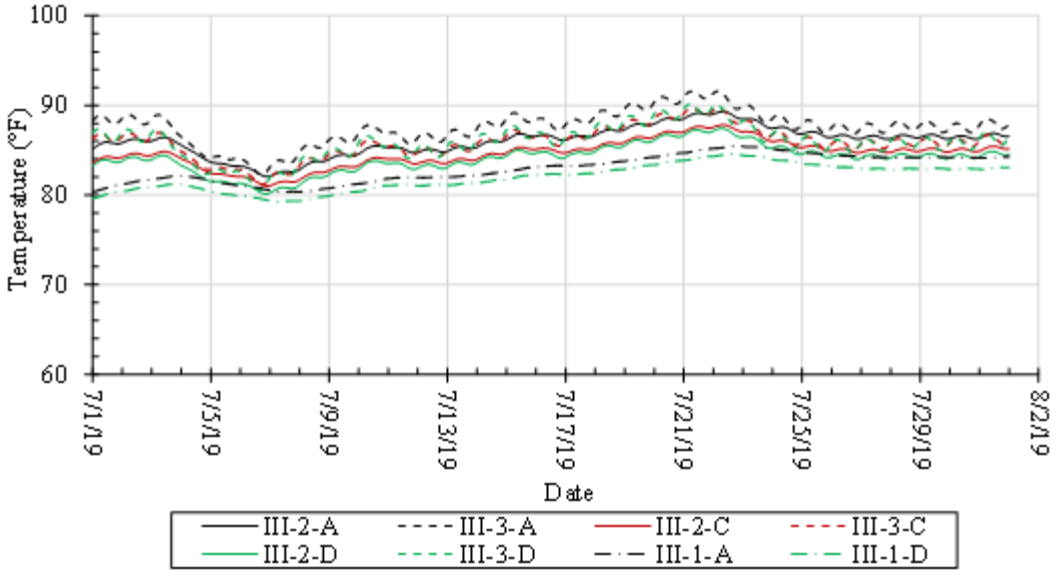

Figure 5.5: Change of Temperature Readings at Different Distances in Section III

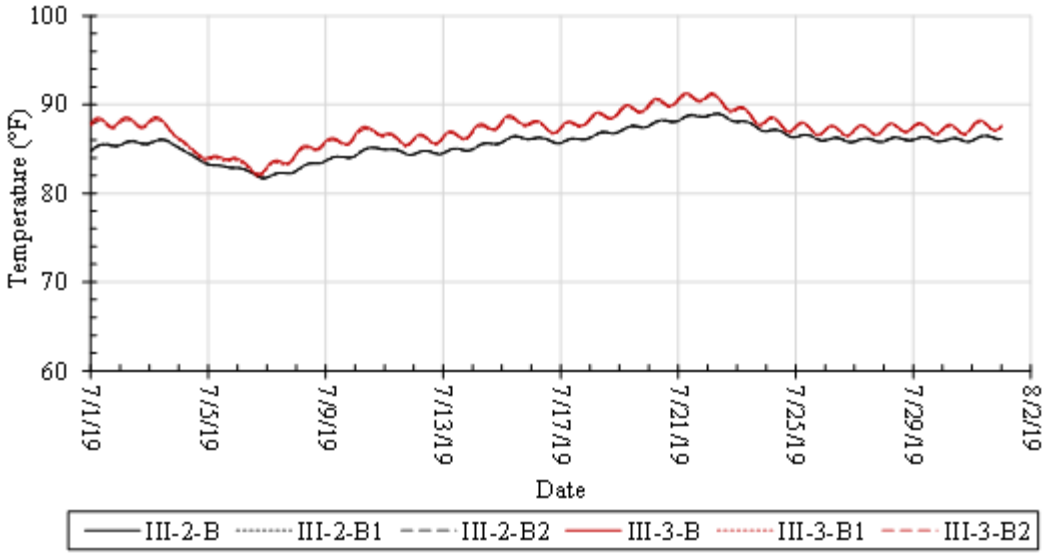

Figure 5.6: Change of Temperature Readings at Different Distances from Transverse Joint in Section III

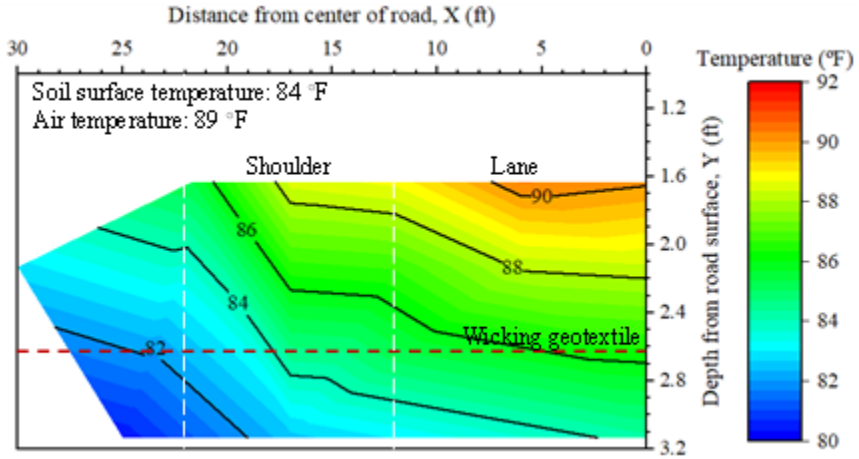

(a) Section I

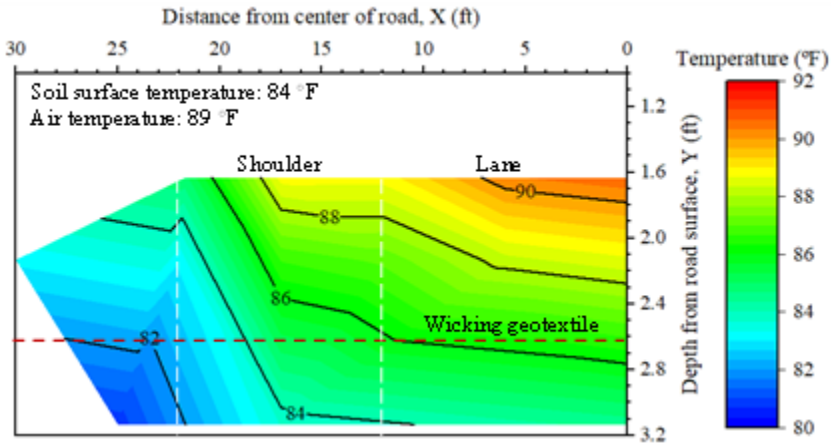

(b) Section III

Figure 5.7: Temperature Distributions in the Pavement Sections at 12 p.m. on July 20th, 2019

5.3.2 Cold Air Temperature Condition

Figure 5.8 shows the temperatures in air and under the soil surface during February 2021. The air temperature ranged between -14 °F to 22 °F (-26 ºC to -6 ºC) from February 13th, 2021, to February 17th, 2021, while the lowest soil surface temperature was approximately 24.8 °F (-4 ºC). When the temperature of the soil surface dropped below 32 °F (0 ºC), some water in the soil was frozen. According to Dawson (2009), the thermal conductivity of ice is four times higher than the conductivity of water. Theoretically speaking, the temperature under the soil surface should be much lower than 24.8 °F (-4 ºC). The weather condition in Humboldt, Kansas showed that the soil was covered by snow from February 7th to 23rd; therefore, the insulation of snow might be the reason why the temperature in the soil was just approximately 24.8 °F (-4 ºC). Even though the air temperature increased to above 32 °F (0 ºC) after February 21st, 2021, the soil surface temperature increased to above 32 °F (0 ºC) after February 24th, 2021. The snow melted on the top of the soil surface at the air temperature above 32 °F (0 ºC) and lost its insulation effect until all snow melted. After all snow melted, the soil interacted with air in the atmosphere again; therefore, the temperature under the soil surface fluctuated with the air temperature after February 24th, 2021.

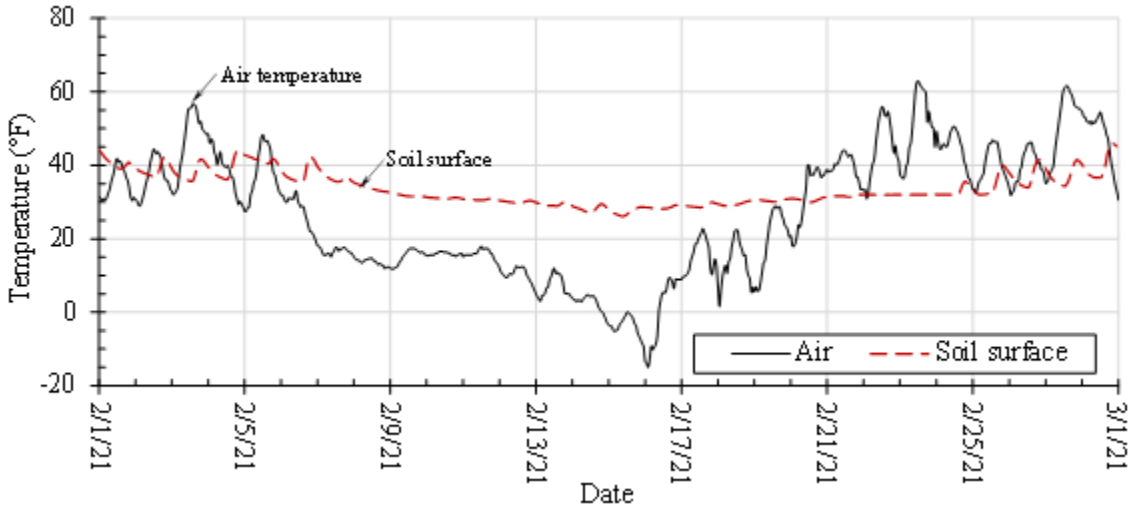

Figure 5.8: Air Temperature and Temperature under the Soil Surface in February 2021

Figure 5.9 shows the temperature variations in the pavement structure during February 2021. In Section I, the datalogger did not record any readings from all the sensors on February 16th,

2021. The exact reason is unknown, but it might be caused by the low air temperature on that day. The sensors at Distance A, Distance C, and Distance D in Section II had lower temperatures than the sensors at the same locations in Section III from February 16th to 22nd. Overall, the daily temperature variations of the sensors in Section II were more significant than the sensors in Section I and Section III. Since the depth of the sensors in Section II was smaller than those of the sensors at Level 3 in Section I and Section III, the temperature changes of the concrete pavement surface with the air temperature had more effects on the readings of the sensors at Level 3 in Section II than those at Level 3 in Section I and Section III. Dawson (2009) pointed out that thermal conductivity of a soil increases with its water content. Due to the wicking ability of the wicking geotextile, Section I and Section III had lower water contents at this level as discussed later. As a result, the conductivity of the aggregate bases in these sections was lower so that higher temperatures and less significant temperature variations happened. When the temperature dropped below 32 °F (0 °C), the thermal conductivity of the soil increased due to water freezing. In addition, ice lenses might develop in the aggregate base that attracted more water and increased the water content. As a result, the thermal conductivity increased as the water content increased. The above may explain why the temperature in Section II varied more significantly than those in the other two sections from February 16th to 23rd. The temperature readings from Sensor II-3-F in Section II had the similar temperature change pattern as those under the soil surface because the aggregate base around the sensor without a concrete pavement could interact with the air temperature similarly as the soil surface. The temperatures from the other three sensors in Section II dropped with time gradually and then dropped dramatically at 6 a.m. on February 16th, 2021. The reason for this phenomenon might be that the water in the pavement was frozen and the thermal conductivity of the aggregate base increased dramatically consequently.

Figure 5.10 shows the temperature changes at different depths in Section III. The temperature in the aggregate base increased as the depth from the pavement surface increased under the cold weather condition because the cooling effect of the air temperature decreased with the depth. The temperature readings of the sensors decreased from February 7th, 2021, and then increased abruptly from February 24th, 2021, which coincided with the existence of snow during the same period. This phenomenon indicates that snow could work as an insulation to minimize

the effect of cold temperature on the aggregate base in the pavement. In addition, the abrupt temperature increases occurred sequentially from Distance A to Distance D due to the elevation differences. Figure 5.11 shows that the existence of the transverse joint had a negligible effect on the temperature change in the pavement under the cold weather condition.

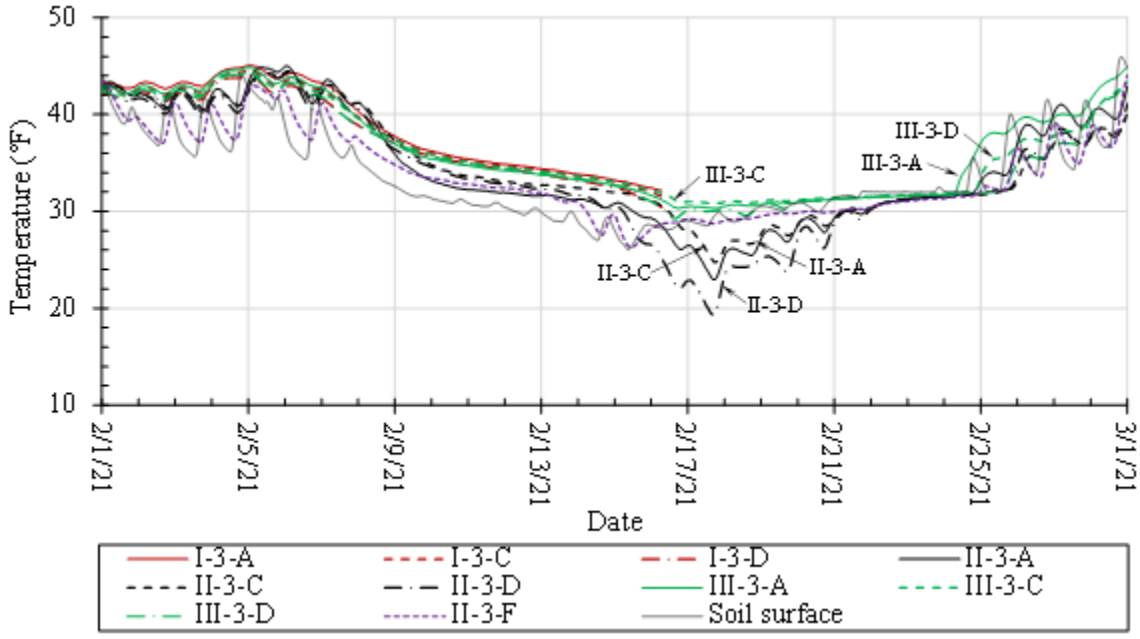

Figure 5.9: Temperature Readings of the Sensors in the Three Sections

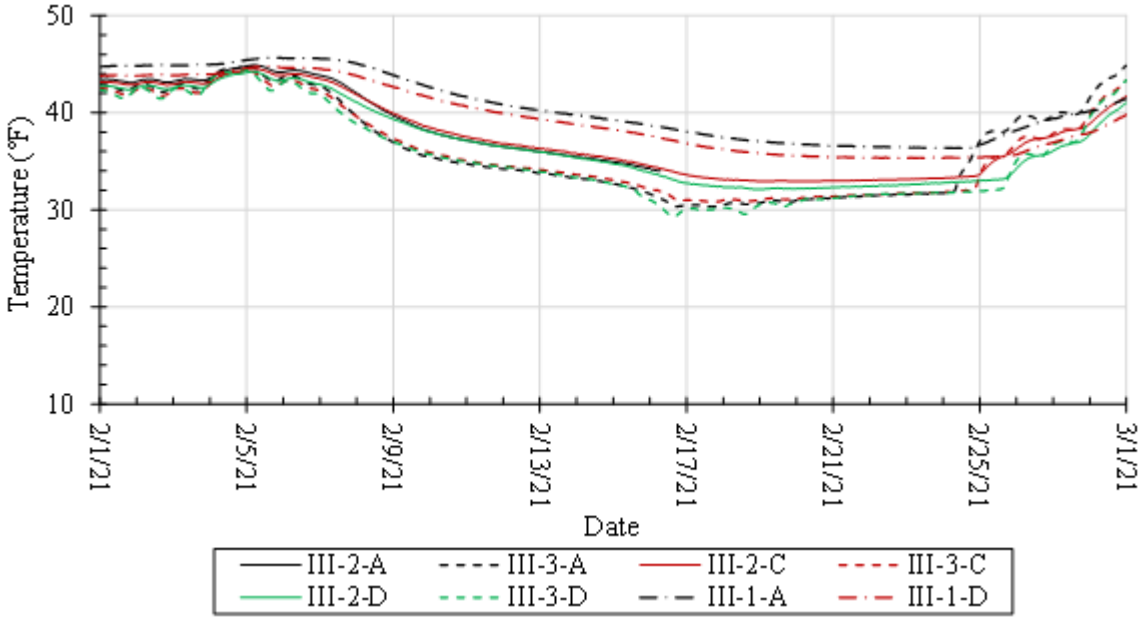

Figure 5.10: Temperature Variations with Depths in Section III during February 2021

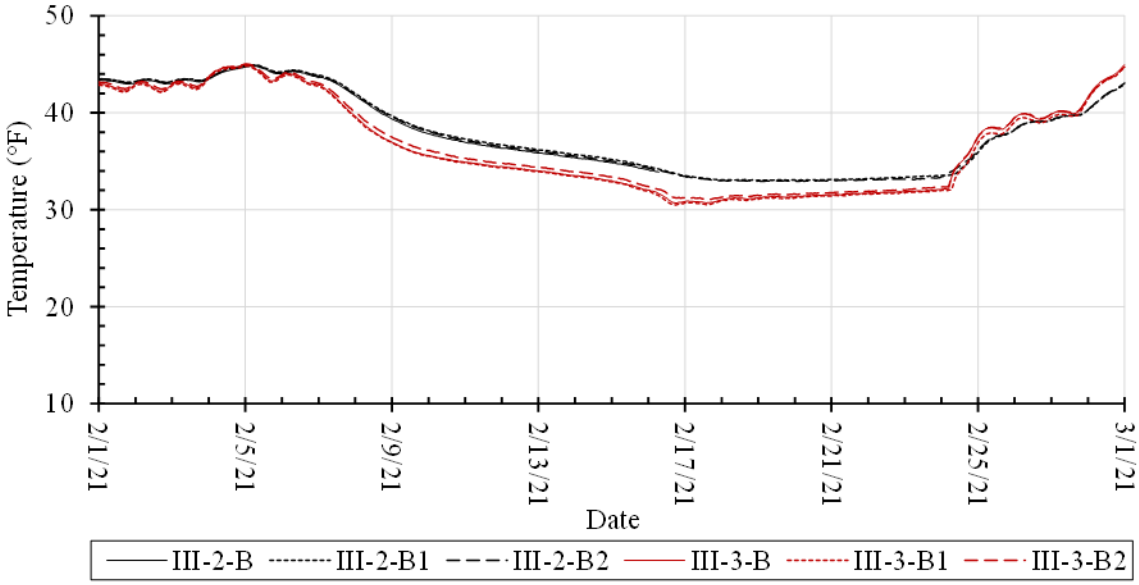

Figure 5.11: Temperature Variations with Distances from the Transverse Joint in Section III during February 2021

Figure 5.12 shows the temperature distributions in Section I and Section III at 12 p.m. on February 15th, 2021. The temperature distributions indicated that the temperature increased with the increase of the depth but the decrease of the distance from the center of the road, which is different from the temperature distributions in the pavement under the hot air temperature condition.

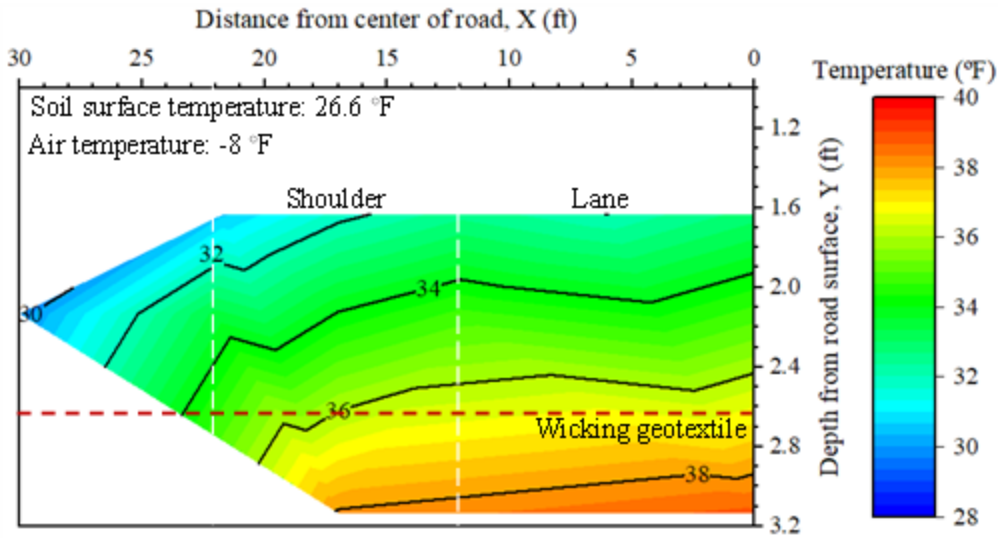

(a) Section I

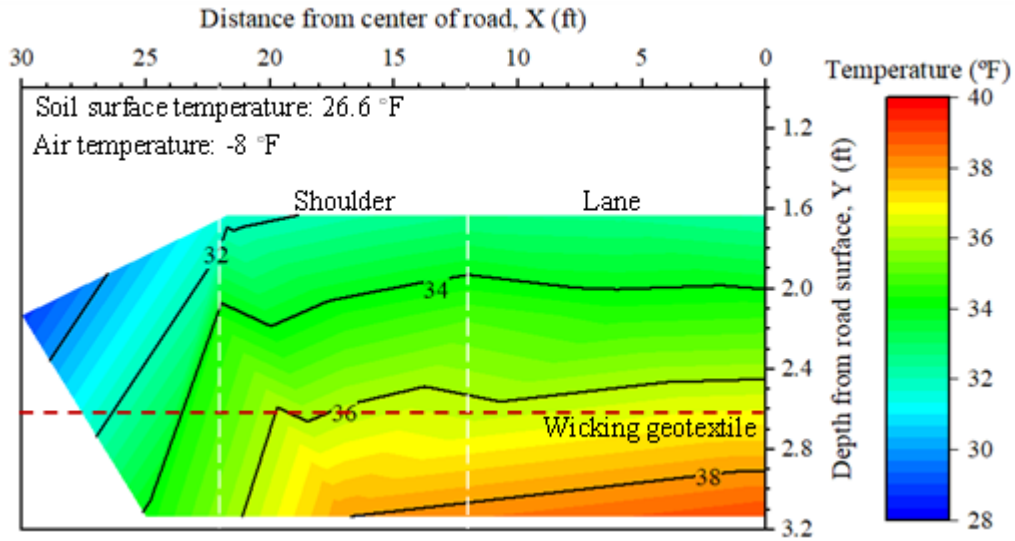

(b) Section III

Figure 5.12: Temperature Distributions in the Pavement at 12 p.m. on February 15th, 2021

5.4 Water Content Variations in Pavement

5.4.1 Causes for Water Content Variations

Before evaluating the monitoring data of volumetric water content (VWC), it is important to understand possible causes for water content increase and decrease in the pavement. The causes for the water content increase are related to the sources for water as discussed in the literature. The causes for the water content decrease are related to lowering of groundwater table, drainage, and

evaporation. Figure 5.13 shows the cross sections and sensors for Section I, Section II, and Section III.

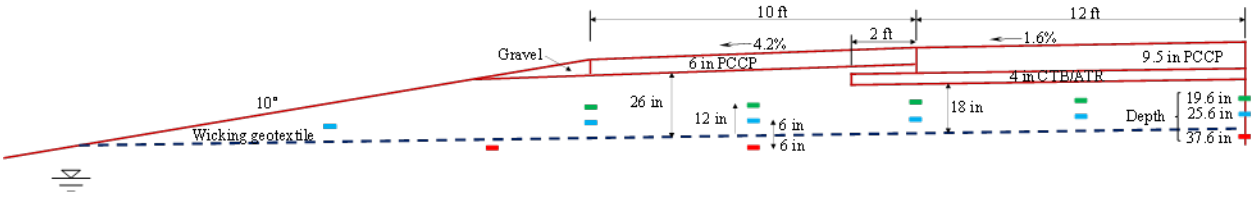

(a) Sections I and III

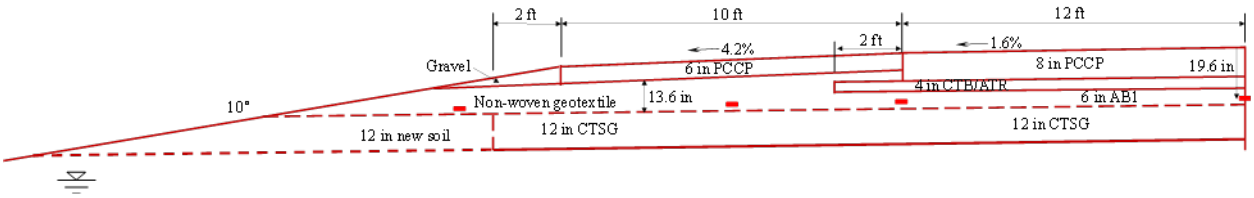

(b) Section II

Figure 5.13: Cross Sections and Sensors in the Pavement Sections

Specific to these test sections, precipitations including rainfalls and snowfalls can generate water. Water from precipitations may infiltrate into the aggregate base and the subgrade through pavement longitudinal and transverse joints between the lane concrete pavements, between the lane pavement and the shoulder concrete pavement, and the rock stone at the edge of the shoulder. Water infiltration and runoff water entering the ditch may raise the groundwater table. In this project site, the steady groundwater table was relatively high and close to the top of the subgrade (i.e., right below the wicking geotextile). The rise of the groundwater table might saturate part of the aggregate base and affect the sensors in the base from Level 2 (middle) to Level 3 (top). Since the AB-1 and AB-3 aggregates had approximately 10% or more fines, capillary rise of water might happen in them. The height of the capillary rise depends on the density and the fines content in the aggregate and the groundwater table level. These test sections were monitored for two and half a years and experienced rainfalls, snowfalls, dry periods, and freeze-thaw periods. These climate conditions affected the variations of the measured VWCs. As discussed later, water freezing in winter made moisture sensors nonfunctional that resulted in low false readings while thaw in early spring increased the VWC readings significantly. The variations of the VWC readings might be induced by different causes that are not necessarily able to be separated and pinpointed exactly.

5.4.2 Short-term Performance of the Wicking Geotextile

To investigate the wicking ability of the wicking geotextile to reduce water contents in aggregate bases, three situations were considered in the analysis. The first situation was to evaluate the changes of water contents in the aggregate bases without and with the concrete pavement from the sensor installation to December 1st, 2018. The second situation was selected to study the performance of the wicking geotextile during the period with continuous and heavy rainfalls from May 18th to June 23rd in 2019, while the third situation was chosen to study the performance of the wicking geotextile under snow and snow melting conditions from January 26th to March 11th in 2021.

5.4.2.1 During and Right after Pavement Construction

To evaluate the performance of the wicking geotextile, volumetric water content (VWC) readings of sensors during the time span from July 24th, 2018, to December 1st, 2018, were analyzed. Figure 5.14 shows the weather condition in Humboldt, Kansas during this period. On August 17th, September 5th, September 7th, October 8th, October 9th, and November 30th, 2018, the daily rainfalls were 1.17, 1.67, 1.45, 1.81, 1.16, and 1.19 in. (29.7, 42.2, 36.8, 46.0, 29.5, and 30.2 mm), respectively. In general, the average daily air temperature was constant from July to September 2018, and then decreased until December 1st, 2018. The relative humidity variated hourly with the air temperature. The relative humidity increased as the air temperature increased from 8:00 a.m. to 6:00 p.m., while the relative humidity decreased as the air temperature decreased from 6:00 p.m. to 8:00 a.m. of the next day.

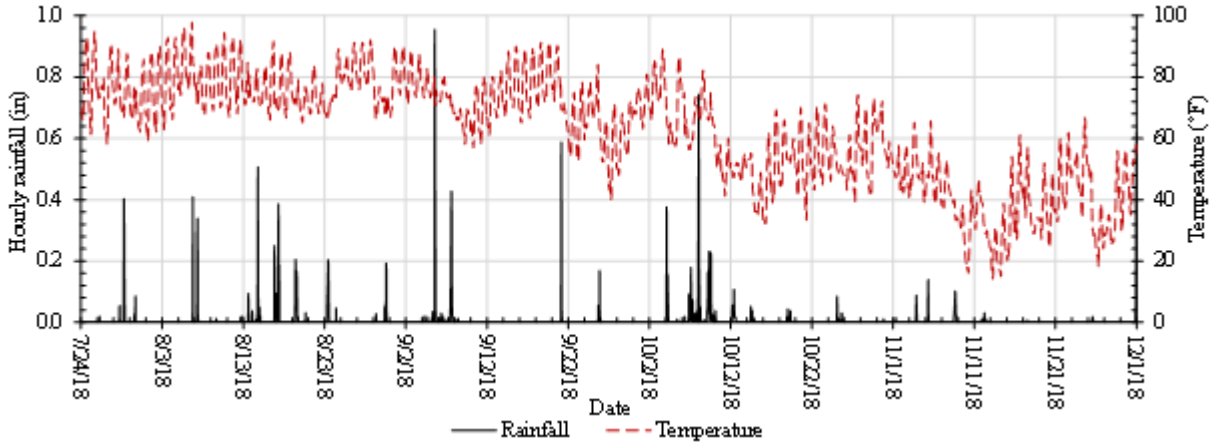

(a) Air Temperature and Hourly Precipitation

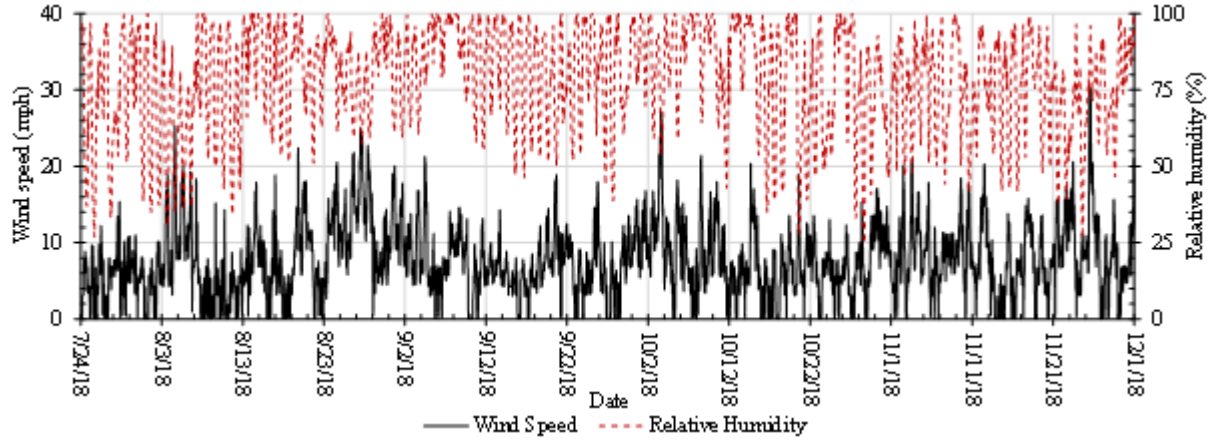

(b) Relative Humidity and Wind Speed

Figure 5.14: Weather Condition from July 24th to December 1st, 2018

The lane pavement was finished on August 21st and 22nd, 2018 while the shoulder pavement was finished on November 2nd, 2018. Figure 5.15(a) shows the changes of VWC readings of the sensors at the first level (i.e., in the subgrade) in Section I. On July 17th, 2018, the VWC readings of Sensor I-1-A and Sensor I-1-D increased rapidly due to the rainfall, but the VWC readings of Sensor I-1-F did not change too much because the soil near Sensor I-1-F next to the drainage ditch was saturated all the time during this period. As a result, rainfalls did not increase the VWC readings of this sensor anymore. Before the concrete pavement was cast, water from the rainfalls could penetrate through the aggregate base and then into the subgrade soil, thus increasing the VWC readings of Sensor I-1-A and Sensor I-1-D. After the lane pavement was cast, water from the rainfall could not reach the soil near Sensor I-1-A directly; therefore, the readings of Sensor

I- 1-A did not change with the rainfall. However, before the construction of the shoulder pavement on November 2nd, 2018, water from the rainfall penetrated the aggregate base and then reached the soil near Sensor I-1-D, thus changing the VWC readings of Sensor I-1-D until November 2nd, 2018. One thing to point out is that the subgrade was a fine-grained soil, and the wicking geotextile was not able to reduce the water content of the subgrade by the wicking action.

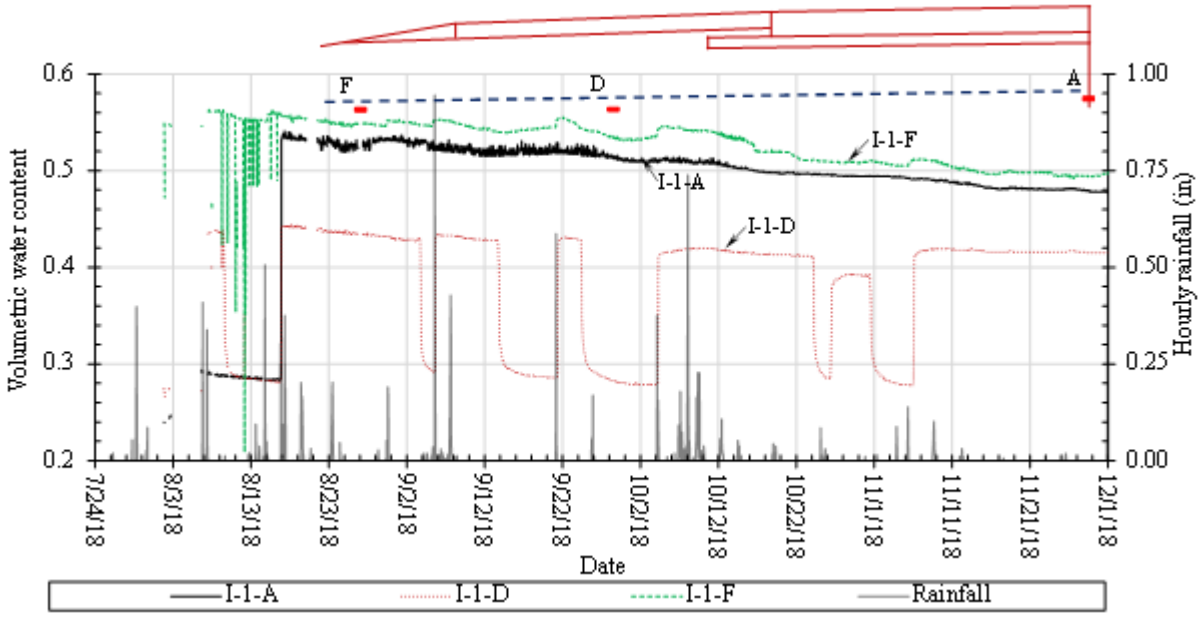

(a) At the Elevation of 6 in. below the Wicking Geotextile

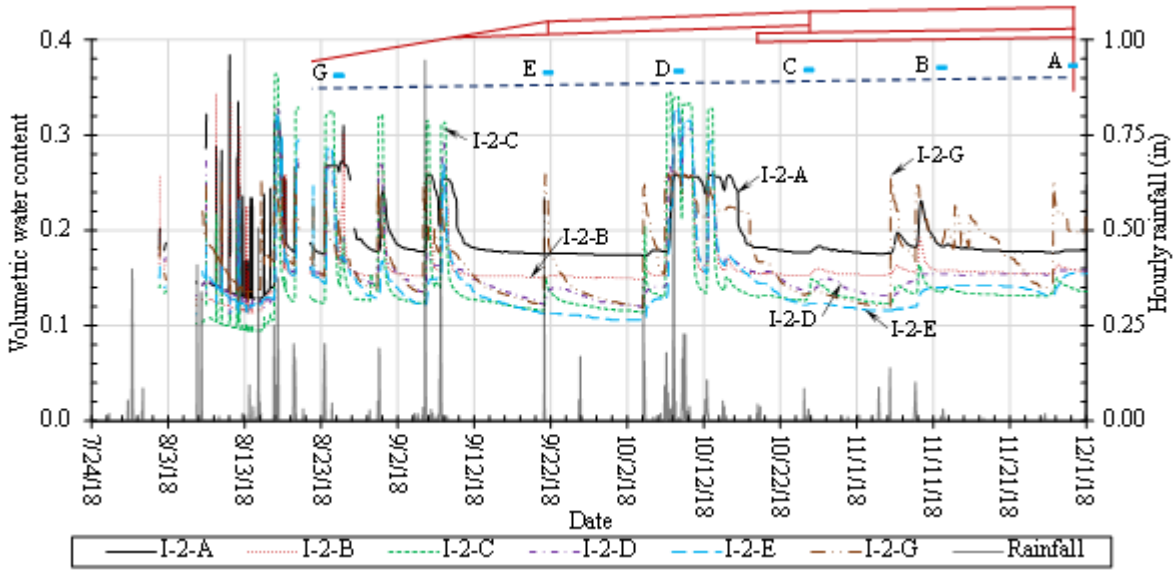

(b) At the Elevation of 6 in. above the Wicking Geotextile

Figure 5.15: VWC Readings in Section I from July 24th to December 1st, 2018

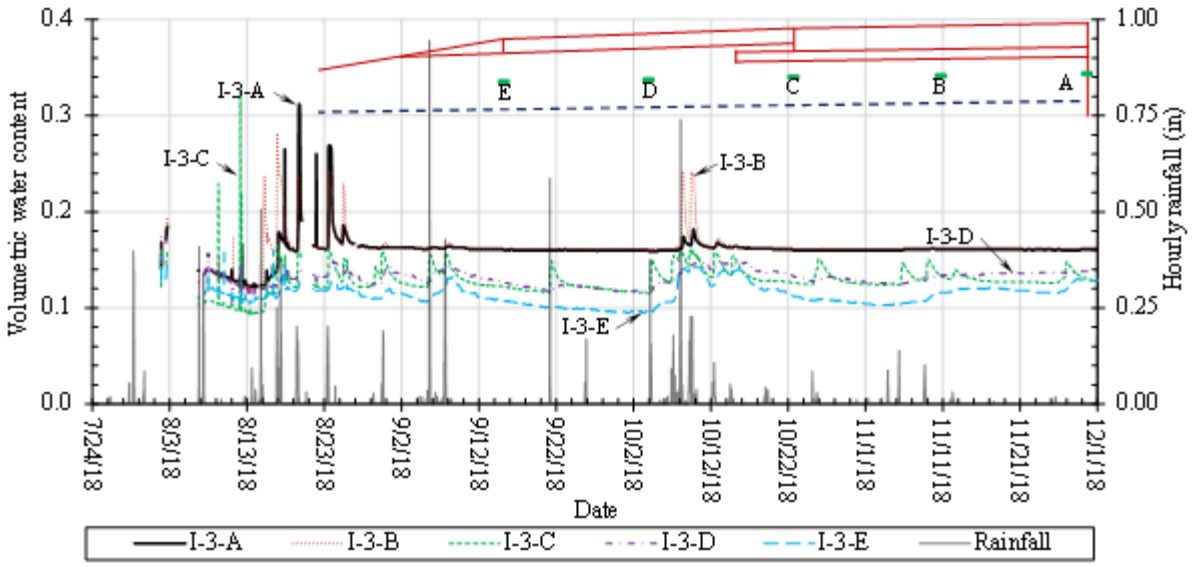

(c) At the Elevation of 12 in. above the Wicking Geotextile

Figure 5.15: VWC Readings in Section I from July 24th to December 1st, 2018 (Continued)

Figure 5.15(b) shows the VWC readings of the sensors in the second level (i.e., above the wicking geotextile and in the aggregate base) in Section I. After the lane pavement was cast on August 21st and 22nd, 2018, theoretically speaking, water from the rainfall within the lane pavement would flow transversely down the transversal slope of the pavement, resulting in limited changes in the VWC readings of the sensors at this level if water infiltration was the main course. However, Figure 5.15(b) shows that the VWC readings of the sensors at this level increased rapidly after rainfalls and reached more than 26%. As calculated in Chapter 4, the average saturated VWC for the AB-1 aggregate in Section 1 was 20.6%, indicating the aggregate at this level was saturated due to the rise of the groundwater table. After the rainfalls and during the non-rainfall (drying) period, the VWC readings decreased quickly due to drainage and lowering of the groundwater table. In addition, the VWC readings of Sensor I-2-A and Sensor I-2-B did not increase after the rainfalls on September 21st and 25th. This is because the rainfalls were short or light, the rise of the groundwater table did not reach to the levels of Sensor I-2-A and Sensor I-2-B. During the period from October 4th to 15th, continuous precipitations with limited drying days increased the groundwater table to the soil levels near Sensor I-2-A and Sensor I-2-B, thus increasing their VWC readings.

Figure 5.15(c) shows the VWC readings of the sensors at the third (top) level in Section I. The lane pavement was completed on August 21st and 22nd, 2018. Before the lane pavement was cast, the VWCs measured by Sensor I-3-A and Sensor I-3-B reached the saturated VWC after rainfalls due to water infiltration. After the lane pavement was constructed, however, the VWC readings of Sensor I-3-A and Sensor I-3-B did not change with rainfalls after August 25th, 2018, except for the period from October 8th to 10th, 2018. Due to the continuous rainfalls from October 4th to 8th, the groundwater rose or the capillary action from the increased water table increased the VWC readings of Sensor I-3-A and Sensor I-3-B. The VWC readings for Sensor I-3-B increased more significantly than Sensor I-3-A due to its lower elevation than Sensor I-3-A. The VWC readings of Sensor I-3-C changed with the rainfall even after the construction of the shoulder pavement, indicating water due to the rainfall could infiltrate through the joint between the lane pavement and the shoulder pavement, increasing the VWC readings of Sensor I-3-C.

Figure 5.16 shows the VWC readings of the sensors in Section II. Before the construction of the lane pavement, the VWC readings of all the sensors increased with the rainfalls due to water infiltration and then decreased during the drying period following the rainfalls. After the construction of the lane pavement, the VWC readings of Sensor II-3-A did not change with the rainfalls unless the continuous rainfalls increased the groundwater table high enough to increase the water content of the soil near this sensor. For example, the continuous rainfall from October 4th to 8th increased the water table and the capillary action increased the VWC readings of Sensor II-3-A. After the construction of the shoulder pavement on November 2nd, 2018, the VWC readings of Sensor II-3-C and Sensor II-3-D did not change with the rainfalls because water from rainfalls flowed down the pavement and then into the drainage ditch. The comparison of the VWC readings of Sensor I-3-C and Sensor II-3-C with the rainfalls after November 2nd, 2018, indicates that the quality of the joint between the shoulder and the lane was not the same for these two sections.

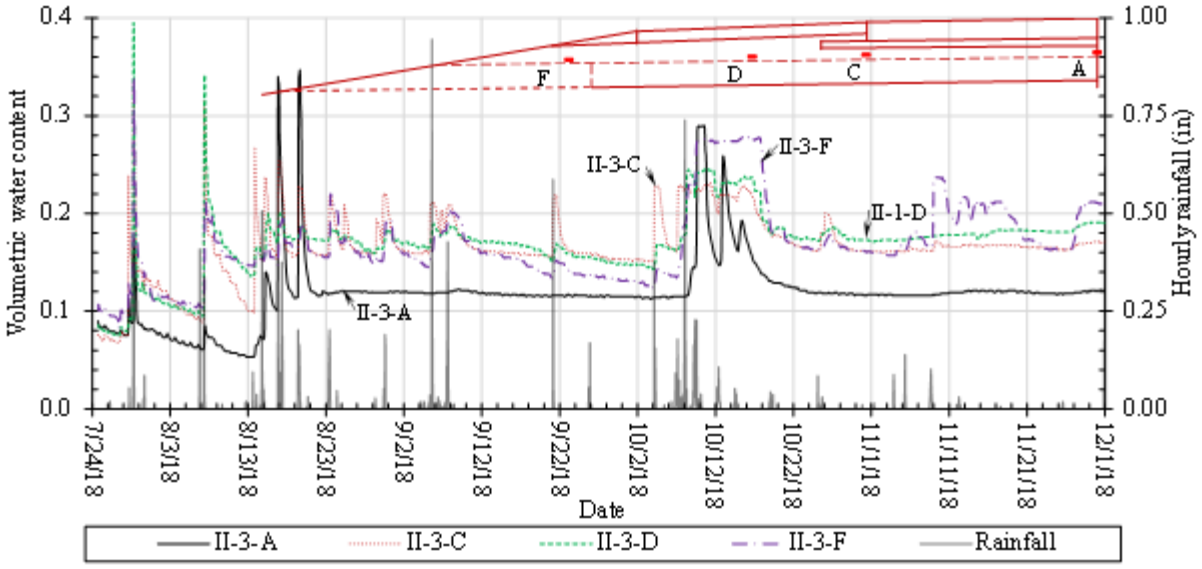

Figure 5.16: VWC Readings in Section II from July 24th to December 1st, 2018

Figure 5.17 shows the VWC readings of the sensors in Section III during the same period. The VWC reading changes with precipitations in Section III had similar patterns to those in Section I. For example, the VWC in the subgrade soil did not change too much with rainfalls since the subgrade soil was a fine-grained soil and nearly saturated. The AB-3 aggregate at the second level after heavy rainfalls or continuous rainfalls reached the saturated condition due to the rise of the groundwater table because the measured VWCs were higher than the saturated VWC as determined in Chapter 4. However, different aggregate materials contributed to some different responses between Section I and Section III. For instance, the VWC readings of the sensors at the second level in Section III were more sensitive to rainfalls than those in Section I because the base material (AB-3) in Section III had more small particles than the AB-1 aggregate in Section I. Therefore, it was more likely for the AB-3 aggregate to have more capillary rise effect from the rising groundwater table. After the VWC readings reached the peak values due to rainfalls, they dropped more quickly in Section I than Section III because the AB-1 aggregate was more permeable to have faster drainage. However, the VWCs of the AB-3 aggregate at the third level in Section III maintained lower values than those of the AB-1 aggregate in Section I because the AB- 3 aggregate allowed less water infiltration than the AB-1 aggregate.

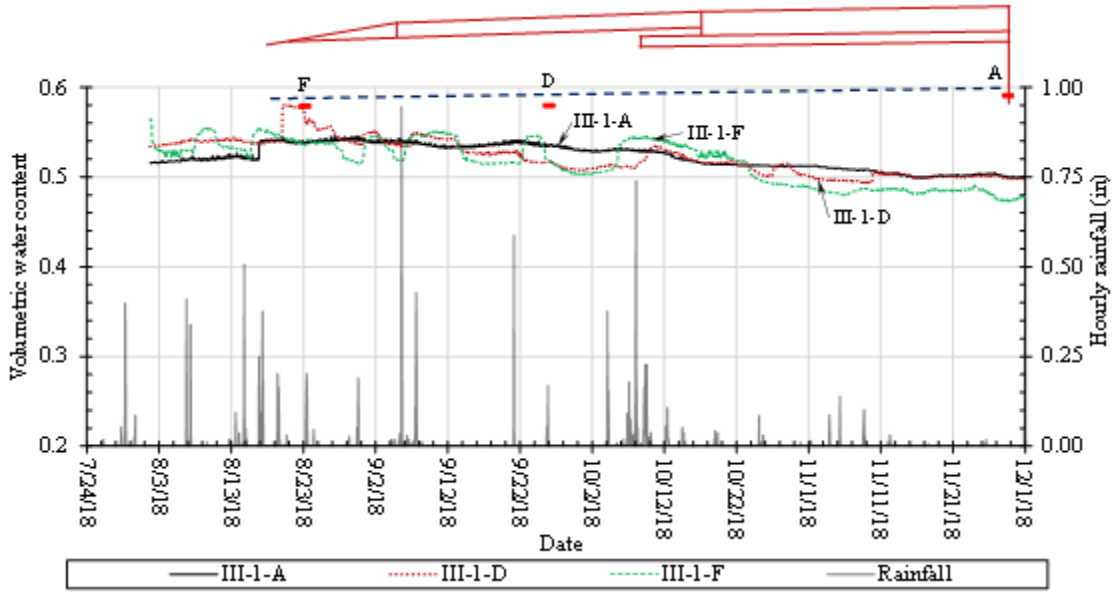

(a) At the Elevation of 6 in. below the Wicking Geotextile

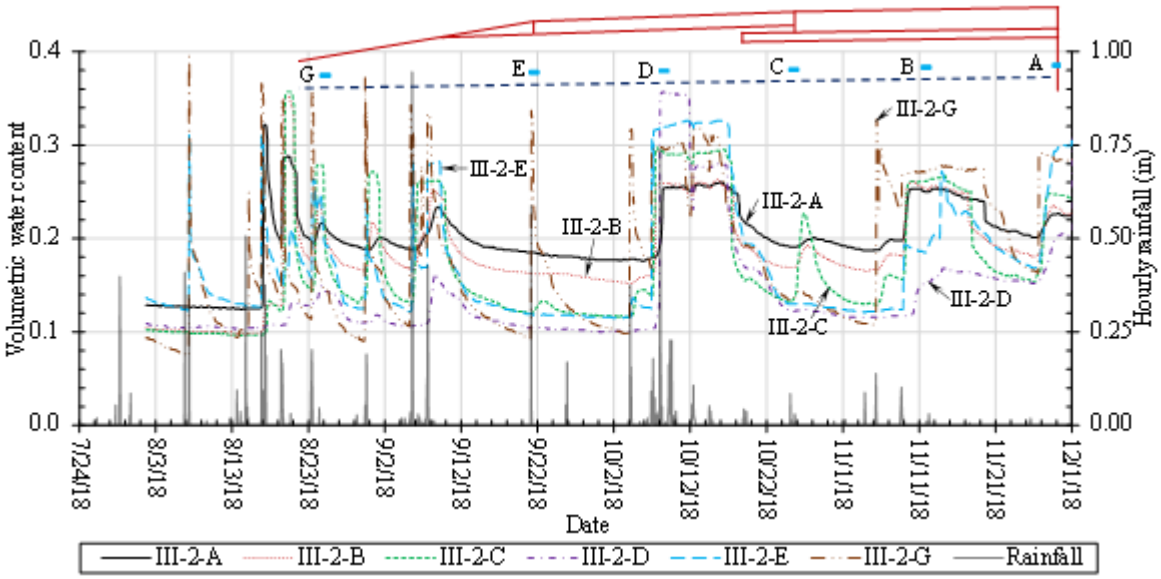

(b) At the Elevation of 6 in. above the Wicking Geotextile

Figure 5.17: The VWC Readings in Section III for July 31st to December 1st, 2018

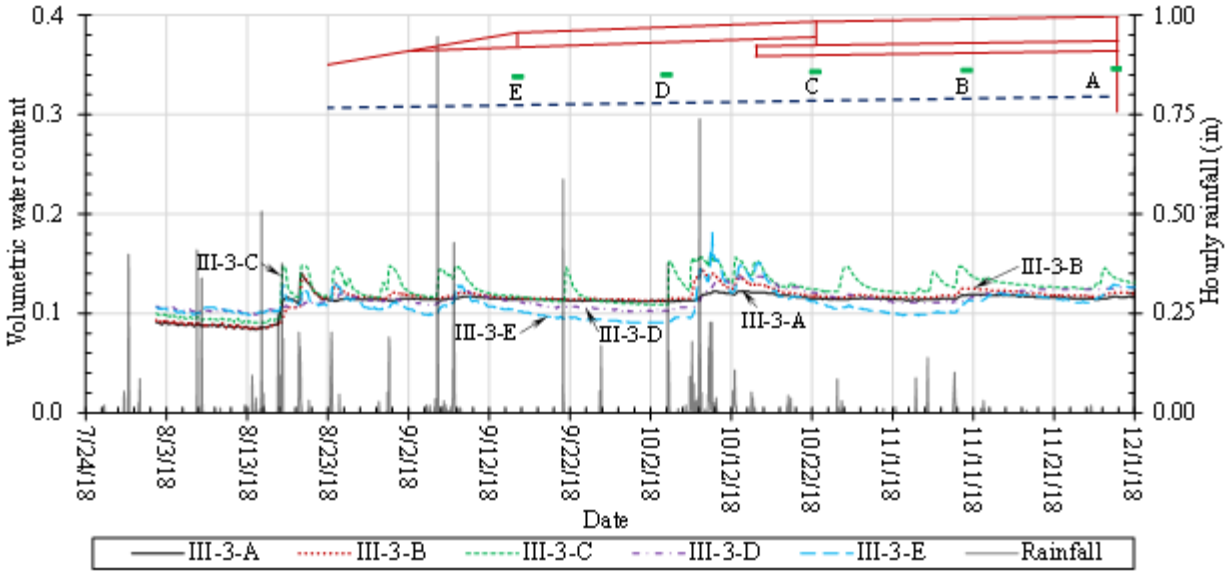

(c) At the Elevation of 12 in. above the Wicking Geotextile

Figure 5.17: The VWC Readings in Section III July 31st for to December 1st, 2018 (Continued)

Figure 5.18 shows the comparison of the readings from the sensors at the distances of 0, 12, and 17 ft (0, 3.6, and 5.1 m) from the centerline of the road at the same elevation (the top level) in the three sections. After the construction of the lane pavement on August 21st and 22nd, 2018, the VWC readings of the sensors at the distances of 0 and 12 ft (0 and 3.6 m) were more sensitive to the rainfalls in Section I and Section II than those in Section III. This phenomenon is because both Section I and Section II used more permeable AB-1 aggregate to water infiltration, while Section III used less permeable AB-3 aggregate. After the construction of the shoulder pavement, however, the VWC readings of the sensors at the distance of 12 ft (3.6 m) were more sensitive to continuous light rainfalls in Section I and Section III than those in Section II. For instance, due to the continuous light rainfalls from November 3rd to 9th, the VWC readings of the sensors in Section I and Section III increased and then decreased, but the sensors in Section II did not increase. However, the VWC readings in Section II remained at the high level so that limited water infiltration did not change the readings much. On the other hand, the aggregates in Section I and Section III were relatively dry and more likely to attract water when available. In addition, the VWC readings of the sensors in both Section I and Section III decreased quite quickly after each

precipitation, indicating the benefits of the wicking geotextile in removing water from the aggregate bases.

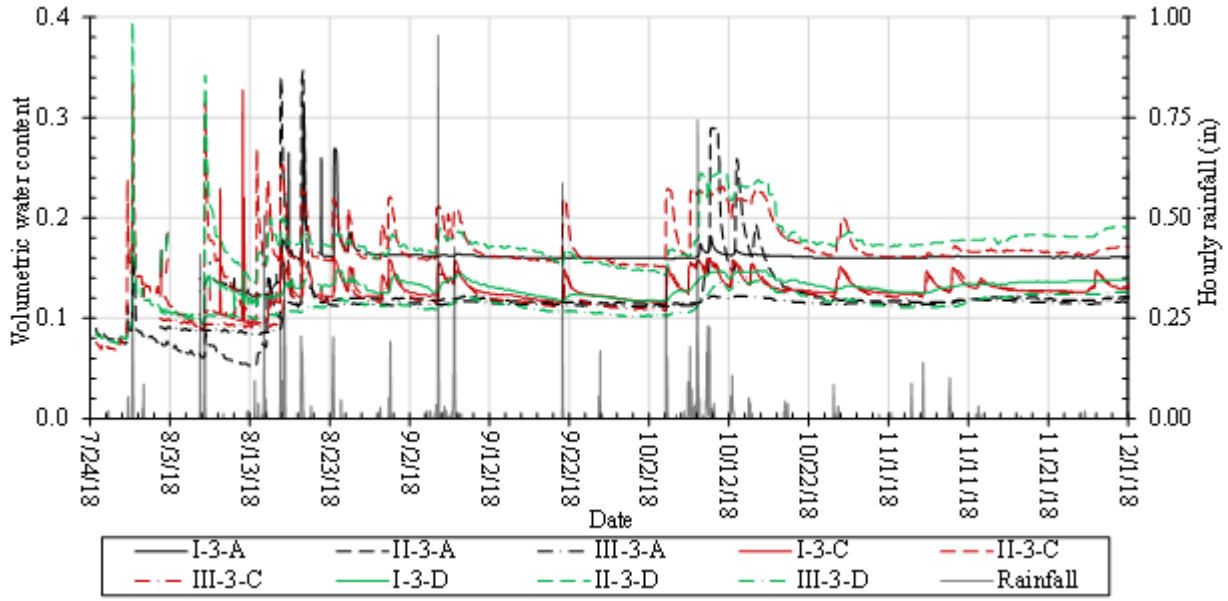

Figure 5.18: VWC Readings in the Three Sections from July 24th to December 1st, 2018

5.4.2.2 Continuous and Heavy Precipitations

Figure 5.19 shows the weather condition in Humboldt, Kansas from May 18th to June 12th, 2019. The maximum daily rainfall was 3.54 in. (90 mm) on May 20th, 2019, with the maximum hourly precipitation of 1.57 in. (40 mm). Continuous and heavy rainfalls happened during the period from May 18th to 28th, 2019, and the total rainfall during this period was 11.69 in. (297 mm), followed by 15 days without any heavy rainfall. The average daily air temperature, daily wind speed, and daily humidity were 72.41 °F (22.45 °C), 9.0 mph (14.4 km/h), and 71.03%, respectively.

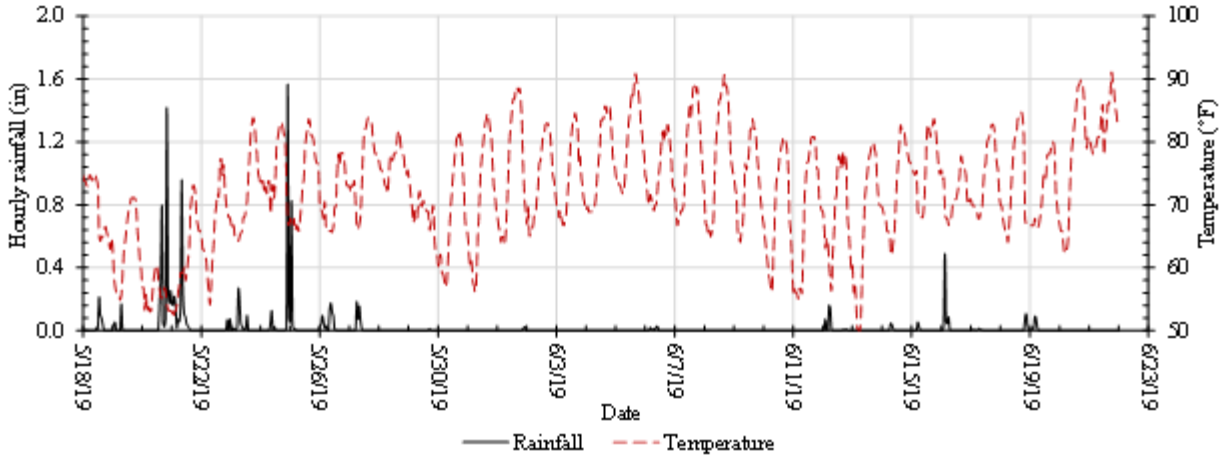

(a) Air Temperature and Hourly Precipitation

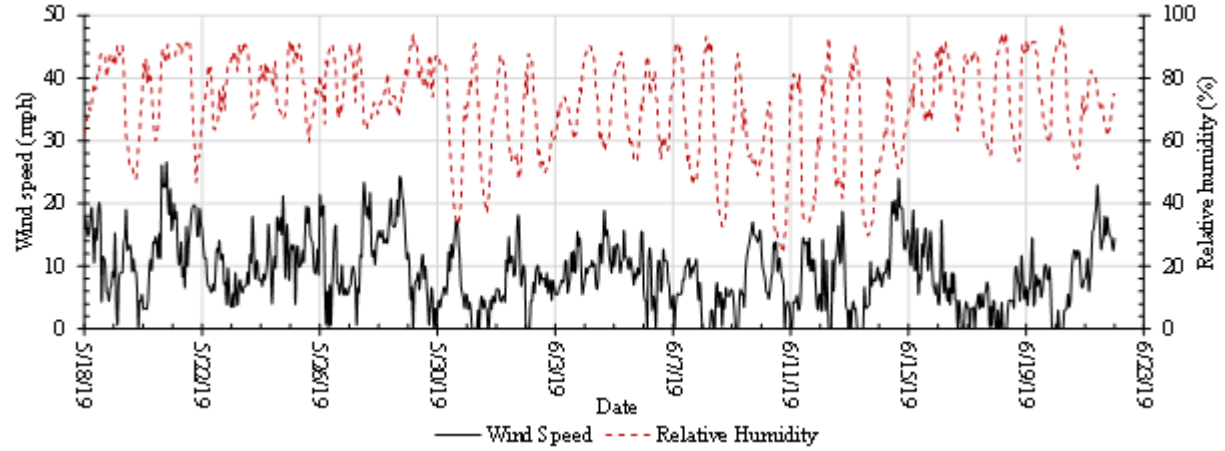

(b) Relative Humidity and Wind Speed

Figure 5.19: Weather Condition from May 18th to June 21st, 2019

Figure 5.20 shows the VWC and temperature readings of the sensor buried under the soil surface. The rainfall happened from noon (12 p.m.) on May 20th to 3 p.m. on May 21st, 2019, and then continued from 8 p.m. on May 22nd to 1 p.m. on May 23rd, 2019. Figure 5.20 shows the VWC readings in the soil reached its highest value (i.e., saturation) at 11 p.m. on May 21st and then the VWC reading dropped after 5 p.m. on May 22nd, 2019. However, the effect of the rainfall from May 22nd to May 23rd, 2019, on the VWC readings was not significant. Since the surface soil was a fine-grained soil and had low permeability, it was slow for water to infiltrate it during the short heavy rainfall. However, continuous light rainfalls could have more effect on the VWC readings under the soil surface than short heavy rainfalls. This explains why the VWC readings changed more obviously after May 26th, 2019, than those from May 23rd to 24th, 2019. After each rainfall,

the VWC readings under the soil surface decreased gradually due to evaporation. In addition, the VWC readings fluctuated slightly with the hourly air temperature. Dew on grass might fall on the soil at night and then the soil surface dried during daytime. This process might cause slight hourly fluctuations of the VWC readings with the air temperature under the soil surface.

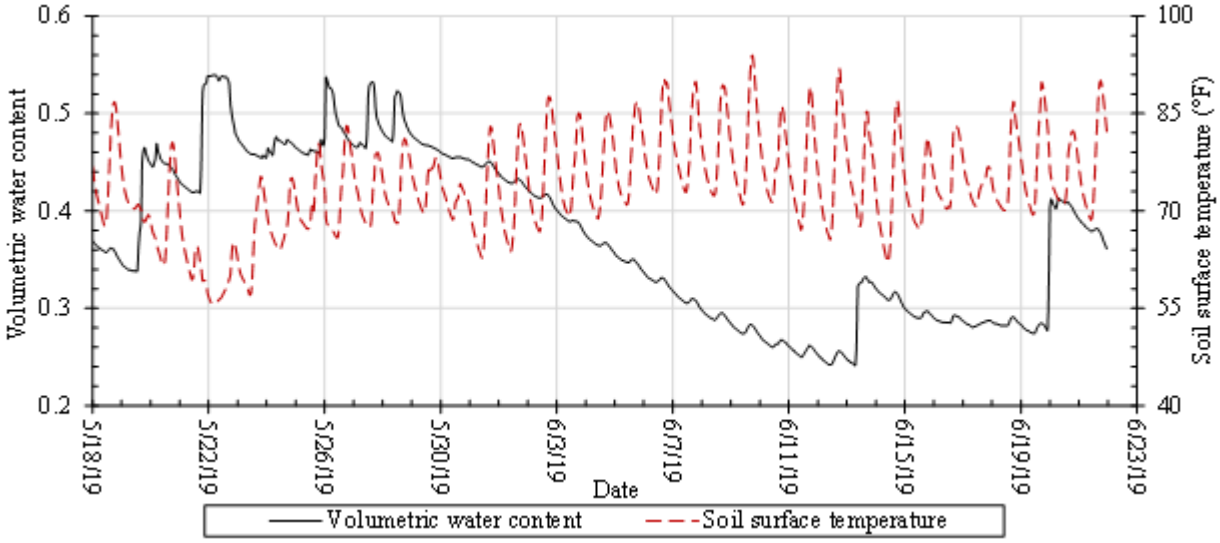

Figure 5.20: VWC and Temperature Readings of the Sensor under the Soil Surface

Figure 5.21 shows the VWC reading changes in Section I during the period from May 18th to June 22nd, 2019. Figure 5.21(a) shows that the VWC readings in the subgrade soil did not change much with time as discussed earlier. Figure 5.21(b) shows the readings of the sensors at 6 in. (0.15 m) above the wicking geotextile in the AB-1 aggregate base. The VWC readings of Sensor I-2-A, Sensor I-2-B, Sensor I-2-C, and Sensor I-2-D increased with the increasing water table due to the continuous and heavy rainfalls from May 18th to 28th, 2019. Since Sensor I-2-E and Sensor I-2-G were not covered by the concrete pavement, water infiltrated into the soil near these two sensors during the rainfalls. As a result, the VWC readings of these two sensors were much more sensitive to the rainfalls than those of other sensors. Furthermore, after the drying period from May 28th to June 12th, 2019, the rainfalls from June 12th to 20th, 2019 did not increase the water table to the elevation to affect the VWC readings of Sensor I-2-A, Sensor I-2-B, and Sensor I-2-C significantly. Figure 5.21(c) shows the VWC readings of the sensors in the AB-1 aggregate base and at 12 in. (0.3 m) above the wicking geotextile. Due to the higher elevations of these sensors,

the increasing water table could not reach this level so that it did not affect the VWC readings of Sensor I-3-A, Sensor I-3-B, and Sensor I-3-C significantly. Since the elevation of Sensor I-3-E was lower, closer to the drainage ditch than other sensors, and covered by the rock stone, its VWC readings were affected by the increasing water table and/or water infiltration due to the rainfalls.

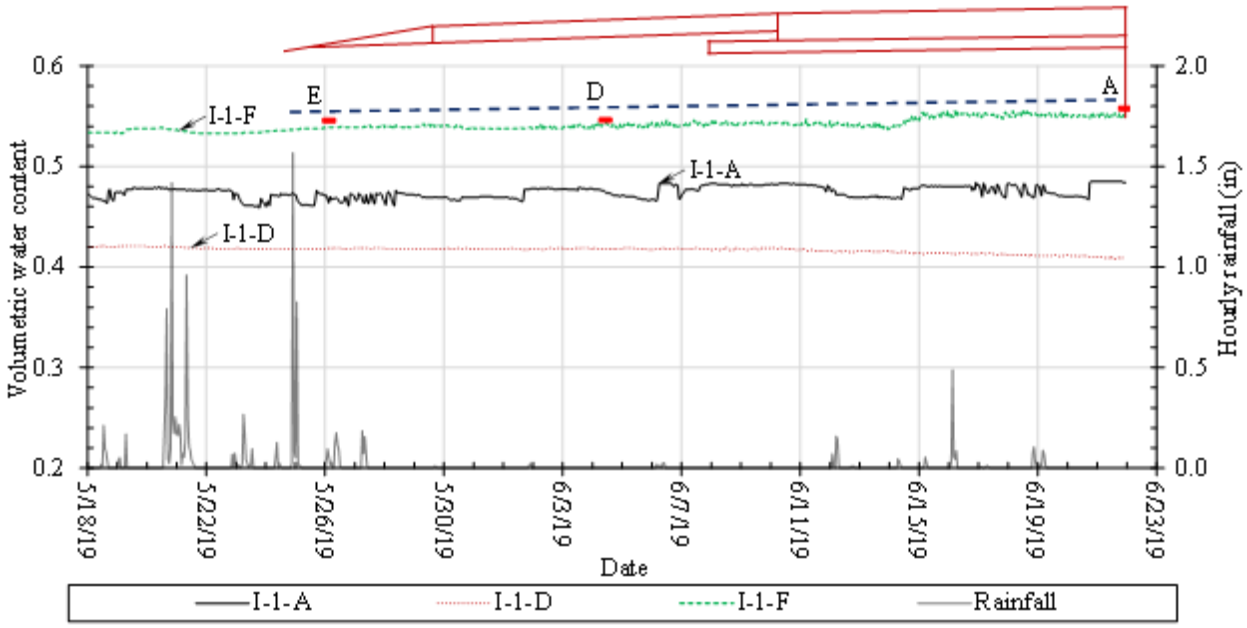

(a) At the Elevation of 6 in. below the Wicking Geotextile

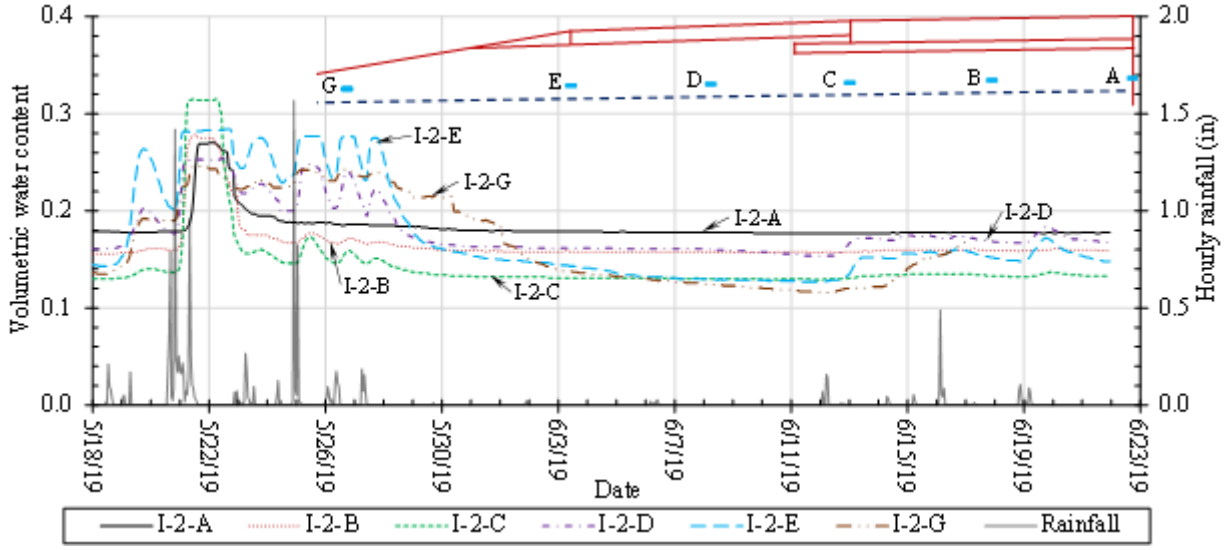

(b) At the Elevation of 6 in. above the Wicking Geotextile

Figure 5.21: VWC Changes in Section I from May 18th to June 22nd, 2019

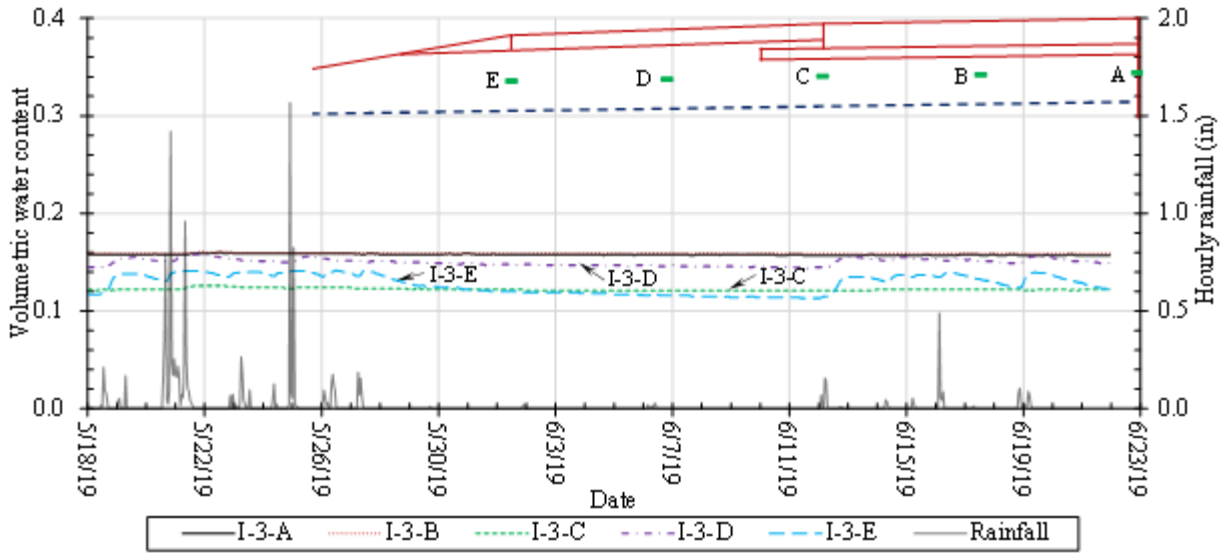

(c) At the Elevation of 12 in. above the Wicking Geotextile

Figure 5.21: VWC Changes in Section I from May 18th to June 22nd, 2019 (Continued)

Figure 5.22 shows the VWC changes from the sensors in Section II. Since Sensor II-3-F was under the side slope of the road without any concrete pavement, water from the rainfall and the pavement infiltrated into the soil near this sensor, thus increasing its VWC readings. In addition, the VWC readings of Sensor II-3-F fluctuated with the rainfall more significantly than other sensors because water was more easily reaching this sensor. The VWC readings of Sensor II-3-F and Sensor II-3-D reached their peak values at 6 p.m. on May 20th, 2019, while the VWC readings of Sensor II-3-C reached its peak value at 11 a.m. on May 22nd, 2019, due to the rainfalls on May 20th and 21st. Since Sensor II-3-F had a lower elevation than Sensor II-3-A due to the transverse slope and was covered by the rock stone, the capillary rises due to the rising water table due to continuous rainfalls increased the VWC readings of Sensor II-3-F, Sensor II-3-D, Sensor II-3-C, and Sensor II-3-A sequentially. The aggregates at Sensor II-3-F, Sensor II-3-D, Sensor II-3-C were close to saturation. After reaching their peak values, the VWC readings of all the sensors fluctuated with the water table due to rainfalls. After the continuous precipitations from May 8th to May 27th, 2019, the VWC readings of Sensor II-3-A, Sensor II-3-C, Sensor II-3-D, and Sensor II-3-F decreased sequentially due to the decreasing water table as shown in Figure 5.22. The rainfalls on and after June 12th, 2019, increased the VWC readings of Sensor II-3-F and Sensor II-3-D more significantly than those of Sensor II-3-C and Sensor II-3-A. Evaporation and drainage lowered the

water table from May 28th to June 12th, 2019. Even though there were rainfalls from June 12th to 20th, they were not heavy and long enough to raise the water table to the elevation to affect their VWC readings of Sensor II-3-A and Sensor II-3-C significantly. However, capillary action from the higher water table after rainfalls during this period increased the water contents of the soil near Sensor II-1-A and Sensor II-1-C slightly.

Sensor II-3-A and Sensor II-3-C were located under the joint between the left lane and the right lane, and the joint between the lane and the shoulder, respectively. Water from rainfalls was expected to flow from the center of the road, over the joint between the lane and the shoulder, and then over the side slope into the drainage ditch. Theoretically speaking, Sensor II-3-C should be more affected by water infiltration through the joint than Sensor II-3-A, because less water was expected to flow over the joint between the left lane and the right lane than that over the joint between the lane and the shoulder. However, the VWC readings of Sensor II-3-A and Sensor II- 3- C did not change significantly with the precipitations from June 12th to 20th, 2019, indicating the good-quality joints that might have minimized water from infiltrating into the pavement structure.

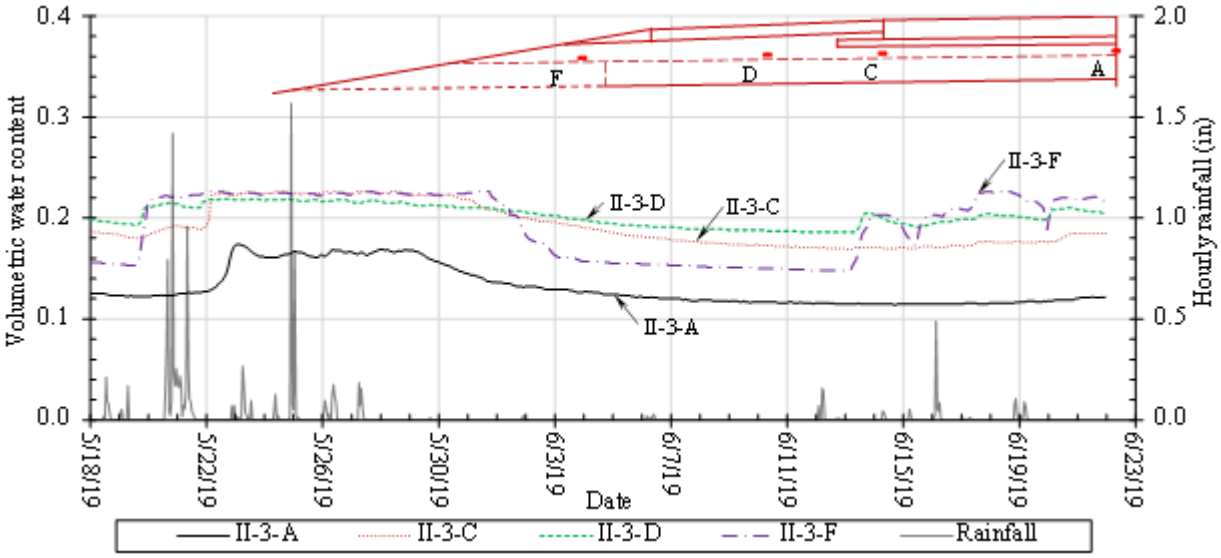

Figure 5.22: VWC Changes in Section II from May 18th to June 22nd, 2019

Figure 5.23 shows the VWC changes in Section III during the same period as discussed above. The VWC readings of the sensors in Section III changed in the similar pattern as those in

Sections I. For example, the VWC readings for the sensors in the subgrade did not vary much as shown in Figure 5.23(a). Figure 5.23(b) shows that the VWC readings increased and reached the similar values of moisture contents (saturation) sequentially from Sensor III-2-G, Sensor III-2-E, Sensor III-2-D, Sensor III-2-C, Sensor III-2-B, and Sensor III-2-A from May 18th to May 22nd. This result indicates the groundwater rose gradually to the elevation where Sensor III-2-A was located. During June 12th to 20th, the similar situation happened to the VWC readings of Sensor III-2-G, Sensor III-2-E, and Sensor III-2-D during the rainfalls, but not to Sensor III-2-C, Sensor III-2-B, and Sensor III-2-A, the readings of which increased gradually but did not reach the high level (i.e., not saturated). The gradual increases of these VWC readings might be attributed to capillary rise from the groundwater table. For the sensors at Level 3 as shown in Figure 5.23(c), the increases of the VWC readings were mostly caused by water infiltration from the surface after rainfalls. Since Sensor III-3-E was at the interface between the rock cover and the concrete shoulder, it was easily accessed by water infiltration so that its VWC readings increased with the rainfalls. Then water flowed from Distance E to Distance D when Sensor III-3-D was located. The increase of the VWC readings at Sensor III-3-C and Sensor III-3-B were likely caused by water infiltration from the joint above Sensor III-3-C.

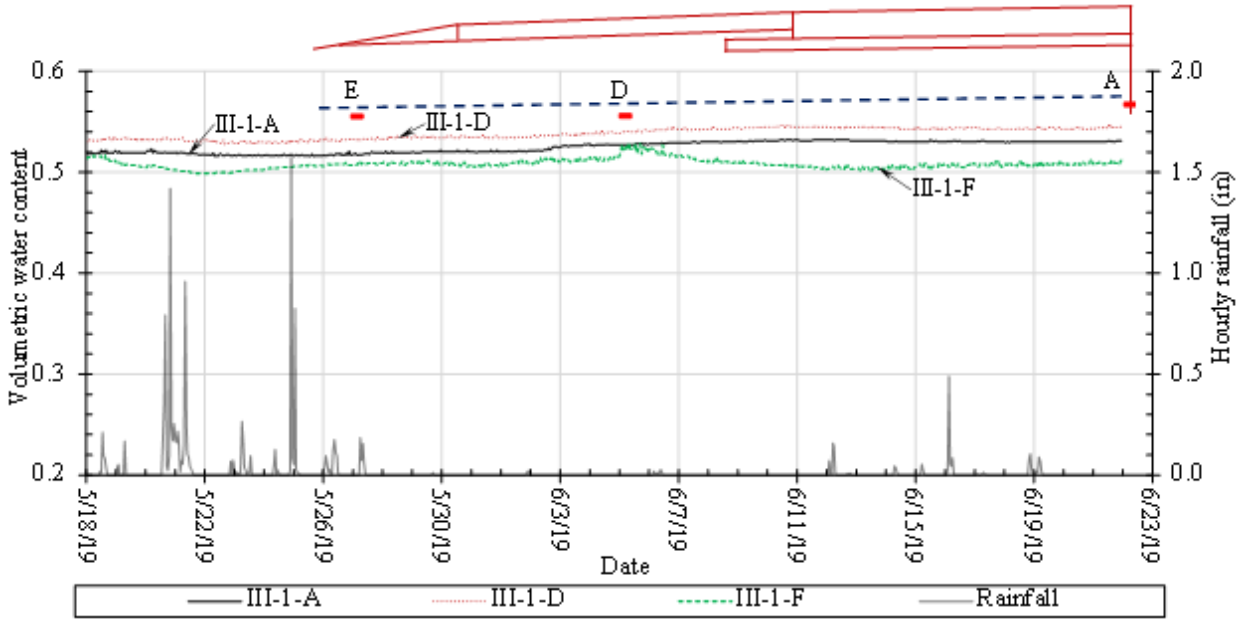

(a) At the Elevation of 6 in. below the Wicking Geotextile

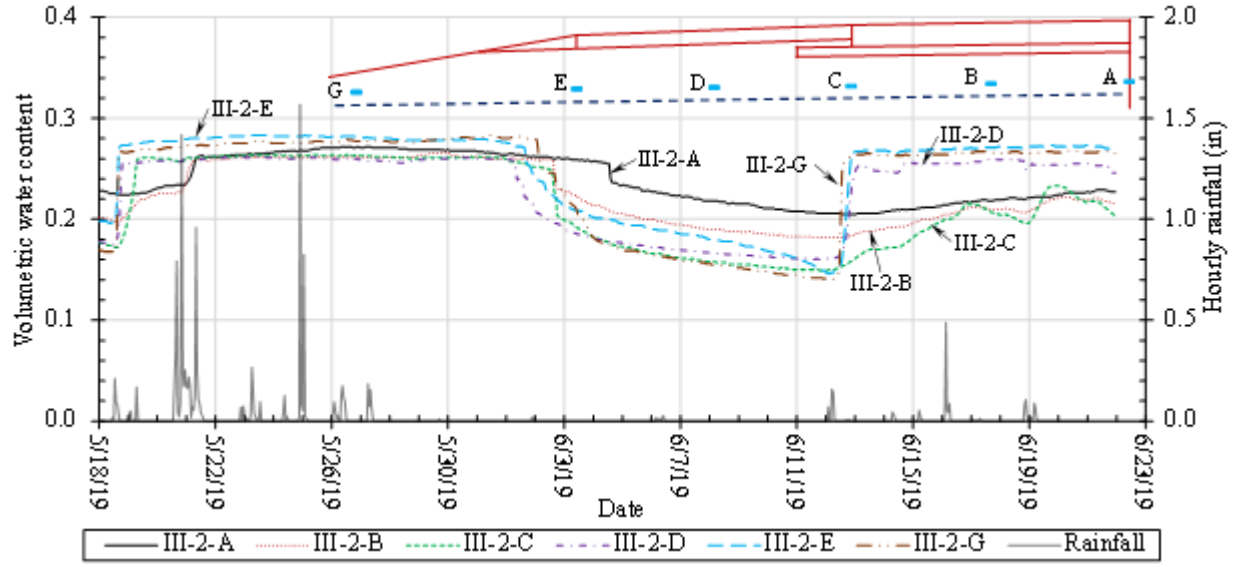

(b) At the Elevation of 6 in. above the Wicking Geotextile

Figure 5.23: VWC Changes in Section III from May 18th to June 22nd, 2019

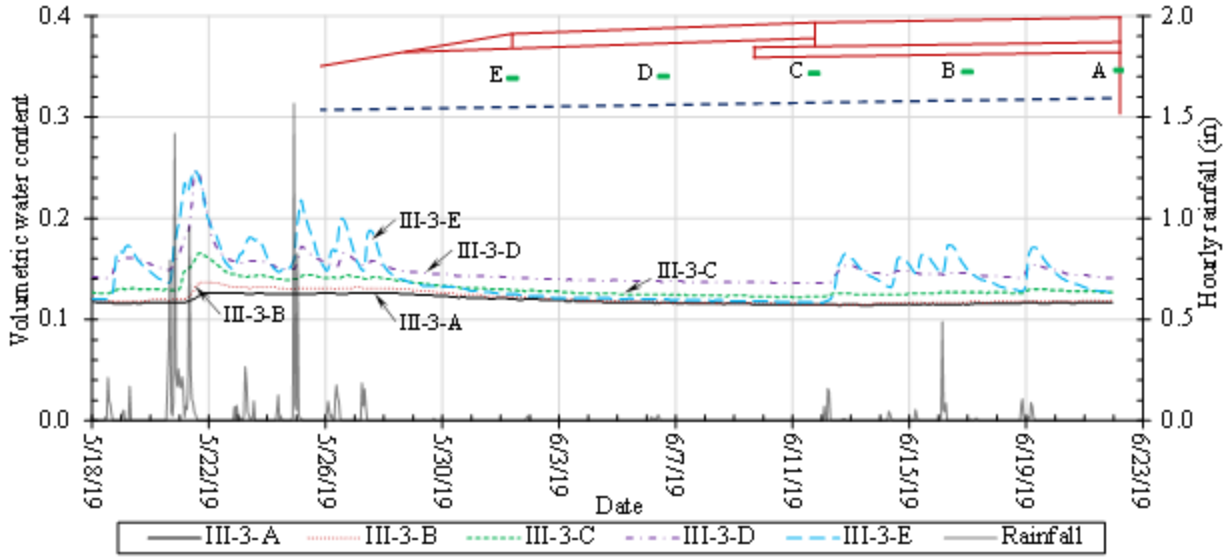

(c) At the Elevation of 12 in. above the Wicking Geotextile

Figure 5.23: VWC Changes in Section III from May 18th to June 22nd, 2019 (Continued)

Figure 5.24 shows the comparisons of the VWC readings of the sensors at the same top elevation in the three sections. Even though Sensor III-3-D and Sensor III-3-E reached the highest VWCs (close to saturation) on May 21st, 2018, the VWC readings in Section I and Section III were generally lower than those in Section II, indicating the benefits of the wicking geotextile used in both Section I and Section III.

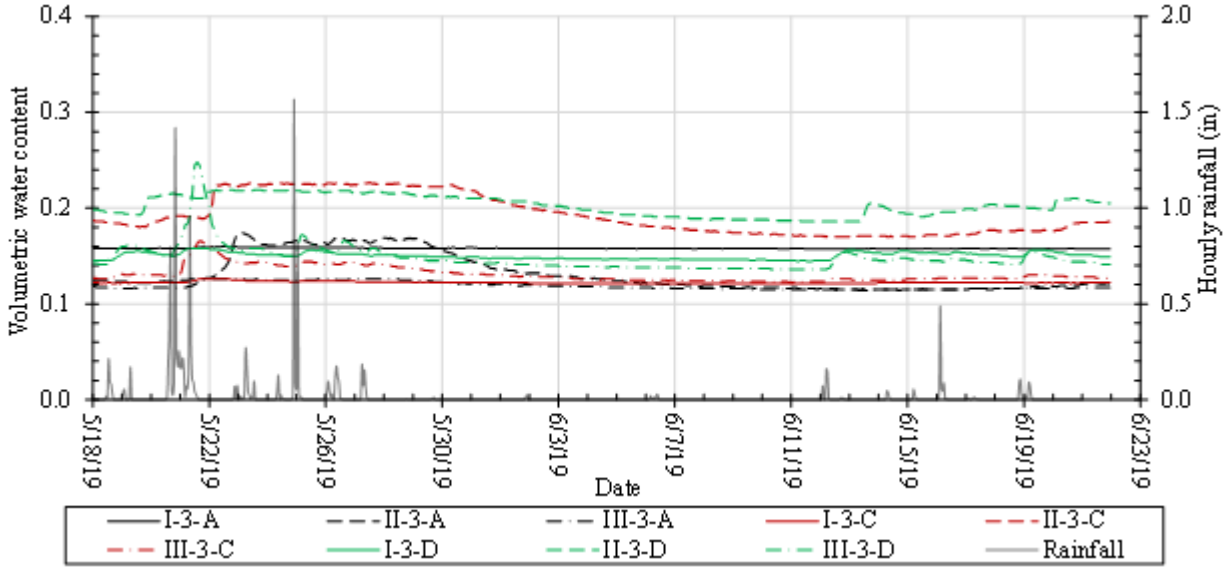

Figure 5.24: VWC Readings in the Three Sections from May 18th to June 23rd, 2019

5.4.2.3 Snowfall and Snow Melting

Figure 5.25 shows the weather condition in Humboldt, Kansas from January 26th, 2021, to March 11th, 2021. The air temperature was below 32 °F (0 °C) during the period from February 6th to 20th, 2021. The maximum daily rainfall was 1.3 in. (33 mm) on January 30th with the maximum hourly rainfall of 0.17 in. (4.4 mm). The maximum daily snowfall was 0.22 in. (5.52 mm) on February 14th, 2021, and the maximum hourly snowfall was 0.18 in. (4.68 mm) on February 22nd, 2021. The average daily air temperature, daily wind speed, and daily humidity were 34.34 °F (1.3 °C), 10.6 mph (17 kph), and 66.2%, respectively during this period.

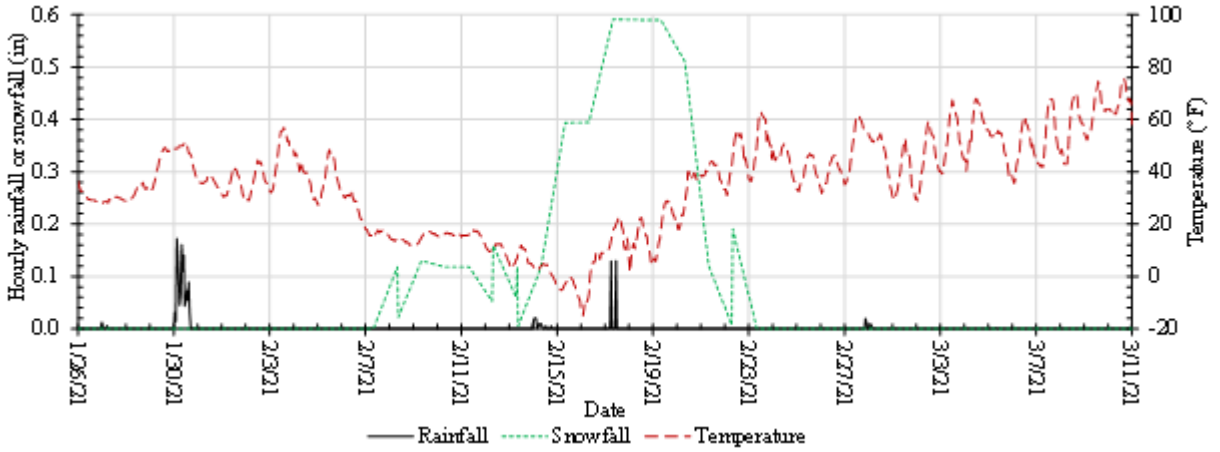

(a) Air Temperature, Hourly Snowfall, and Hourly Rainfall

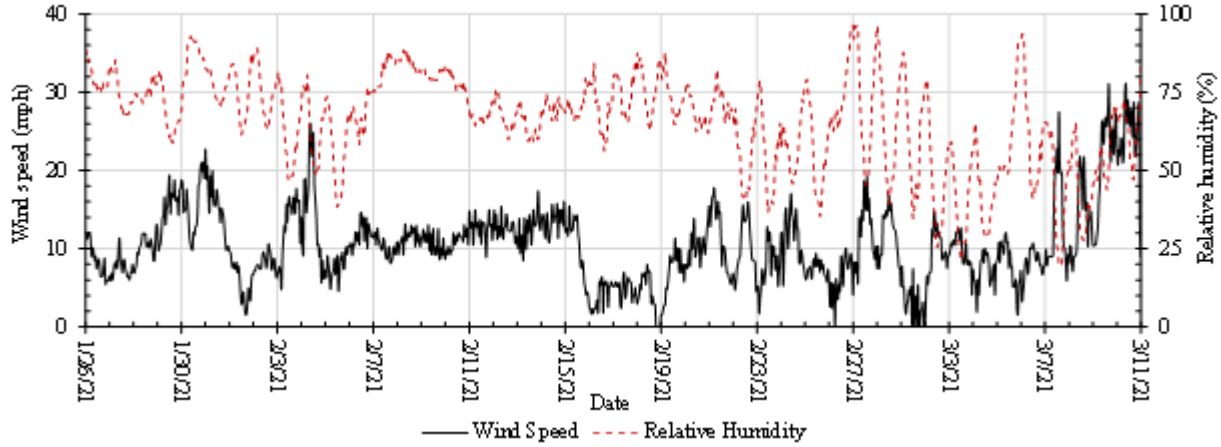

(b) Relative Humidity and Wind Speed

Figure 5.25: Weather Condition from January 26th to March 11th, 2021

Figure 5.26 shows the VWC and temperature readings of the sensor buried under the soil surface. The VWC readings indicated that the VWC readings increased on January 27th and January 31st, 2021, and the increases of the VWC readings were caused by the rainfalls on January 27th and January 30th, 2021. The VWC readings dropped quickly during the period from February 9th to 20th, 2021, and then increased quickly from February 21st to 22nd, 2021. These changes of the VWC readings were caused by the freeze-thaw process of water in the soil, which was evidenced by the below 32 °F (0 °C) temperature readings from February 9th to 25th, 2021. In addition, since water in the soil was frozen, the moisture sensor could not measure the VWCs correctly and the VWC readings did not vary much for the sensor buried under the soil surface.

Figure 5.27 shows the VWC readings in Section I during the period from January 26th to March 10th, 2021. Similarly, to what was explained earlier, Figure 5.27(a) shows that the VWC readings in the subgrade soil from January 26th to February 12th did not change with the rainfall when the air temperature was above 32 °F (0 °C). After that, the VWC readings for Sensor I-1-A and Sensor I-1-D rapidly dropped due to the frozen process of water in the subgrade soil. As mentioned earlier, unfortunately, the datalogger stopped recording data after February 16th, 2021, for the sensors in this section. Figure 5.27(b) shows that VWC readings of the sensors at 6 in. (0.15 m) above the wicking geotextile fluctuated with the rainfall and then decreased with time after the rainfall. The abrupt decrease of the VWC readings of Sensor I-2-G was caused by freezing of water in the aggregate. Figure 5.27(c) shows the slight variations of the VWC readings of the sensors at Level 3 after the rainfall due to water infiltration from January 30th to February 1st, 2021. However, the VWC readings of these sensors except for Sensor I-3-A decreased abruptly due to freezing of water in the aggregate.

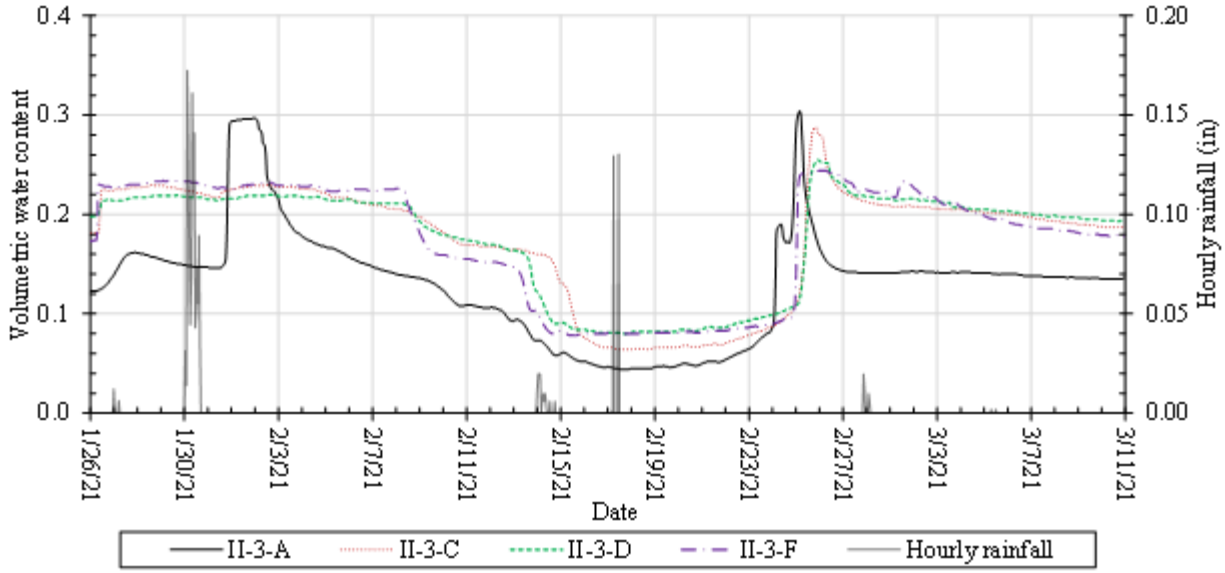

Figure 5.26: VWC and Temperature Readings of the Sensor under the Soil Surface from January 26th to March 11th, 2021

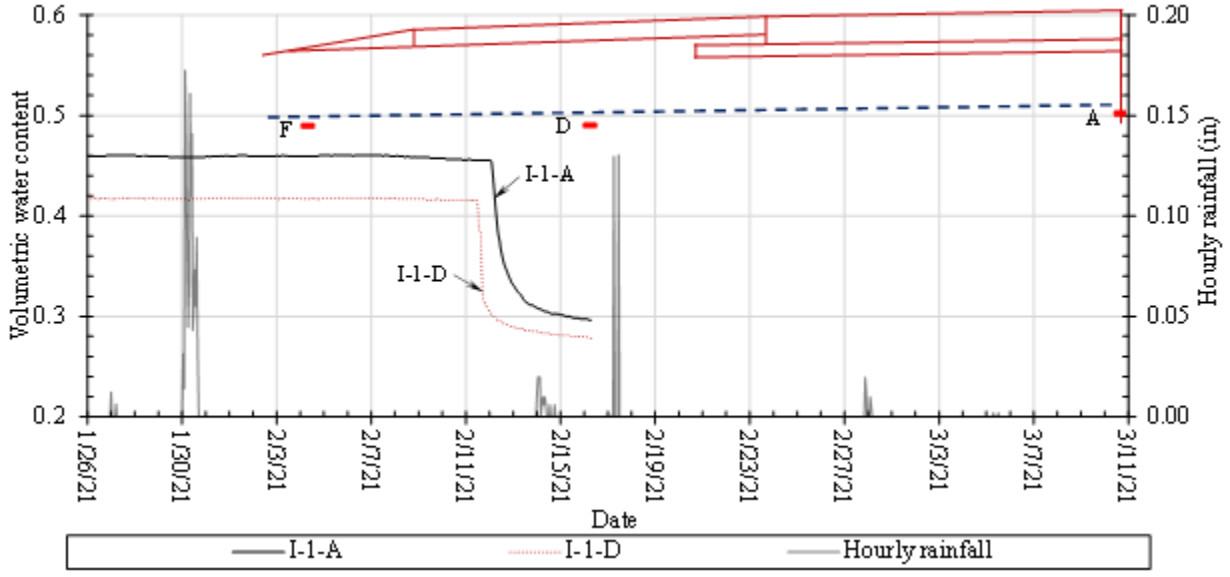

(a) At the Elevation of 6 in. below the Wicking Geotextile

Figure 5.27: VWC Readings in Section I from January 26th to March 10th, 2021

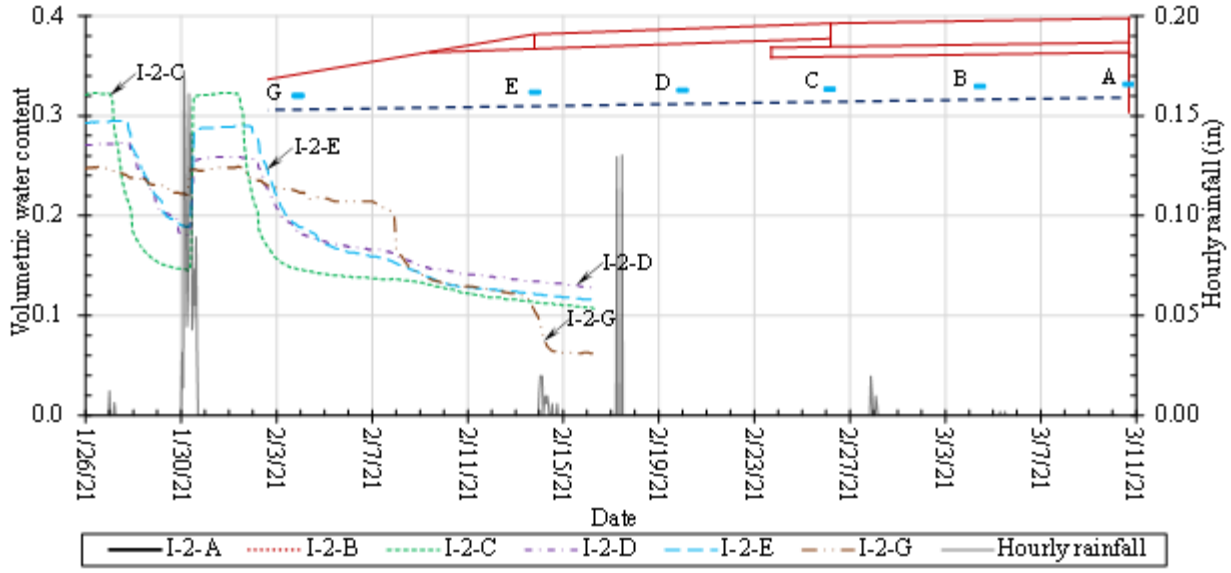

(b) At the Elevation of 6 in. above the Wicking Geotextile

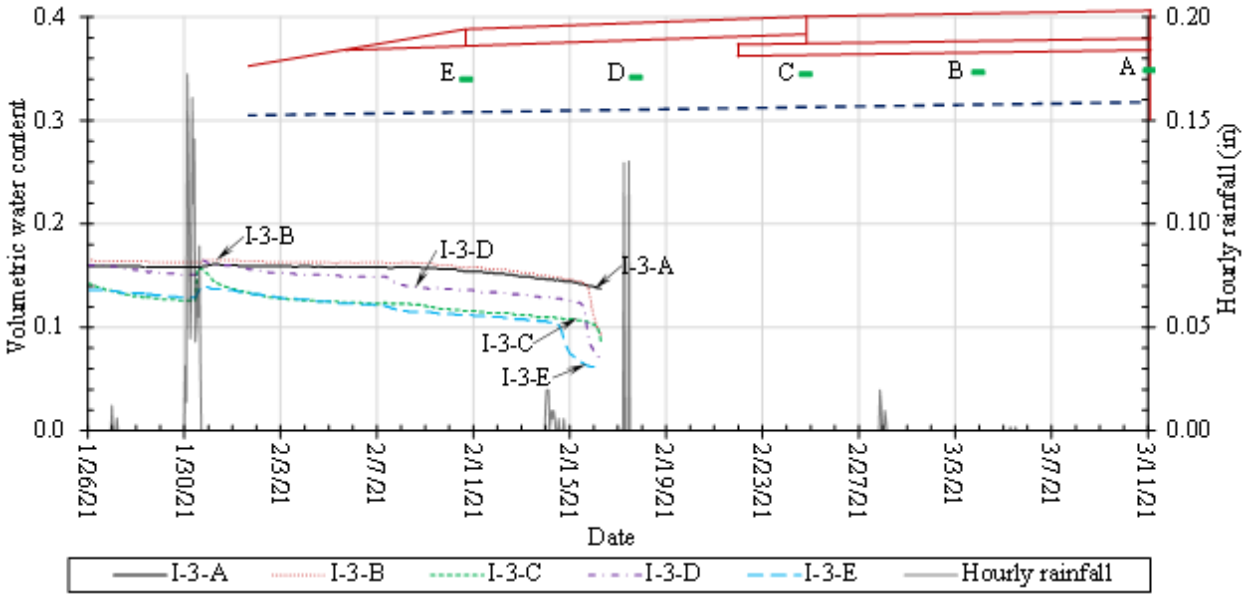

(c) At the Elevation of 12 in. above the Wicking Geotextile

Figure 5.27: VWC Readings in Section I from January 26th to March 10th, 2021 (Continued)

Figure 5.28 shows the VWC readings of the sensors in Section II. During the period from January 26th to February 3rd, 2021, the AB-1 aggregate near Sensor II-3-C, Sensor II-3-D, and Sensor II-3-F were saturated before the rainfall on January 30th, 2021, so that their readings did not change after the rainfall. However, the VWC readings of Sensor II-3-A increased quickly after the precipitation on January 30th, 2021, due to water infiltration through the joint and then

decreased with time due to drainage until February 11th, 2021 (the start of the freezing process). As mentioned previously, the temperature in the pavement started to decrease from Sensor II-3-A to Sensor II-3-F under the cold weather condition. On the other hand, the temperature also started to increase from Sensor II-3-A to Sensor II-3-F so that the AB-1 aggregate near Sensor II-3A started to thaw the frozen water. As a result, the VWC readings of Sensor II-3-A increased earlier than those of other sensors. Figure 5.28 clearly shows that the thaw water saturated the AB-1 aggregate on February 25th, 2021, followed by drainage.

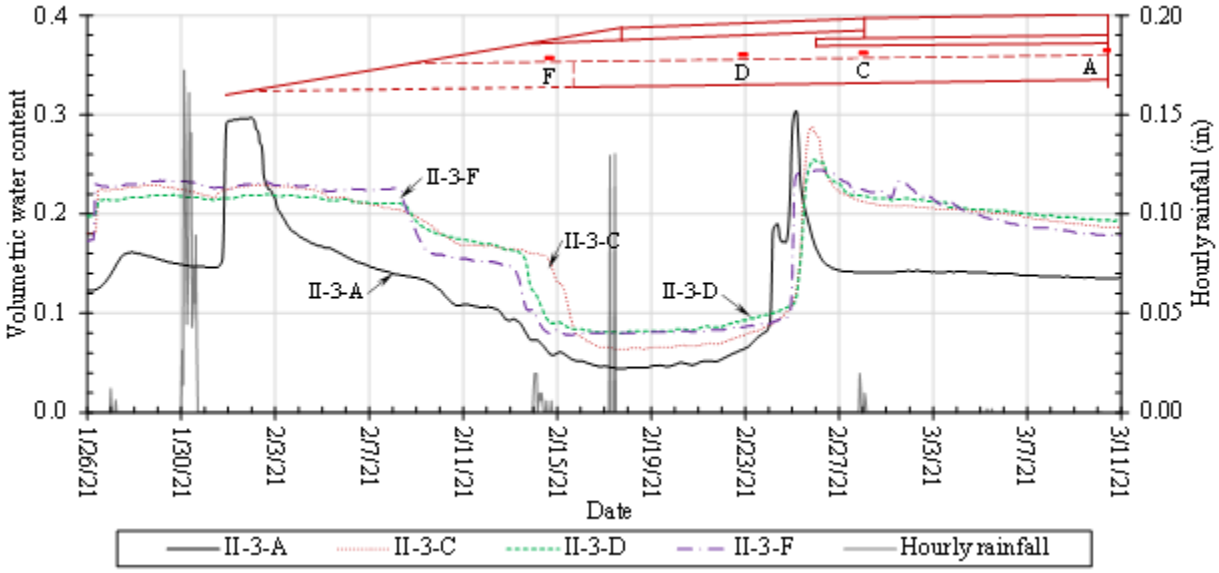

Figure 5.28: VWC Reading Changes in Section II from January 26th to March 11th, 2021

Figure 5.29 shows the changes of the VWC readings of the sensors in Section III during the same time period. Similarly, Figure 5.29(a) shows that the VWC readings in the subgrade soil did not change much with the rainfall, and the low air temperature did not reduce the VWC readings of the sensors too much, likely because the frozen depth did not reach that deep. Figure 5.29(b) shows that the AB-3 aggregate at Level 2 was saturated from January 20th to February 8th, 2021, due to the high groundwater table and the capillary rise. When the wicking geotextile was below the groundwater table, it could not create suction and stop any capillary rise. When the aggregate was saturated, the rainfall did not change the VWC readings. After that, the VWC readings started to decrease due to lowering of the groundwater table. When the groundwater table

was below the wicking geotextile, it could lower the capillary rise and provide wicking drainage. Freezing of water rapidly reduced the VWC readings as shown by Sensor III-2-G. Starting from February 23rd, the temperature was above 32 °F (0 ºC) and the aggregate started to thaw. As a result, the VWC readings quickly increased, and the AB-3 aggregate became saturated again. Starting from March 4th, drainage took place so that the VWC readings decreased with time. Figure 5.29(c) shows the clear variations of the VWC readings of the sensors at Level 3 with the rainfall, freezing, and rainfall again. Since the AB-3 aggregate was not saturated before the rainfall, the VWC readings increased clearly with the rainfall and then decreased with drainage after the rainfall from January 26th to February 15th. When the thaw started, the VWC readings increased again, followed by a decrease due to drainage.

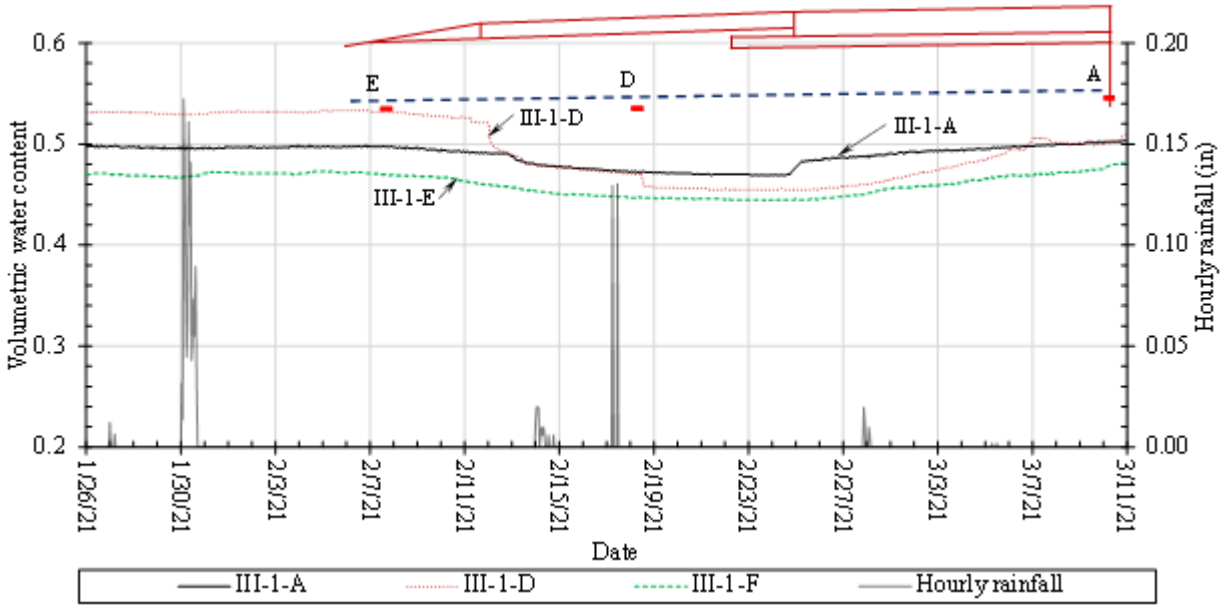

(a) At the Elevation of 6 in. below the Wicking Geotextile

Figure 5.29: VWC Readings in Section III from January 26th to March 11th, 2021

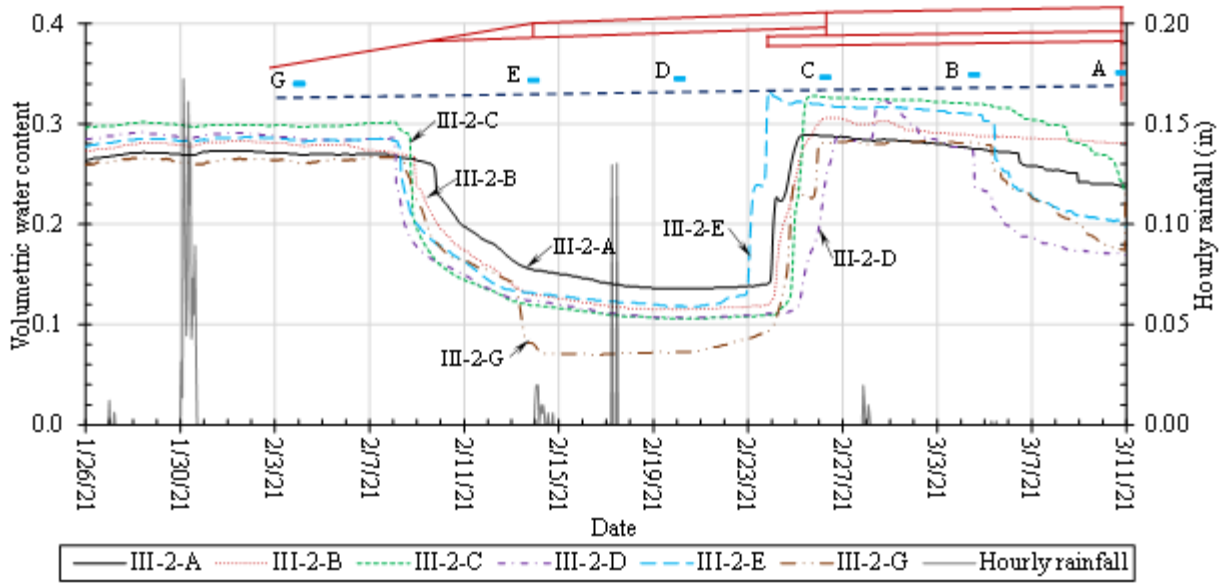

(b) At the Elevation of 6 in. above the Wicking Geotextile

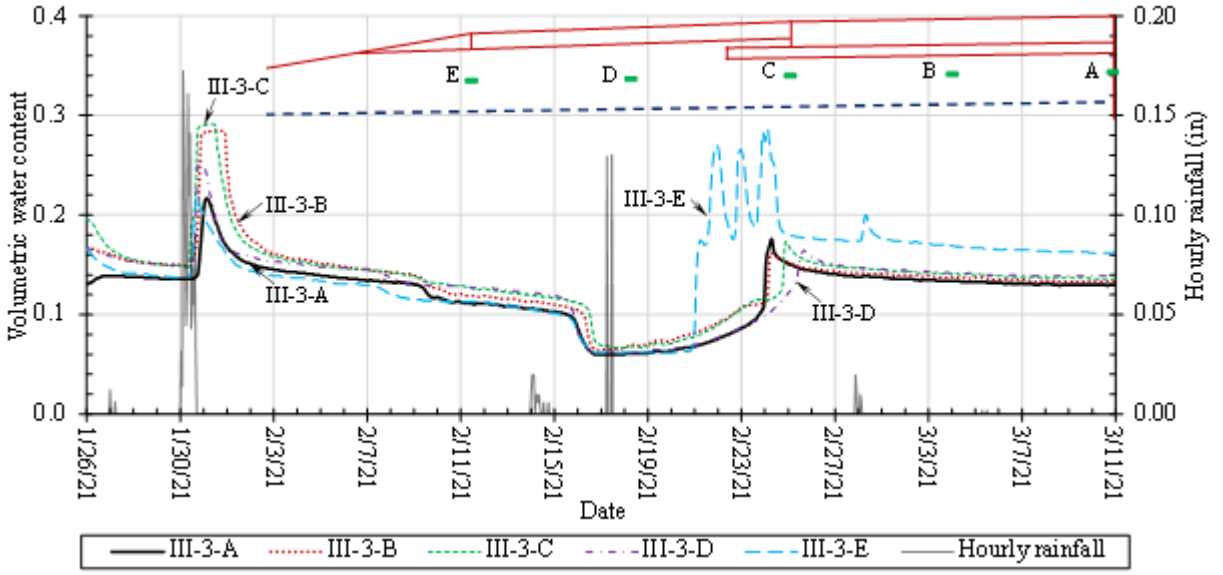

(c) At the Elevation of 12 in. above the Wicking Geotextile

Figure 5.29: VWC Readings in Section III from January 26th to March 11th, 2021 (Continued)

Figure 5.30 shows the comparison of the VWC readings of the sensors at the distances of 0, 12, and 17 ft (0, 3.6, and 5.1 m) away from the centerline of the road at the same top level in the three sections. Among the three sections, Sensor III-3-C, Sensor II-1-A, Sensor III-3-D, and Sensor III-3-A were more sensitive to the first rainfall (on January 30th) but Sensor II-3-A, Sensor II-3-C, Sensor II-3-D, and then Sensor III-3-A and Sensor III-3-C were more sensitive to the thaw (after

February 24th). After these VWC increases, the VWC readings of these sensors decreased with time after the rainfall or the thaw. The reason for Sensor II-3-C and Sensor II-3-D not responding to the first rainfall is that the aggregate at these locations was saturated. The high VWC readings in Section II and Section III from January 30th to February 3rd were likely caused by the high groundwater table and the capillary rise after the rainfall. In addition, from February 24th to 26th, thaw of ice saturated the aggregate in Section II but increased the VWCs in the aggregate in Section III without saturation. Unfortunately, no data was available for Section I. This comparison demonstrated that the wicking geotextile minimized the capillary rise even though the AB-3 aggregate had more fines and small particles than the AB-1 aggregate. This result may also indicate that the cement treated subgrade in Section II was not so effective as the wicking geotextile to minimize the capillary rise. It is equally important that Figure 5.30 clearly shows that during the drying period, Section I and Section III had much lower VWC readings than Section II, indicating that the wicking geotextile worked better than the non-woven geotextile to remove water from the aggregate under unsaturated conditions.

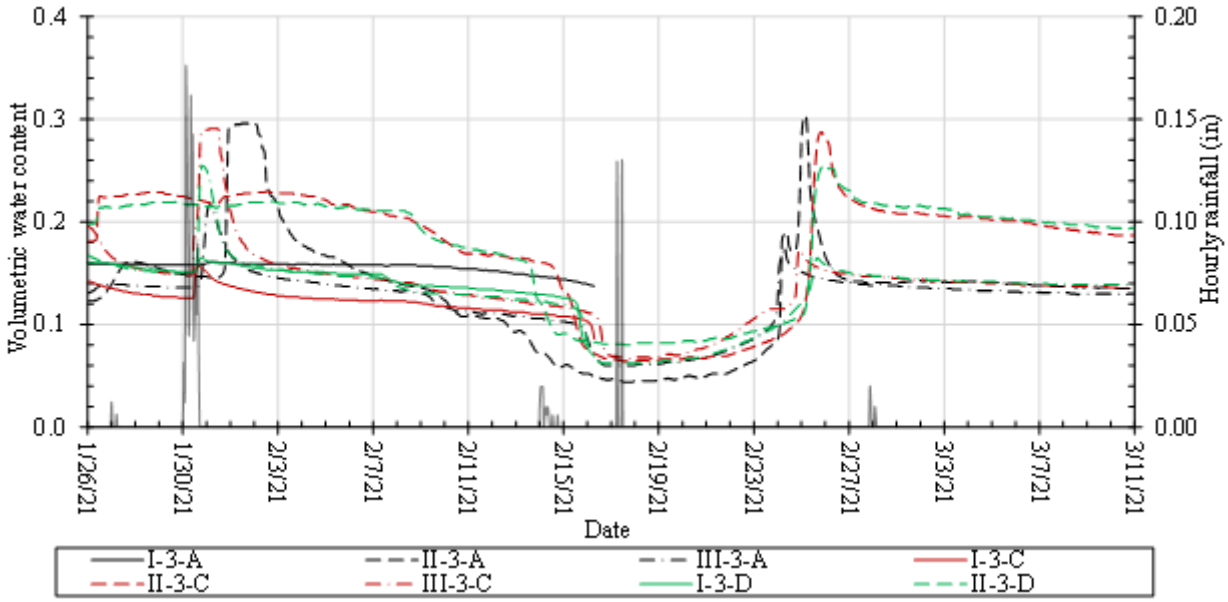

Figure 5.30: Comparison of the VWC Readings in the Three Sections from January 26th to March 11th, 2021

5.4.3 Long-term Performance of Wicking Geotextile

Figure 5.31 shows the VWC readings of the two sensors buried under the soil surface for references. Both sensors show good repeatability of readings until one sensor stopped working in October 2019. The VWC readings of the sensors under the soil surface were very sensitive to the rainfall and drying cycles because they were near the surface.

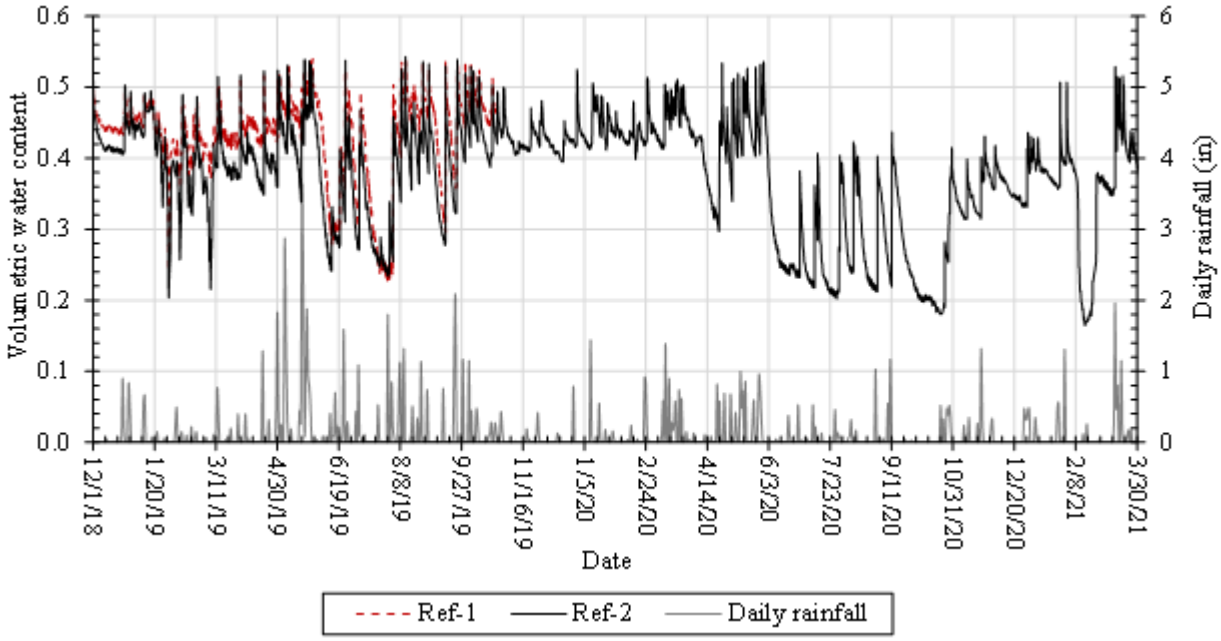

Figure 5.31: VWC Readings of the Sensors under the Soil Surface from December 2018 to March 2021

Figure 5.32 shows the changes of the VWC readings of the sensors in Section I from December 2018 to March 2021. The gaps without any data mean the datalogger stopped recording data. Figure 5.32(a) clearly shows the high VWC values in the subgrade soil and their overall variations throughout the years. The relative VWC values among these sensors seem related to their initial stable values after installation, indicating the density of the soil around each sensor might not be the same after installation. The VWC readings of these three sensors in the subgrade soil were higher from March to October 2019 than those from October 2019 to February 2020. This phenomenon resulted from the heavy rainfalls from March to October 2019.

Figure 5.32(b) shows the changes of the VWC readings of the sensors at Level 2 (i.e., 6 in. or 0.15 m above the wicking geotextile) in the AB-1 aggregate in Section I. All the sensors except

for Sensor I-2-A were sensitive to the rainfalls. After reaching the peak VWC readings (saturation) due to the rainfalls, the VWC readings decreased quickly due to the gravitational drainage and the wicking drainage of the wicking geotextile down to approximately 13% to 17%. Since Sensor I- 2- A was at the highest elevation among these sensors, the groundwater rise had difficulty reaching this level and the water infiltration from the surface took more time to reach this level, also. Among all the sensors at this elevation, the VWC readings of Sensor I-2-C varied most significantly with the rainfalls. This might be induced by the combined effect of the groundwater rise and the water infiltration at the joint between the shoulder pavement and the lane pavement. However, the VWC readings dropped quickly to the lowest VWC readings (approximately 13%) due to the gravitational drainage and the wicking drainage after the rainfalls.

Figure 5.32(c) shows the VWC readings of the sensors at Level 3 in Section I. After January 12th, 2019, the VWC readings of Sensor I-3-A and Sensor I-3-B did not change significantly with the rainfalls because the groundwater could not reach this elevation. As mentioned previously, limited water could infiltrate through the joint between the left lane and the right lane to affect the VWC readings of Sensor I-3-A. It was even more difficult for water to infiltrate to this location of Sensor I-3-B because it was under the middle of the lane pavement. The VWC readings of Sensor I-3-D fluctuated less significantly than Sensor I-3-E and Sensor I-3-C with the rainfalls. Water infiltration through the joint between the lane and the shoulder increased the VWC readings of Sensor I-3-C, while water easily infiltrated through the rock stone to reach Sensor I-3-E. However, Sensor I-3-D was located under the middle of the shoulder pavement; therefore, water had more difficulty reaching it there.

Figure 5.32(d) shows the profiles of the VWC readings of the top and middle level sensors in the AB-1 aggregate at different distances from the center of the road on the selected heavy rainfall (RF) day (May 21st, 2019) and on the selected non-rainfall (drying) day (NR) (July 18th, 2019). The profiles did not show a clear trend in terms of the VWC distribution with the distance. However, the middle level sensors indicated that the aggregate was saturated or nearly saturated on the RF day, while the aggregate was not saturated at the top level. From the RF day to the NR day, the VWC values for the middle level decreased from approximately 28% to 14% due to lowering of the groundwater table, gravitational drainage, and wicking drainage by the wicking

geotextile. However, the VWC values for the top level decreased from approximately 14% to 13% due to wicking drainage by the wicking geotextile. Since the aggregate at the top level was farther from the wicking geotextile than that at the middle level, the wicking effect decreased as shown by Guo et al. (2019b) in their laboratory study. These results indicate that the effective distance for the wicking geotextile in the AB-1 aggregate was 12 in. (0.3 m) or greater, which is slightly greater that found by Guo et al. (2019b).

Figure 5.32(e) shows the VWC readings of the top and middle level sensors in the AB-1 aggregate at different distances from the transverse joint. For easy evaluation, the profiles of the VWC values along the distance to the transverse joint on the same selected days as discussed above are plotted in Figure 5.32(f). The middle level sensors indicated that the aggregate was saturated or nearly saturated on the RF day; however, the top level sensors showed that the aggregate was not saturated. On the NR day, the aggregate had much lower VWC values for the middle level, indicating lowering of the groundwater table and effective drainage. The VWC values at the middle level decreased from approximately 29% to 16% from the RF day to the NR day, which is significant. At the top level, the VWC values decreased from approximately 22% to 14% from the RF day to the NR day, indicating effective drainage by the wicking geotextile. The large VWC reduction might include gravitational and wicking drainage. These results also indicate that the effective distance for the wicking geotextile in the AB-1 aggregate was 12 in. (0.3 m) or greater.

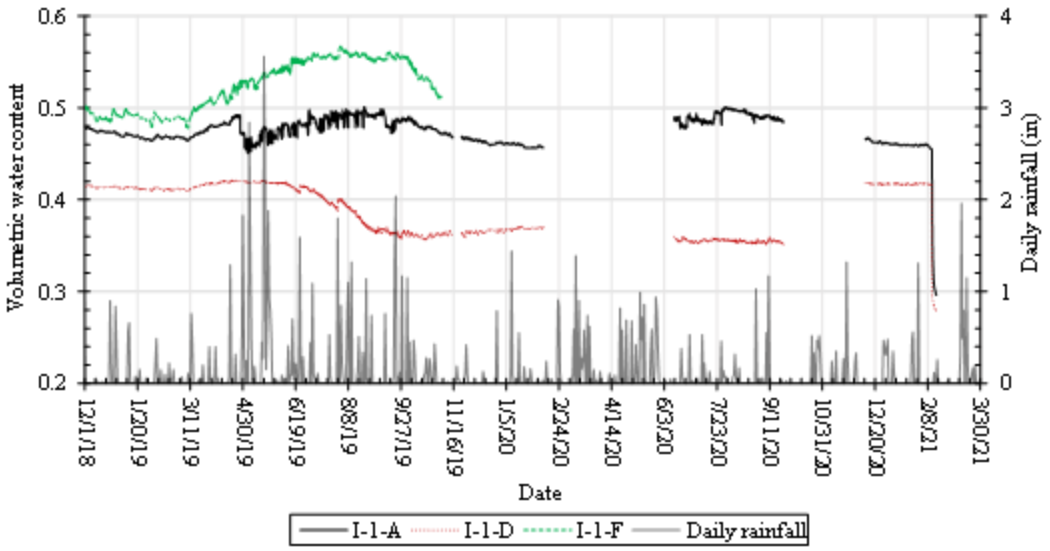

(a) At the Elevation of 6 in. below the Wicking Geotextile

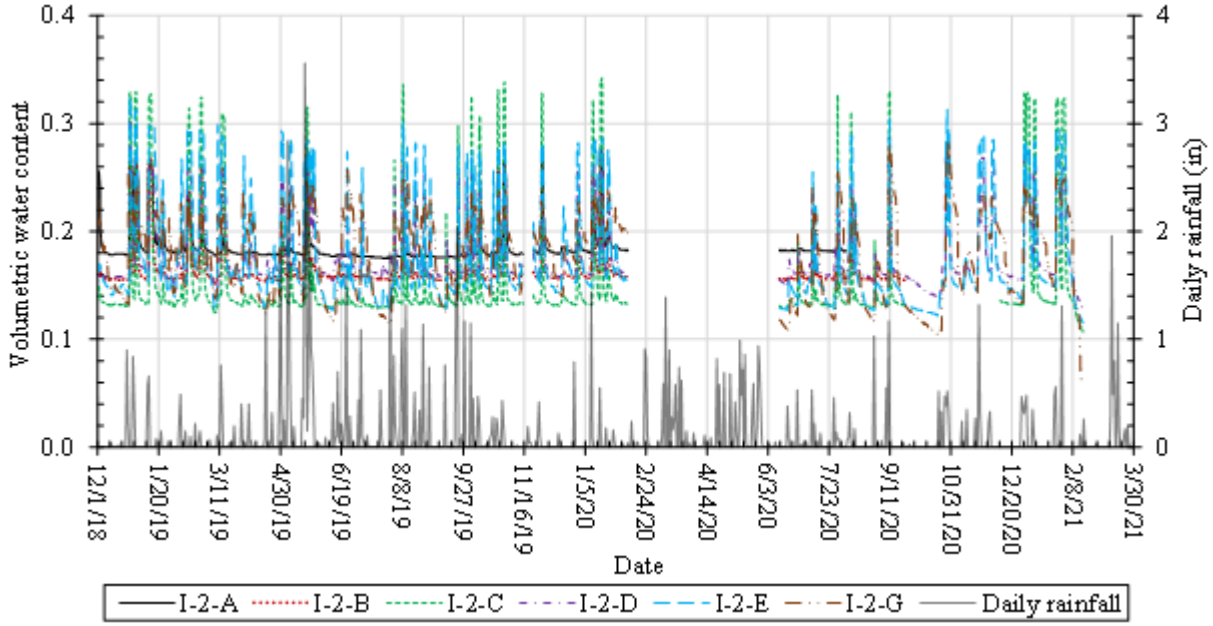

(b) At the Elevation of 6 in. above the Wicking Geotextile

Figure 5.32: VWC Readings of Sensors in Section I from December 2018 to March 2021

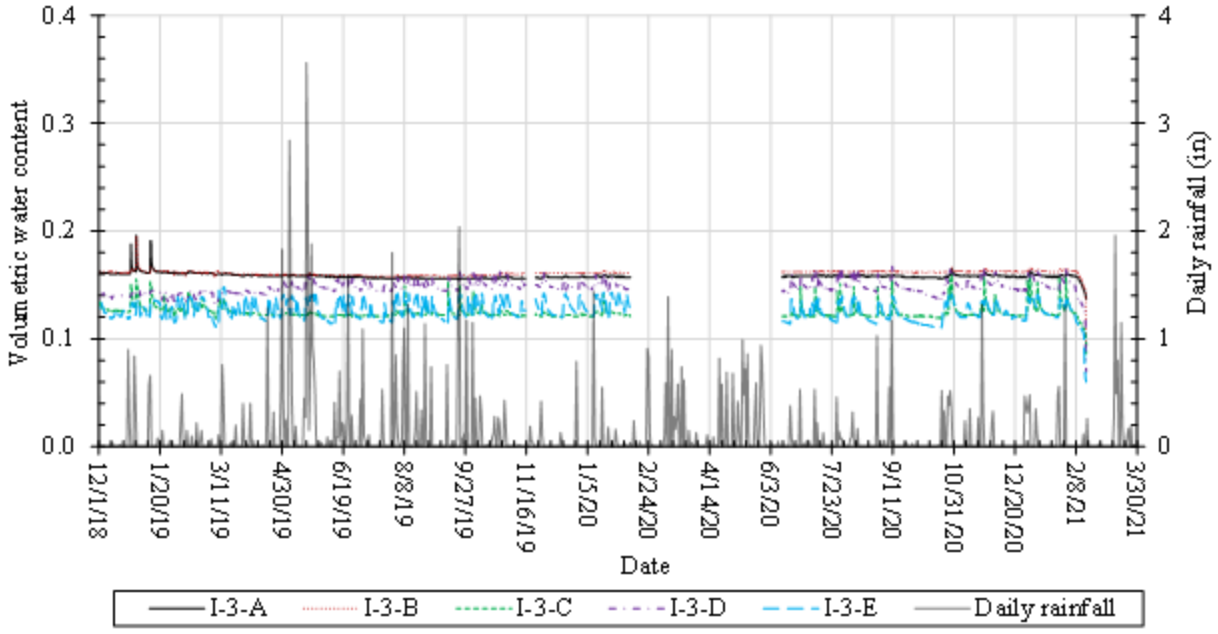

(c) At the Elevation of 12 in. above the Wicking Geotextile

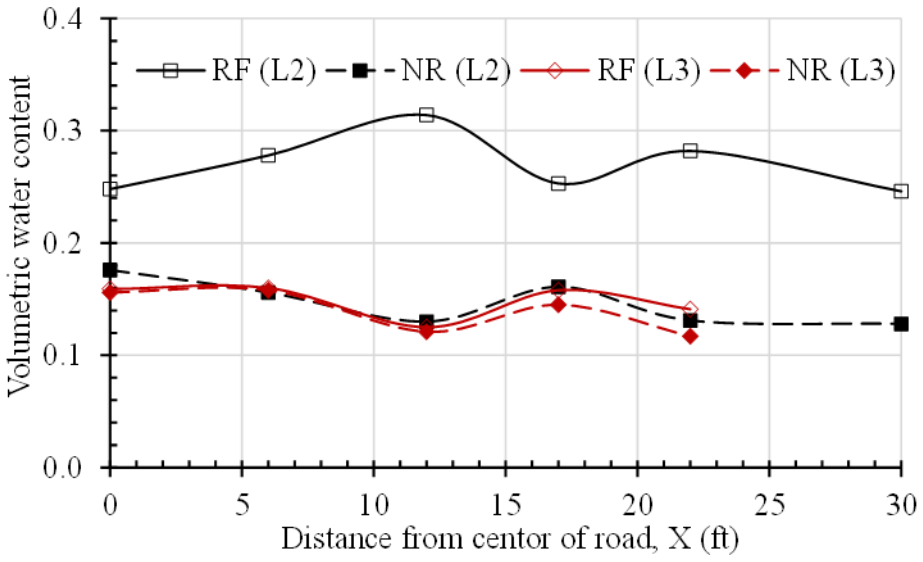

(d) VWC Profile from the center of the Road

Figure 5.32: VWC Readings of Sensors in Section I from December 2018 to March 2021 (Continued)

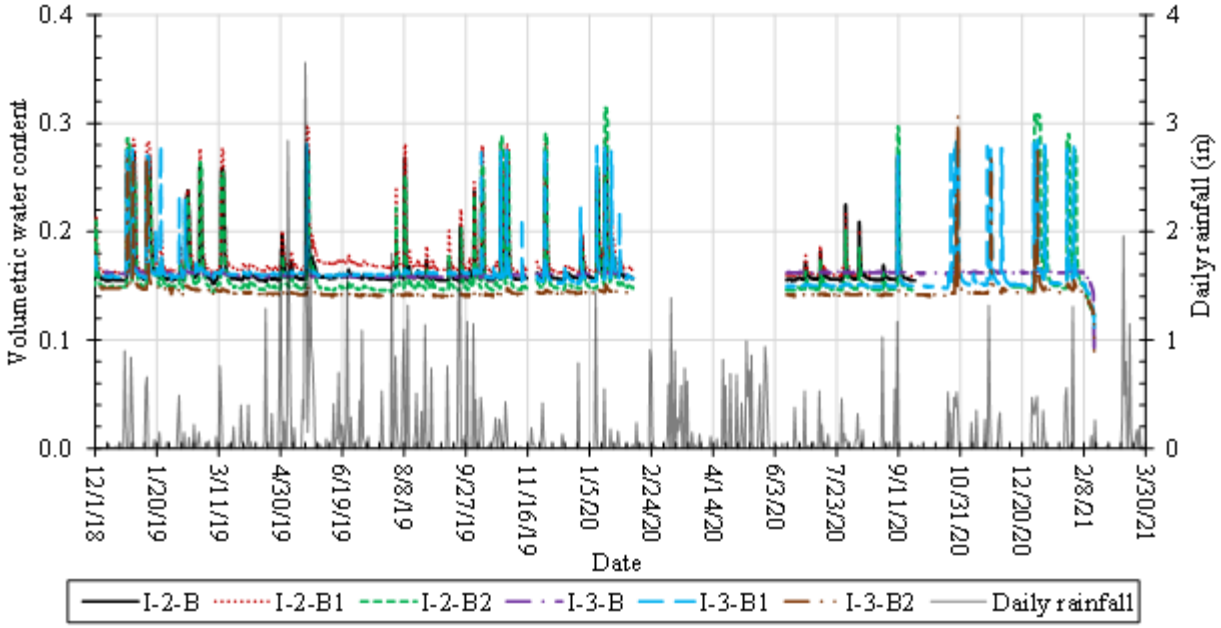

(e) At Different Distances from the Transverse Joint

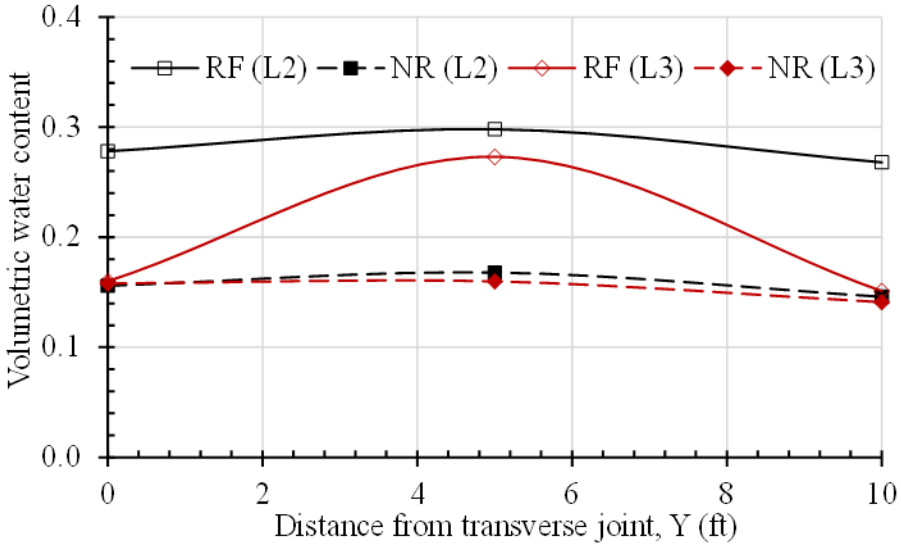

(f) VWC Profile from the Transverse Joint

Figure 5.32: VWC Readings of Sensors in Section I from December 2018 to March 2021 (Continued)

Figure 5.33(a) shows the VWC readings of the sensors in Section II during the same time period as discussed for Section I. The VWC readings of Sensor II-3-A were less sensitive to the rainfalls during the period from March to October 2019 than the period from October 2019 to March 2020 and October 2020 to March 2021 even though the rainfalls were heavy and occurred more frequently from March to October 2019. There are three possible reasons: higher air

temperatures during March to October accelerated water evaporation; thaw after water freeze significantly increased VWC as discussed earlier; or unfrozen aggregate could drain but frozen aggregate could not drain. From late fall (October) to early spring (March), more water accumulated in the aggregate base and the VWC readings were more sensitive to rainfalls and temperature changes and reached saturation. Continuous rainfalls from Apr 22nd, 2020, to May 16th, 2020, also increased the VWC readings of Sensor II-3-A significantly to saturation due to the water table rise, the capillary rise, and the water infiltration. Except for the VWC readings for Sensor II-3-A, most sensors had the low VWC readings ranging from 14% to 18%, which were higher than those (14% to 16%) at the same elevation in Section I. This difference demonstrates the benefit of the wicking geotextile to keep the VWC values lower for the AB-1 aggregate.

Figure 5.33(b) shows the profiles of the VWC readings of the top sensors in the AB-1 aggregate at different distances from the center of the road on the selected heavy rainfall (RF) day (May 21st, 2019) and on the selected non-rainfall day (NR) (July 18th, 2019). The profiles show a general trend that the VWC values increased with the distance from the center of the road. The VWC values in Section II on the RF day were higher than those in Section I with the same AB-1 aggregate at the same elevation. The reduction of the VWC values from the RF day to the NR day in this section was slightly larger than that in Section I. However, the average VWC value (16%) on the NR day in this section was higher than that (14%) in Section I, demonstrating the benefit of the wicking geotextile to further remove water from the aggregate.

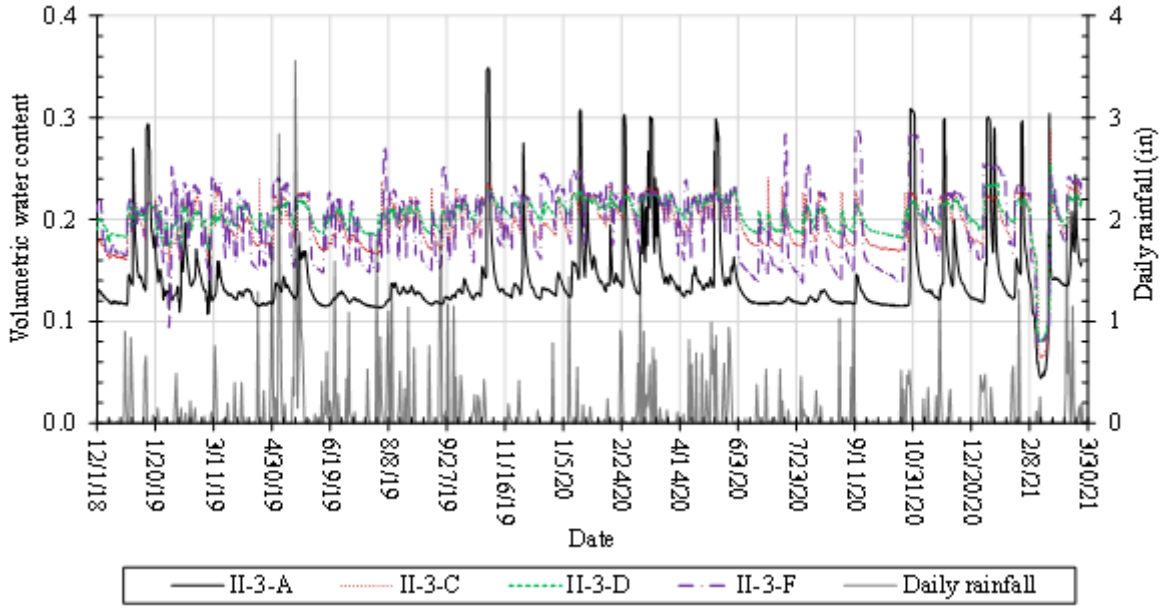

(a) Sensor at the Top Level

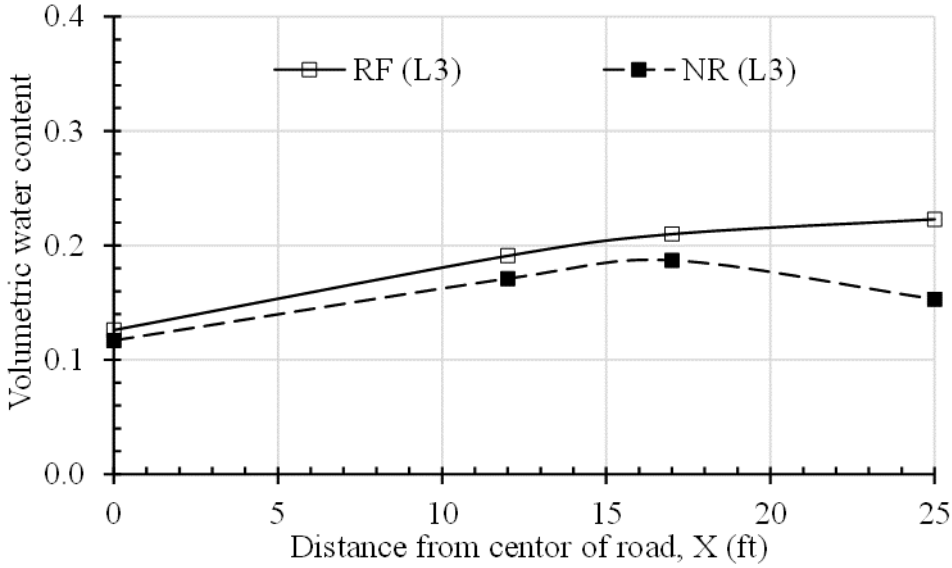

(b) VWC Profile from the center of the Road

Figure 5.33: VWC Readings of Sensors in Section II from December 2018 to March 2021

Figure 5.34 shows the VWC readings of the sensors in Section III during the same period for Section I and Section II. Similarly, the VWC readings of the sensors in the first level (subgrade) were higher from March to October 2019 than those from October 2019 to March 2020. There was another time period from March to October 2020 with higher VWC readings. Figure 5.34(b) shows the VWC readings of the sensors in the second level in Section III fluctuated less significantly

with the rainfalls as compared with those in Section I. The figure clearly shows that the aggregate at the level was saturated after rainfalls. In other words, the wicking geotextile was below the groundwater table during saturation so that it could not stop capillary rise and provide wicking drainage. Since the AB-3 aggregate in Section III had more fines and small particles than the AB-1 aggregate in Section I, gravitational drainage in Section III was slower than that in Section I; therefore, the AB-3 aggregate in Section III maintained high VWCs longer than the AB-1 aggregate in Section I. Figure 5.34(c) shows that the VWC readings of the sensors at the third level varied with the rainfalls or thawing. However, the maximum and minimum VWC values in the AB-3 aggregate at this level in Section III were lower than those in the AB-1 aggregate at the same level in Section I and Section II. The AB-3 aggregate with lower VWC values is beneficial for maintaining higher resilient modulus and pavement performance. Figure 5.34(d) shows the VWC readings of the sensors in the AB-3 aggregate at the second and third levels at different distances from the transverse joint. The curves clearly show that the VWC readings of the sensors at the second (lower) level were higher than those at the third (higher) level. The sensors away from the transverse joint generally measured lower VWC readings.

Figure 5.34(d) shows the profiles of the VWC readings of the top and middle level sensors in the AB-3 aggregate at different distances from the center of the road on the selected heavy rainfall (RF) day (May 21st, 2019) and on the selected non-rainfall day (NR) (July 18th, 2019). On the RF day, the profiles show the increase of the VWC values with the distance, (i.e., those close to the ditch had higher VWC values). The middle level sensors indicated that the aggregate was saturated or nearly saturated on the RF day; however, the top level sensors showed that the aggregate was not saturated except for the two sensors close to the ditch. From the RF day to the NR day, the VWC values for the middle level decreased from approximately 28% to 16% due to lowering of the groundwater table, gravitational drainage, and wicking drainage by the wicking geotextile. However, the VWC values for the top level decreased from approximately 18% to 12% due to wicking drainage by the wicking geotextile. Since the aggregate at the top level was farther from the wicking geotextile than that at the middle level, the wicking effect decreased as shown by Guo et al. (2019b) in their laboratory study. However, the VWC reduction in the AB-3

aggregate was more than that in the AB-1 aggregate by the wicking geotextile. In addition, this result indicates that the effective distance of the wicking geotextile was 12 in. (0.3 m) or greater.

Figure 5.34(e) shows the VWC readings of the top and middle level sensors in the AB-3 aggregate at different distances from the transverse joint. For easy evaluation, the profiles of the VWC values along the distance to the transverse joint on the heavy rainfall (RF) day (May 21st, 2019) and on the non-rainfall day (NR) (July 18th, 2019) are plotted in Figure 5.34(f). The middle level sensors indicated that the aggregate was saturated or nearly saturated on the RF day; however, the top level sensors showed that the aggregate was not saturated on the RF day. On the NR day, the aggregate had much lower VWC values for the middle level, indicating lowering of the groundwater table, gravitational drainage, and wicking drainage by the wicking geotextile. The VWC values at the middle level decreased from approximately 28% to 15% from the RF day to the NR day, which is significant. At the top level, the VWC values decreased from approximately 14% to 11% from the RF day to the NR day, which is lower than those (14%) in Section I and (16%) in Section III, indicating effective drainage by the wicking geotextile in the AB-3 aggregate.

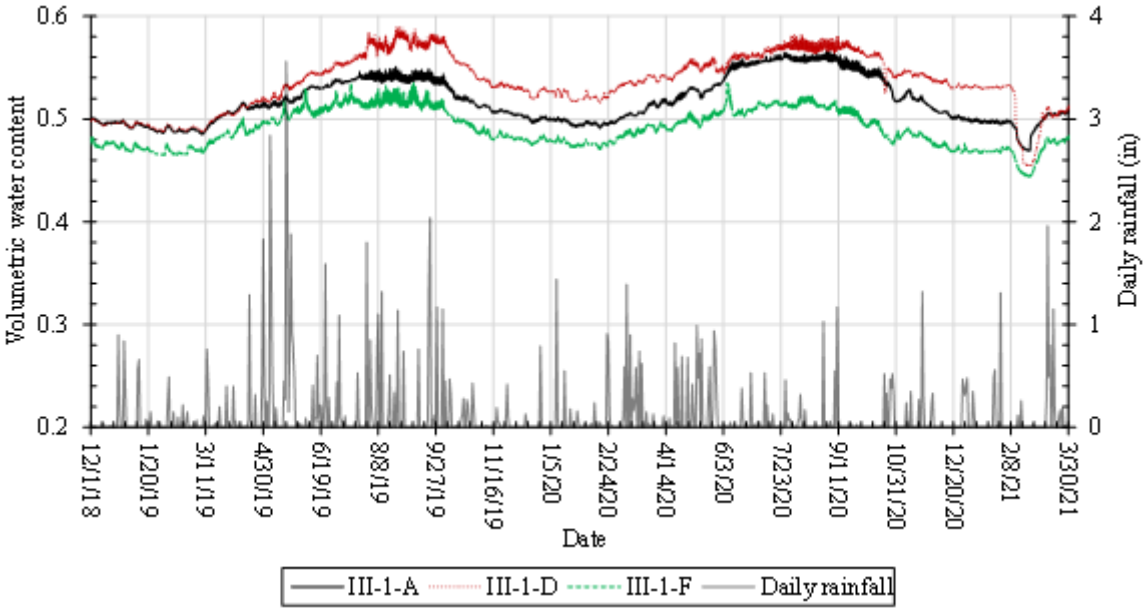

(a) At the Elevation of 6 in. below the Wicking Geotextile

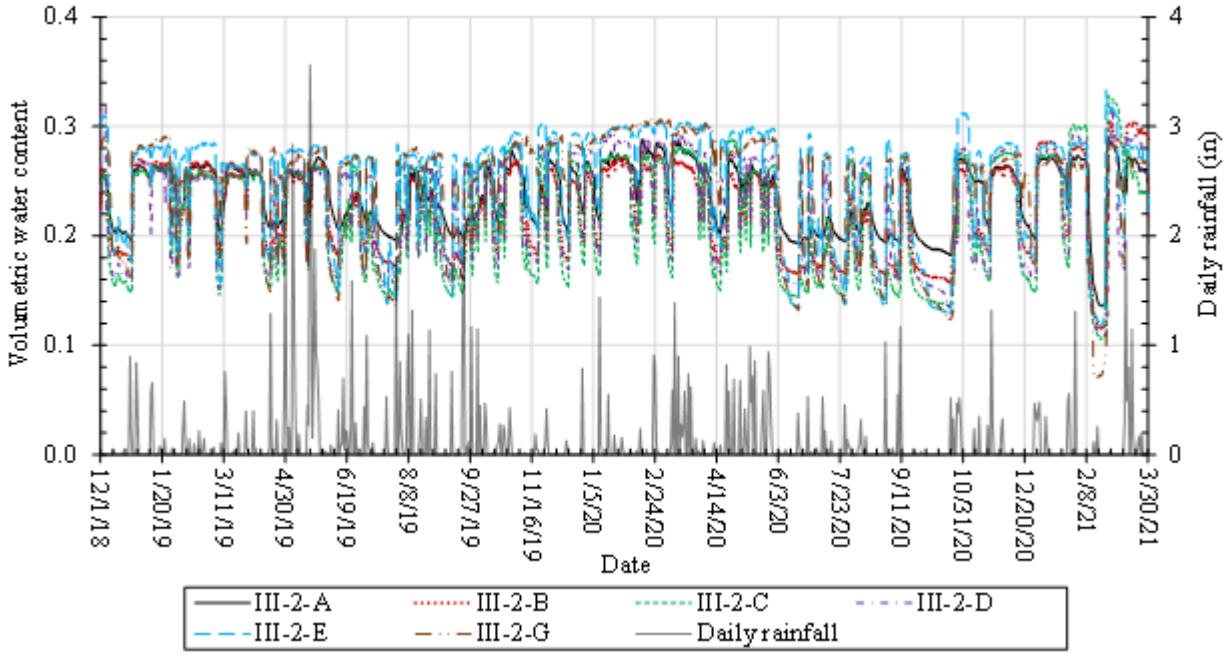

(b) At the Elevation of 6 in. above the Wicking Geotextile

Figure 5.34: VWC Readings of Sensors in Section III from December 2018 to March 2021

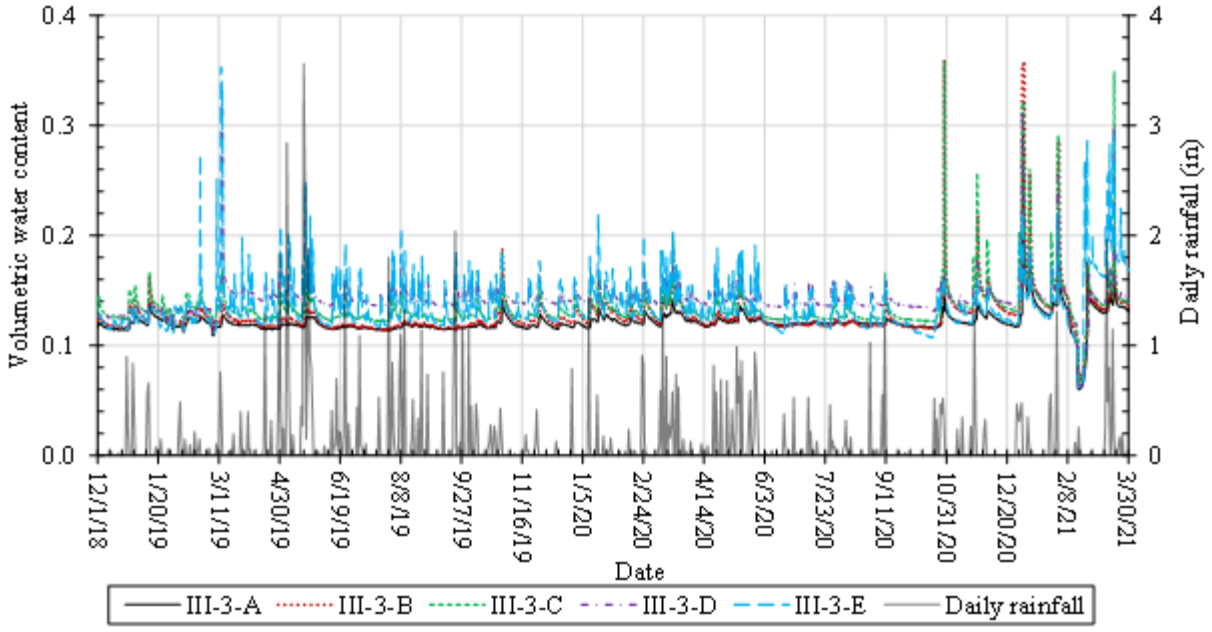

(c) At the Elevation of 12 in. above the Wicking Geotextile

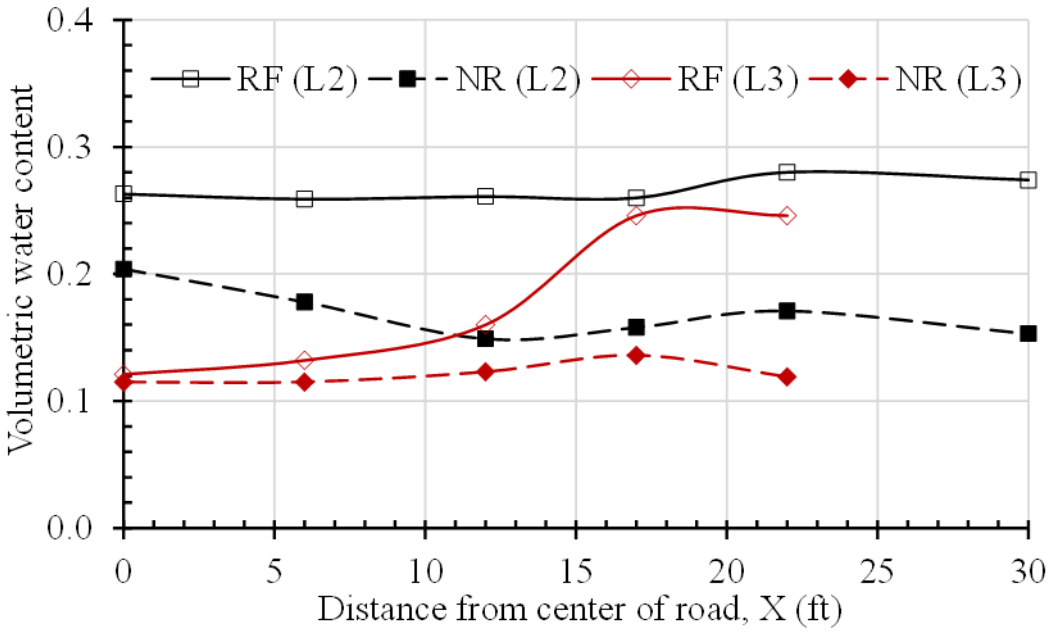

(d) VWC Profile from the center of the Road

Figure 5.34: VWC Readings of Sensors in Section III from December 2018 to March 2021 (Continued)

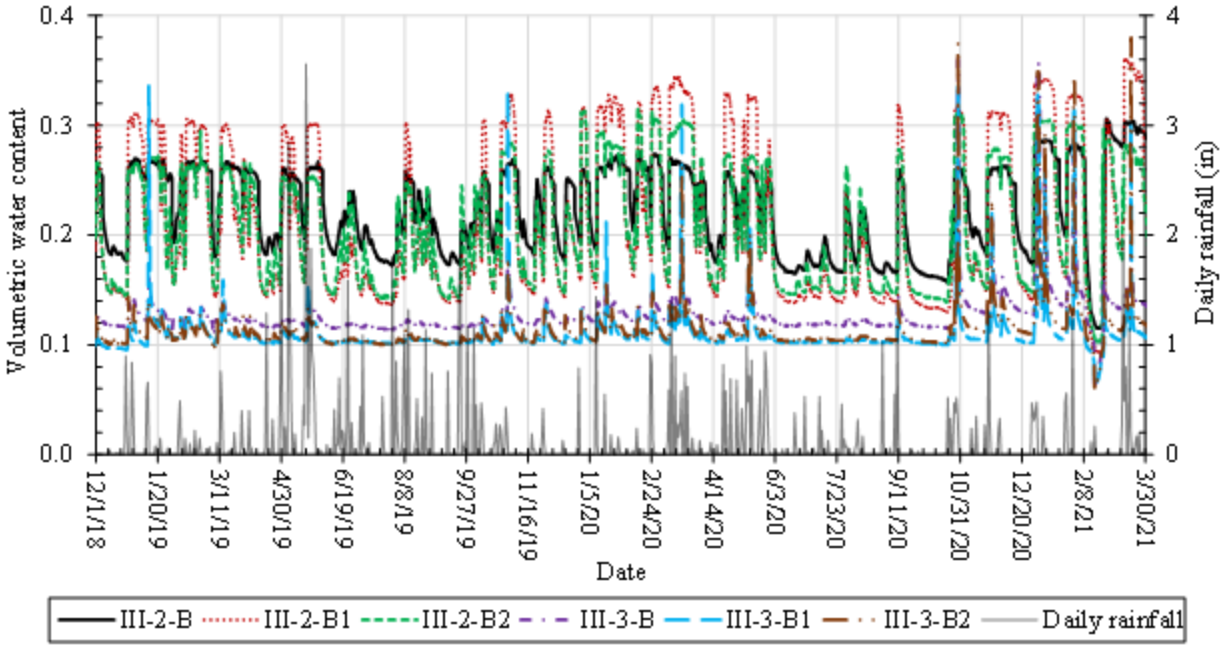

(e) At Different Distances from the Transverse Joint

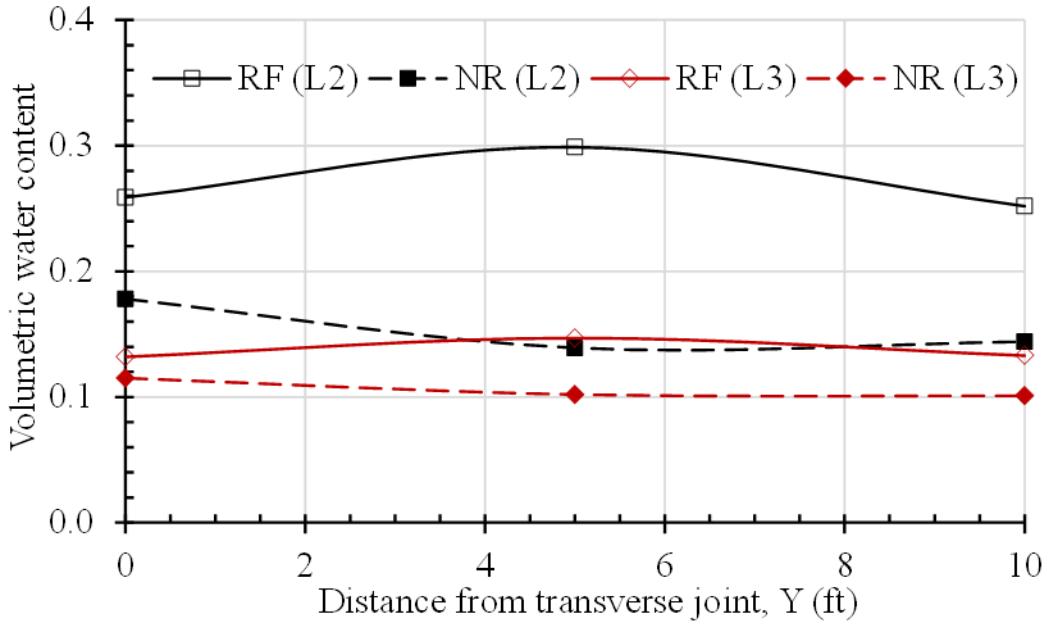

(f) VWC Profile from the Transverse Joint

Figure 5.34: VWC Readings of Sensors in Section III from December 2018 to March 2021 (Continued)

Chapter 6: Conclusions and Recommendations

Water in pavements is the main factor contributing to deterioration and distresses of pavements. Water can come into a pavement section from different sources: infiltration, groundwater rise, capillary rise, freeze and thaw, and vapor movement. Water loss can happen due to evaporation, drainage, and lowering of groundwater table. In addition to the measures to remove water on pavements by slope runoff and prevent water from entering the pavement by barriers, granular material and geocomposites are utilized to remove water from the pavement. However, these drainage materials are effective under saturated or nearly saturated conditions but not effective under unsaturated conditions. Even under unsaturated conditions, excessive water in the pavement may still cause pavement distresses due to lower modulus and freeze-thaw. Recent laboratory and field studies showed that the wicking geotextile available in the market could minimize capillary rise of water and continue removing water from the pavement under unsaturated conditions, thus improving pavement performance. Most of these past studies focused on the use of the wicking geotextile for unpaved and asphalt paved roads. Limited studies have been done for the use of the wicking geotextile in concrete pavements. In this study, the wicking geotextile was adopted for a field trial in the reconstruction of concrete pavements in an area with higher groundwater tables. To evaluate the effectiveness of the wicking geotextile, moisture sensors were installed in the subgrade and two different types of aggregate bases at three levels in three test sections (Section I and Section III with the wicking geotextile and Section II as a control section with a non-woven geotextile). These sensors were monitored for the variations of volumetric water contents (VWC) in the subgrade soil and the aggregate base for over two and half a year. Rainfalls, snowfalls, and freeze-thaw cycles happened during this period, which affected the level of groundwater table and the VWC readings.

6.1 Conclusions

The monitored temperature and VWC data were reduced, analyzed and lead to the following conclusions:

1. The temperature in the concrete pavements changed seasonally with the air temperature. Under the hot air temperature condition, the temperature right

below the pavement surface could be higher than the air temperature, but the temperature decreased as the depth from the pavement surface increased. Under the cold temperature condition, heat transferred upward from the subgrade soil, thus resulting in the increase of the temperature as the depth increased.

2. In general, the variations of the measured VWCs in the subgrade and the aggregate can be divided into two periods: from late March to late October (Period 1) and from early November to early March (Period 2). During Period 1, the VWC readings were mainly affected by rainfalls (water infiltration, groundwater table rise, and capillary rise), while during Period 2, the VWC readings were mainly affected by freeze-thaw.
3. The VWC readings of the sensors in the subgrade in all three sections varied with the season, but slightly with individual rainfalls. The higher VWC readings were measured during Period 1, while the lower VWC readings were measured during Period 2. During the two and a half years monitoring period, the subgrade was saturated or nearly saturated at most times.
4. Different from the VWC readings for the subgrade, the VWC readings for the aggregate bases (including the AB-1 aggregate and the AB-3 aggregate) generally varied with heavy rainfalls or continuous light rainfalls. When the aggregate became saturated, its readings did not vary with rainfalls. They also changed with the seasonal temperatures, especially when the temperature dropped below the freezing temperature. Furthermore, the VWC readings increased quickly when the aggregate started to thaw. During the thawing period, the aggregate in the middle level (i.e., 12 in. or 0.3 m above the subgrade) could be saturated.
5. The concrete pavement minimized water infiltration into the aggregate base after rainfall. Longitudinal and transverse joints performed well and only allowed some water infiltration during continuous rainfalls. The rock stone surface provided easier paths for water infiltration than the lane pavement and the shoulder pavement.

6. The AB-3 aggregate contained more small particles than the AB-1 aggregate; therefore, it slowed down the water infiltration but kept moisture for a longer duration than the AB-1 aggregate due to slower gravitational drainage.
7. When the groundwater table rose above the wicking geotextile after rainfalls, the wicking geotextile could not perform the wicking function until an unsaturated condition resumed. When the groundwater table was below the wicking geotextile, the wicking geotextile could minimize the capillary rise. After the gravitational drainage of the aggregate completed, the wicking geotextile could continue removing water from the aggregate base. The gravitational drainage reduced the VWC values more significantly and faster than the wicking drainage, but the wicking geotextile provided additional benefit in lowering the VWC values. The effective wicking distance of the wicking geotextile in the AB-1 aggregate and the AB-3 aggregate was 12 in. (0.3 m) or greater.
8. The wicking geotextile was more effective to minimize the capillary rise than the cement treated subgrade when the groundwater table was below the wicking geotextile.
9. During the dry period, the VWC readings in the aggregate with the wicking geotextile were generally lower than those with the non-woven geotextile, demonstrating the benefit of the wicking geotextile continuously removing water from the aggregate base. In addition, the VWC readings in the aggregate base under the concrete pavement with the wicking geotextile were more sensitive to rainfalls than those in the section with the non-woven geotextile because the aggregates with the wicking geotextile were drier than those with the non-woven geotextile.
10. Over years, deteriation of sealing joints and cracking in the pavement will allow more water infiltration into the base course. The benefit of the wicking geotextile to reduce water contents in the base course is expected to be more significant but needs to be verified in the future.

6.2 Recommendations

The following recommendations can be made from this study for the application of the wicking geotextile in future projects:

1. The wicking geotextile should be placed above the predicted highest groundwater table level to be effective to minimize capillary rise and provide wicking drainage.
2. The wicking geotextile can provide an alternative solution for the cement treated subgrade to mitigate high groundwater-induced problems.
3. For the AB-1 aggregate and the AB-3 aggregate, the minimum effective wicking distance of the wicking geotextile is 12 in. (0.3 m).

The following recommendations can be made for future studies:

1. Since the control section in this study had different cross sections from the test sections with the wicking geotextile, it was challenging to make direct comparisons. Future studies may adopt the same cross pavement layers for the control section as the test section with the wicking geotextile.
2. This study was focused on the variations of water contents in subgrade and base courses. The benefits of moisture reduction in these layers to the improved structural capacity and performance of pavements should be evaluated.
3. The monitored data may be used to develop a design method to quantify the amount of water content reduction using the wicking geotextile.
4. The monitored data may also be used to verify design methods for the wicking geotextile for pavement applications to be developed in the future.

References

American Association of State Highway and Transportation Officials (AASHTO). (1993). *Guide for design of pavement structures*.

ASTM D6433-18. (2018). *Standard practice for roads and parking lots pavement condition index surveys*. ASTM International. doi: https://doi.org/10.1520/D6433-18, www.astm.org

Azevedo, M. M. D. (2016). *Performance of geotextiles with enhanced drainage* (Doctoral dissertation). University of Texas at Austin. doi: https://repositories.lib.utexas.edu/bitstream/handle/2152/72484/AZEVEDO-DISSERTATION-2016.pdf

Connor, B. & Zhang, X. (2015). *Evaluate H2RI wicking fabric for pavement application*. (Report No. 2013-S-UAF-0026). University of Alaska. doi: http://hdl.handle.net/1773/43553

Dawson, A. (2009). *Water in road structures: Movement, drainage, and effects*. Springer Netherlands.

Federal Highway Administration (FHWA) (1992). *Demonstration project 87: Drainage pavement systems* (Publication No. FHWA-SA-92-008). [Participant notebook].

Galinmoghadam, J., & Zhang, X. (2020). Use of wicking fabric to reduce pavement pumping. In *Geo-Congress 2020*: *Geotechnical Earthquake Engineering and Special Topics* (GSP 318 pp. 630-639). American Society of Civil Engineers. doi: https://doi.org/10.1061/9780784482810.065.

Guo, J. (2017). *Evaluation and design of wicking geotextile for pavement applications* (Doctoral dissertation). University of Kansas. http://hdl.handle.net/1808/27800

Guo, J., Han, J., & Zhang, X. (2019a). Large-scale rainfall simulation and cyclic plate loading test of wicking geotextile-stabilized base. In *Geo-Congress 2019*: *Geotechnical Materials, Modeling, and Testing* (pp. 824-832). American Society of Civil Engineers. doi: https://doi.org/10.1061/9780784482124.083

Guo, J., Han, J., Zhang, X., & Li, Z. (2019b). Evaluation of moisture reduction in aggregate base by wicking geotextile using soil column tests. *Geotextiles and Geomembranes*, *47*, 306-314. doi: 10.1016/j.geotexmem.2019.01.014.

Guo, J., Han, J., Zhang, X., & Li, Z. (2021). Experimental evaluation of wicking geotextile-stabilized aggregate bases over subgrade under rainfall simulation and cyclic loading. *Geotextiles and Geomembranes, 49(6),* 1550-1564. doi: 10.1016/j.geotexmem.2021.07.004.

Guo, J., Wang, F., Zhang, X., & Han, J. (2017). Quantifying water removal rate of a wicking geotextile under controlled temperature and relative humidity. *Journal of Materials in Civil Engineering*, *29(1)*, *04016181*. doi: 10.1061/(ASCE)MT.1943-5533.0001703.

Han, J. (2015). *Principles and practice of ground improvement*. John Wiley & Sons.

Han, J. & Zhang, X. (2014, August). Recent advances in the use of geosynthetics to enhance sustainability of roadways. In *20th International Conference on Advances in Civil Engineering for Sustainable Development* (pp. 29-39). Suranaree University of Technology Nakhon Ratchasima, Thailand.

Han, J., Zhang, X., & Guo, J. (2018, February). Improving roadway performance by wicking geotextile to reduce soil moisture. In J. F. Labuz & J. Skiles (Eds.), *Proceedings of the University of Minnesota 66th Annual Geotechnical Engineering Conference* (pp. 67-81).

Kansas Department of Transportation (KDOT). (2007). Section 1107: *Standard specifications for state road & bridge construction.*

Lin, C., Presler, W., Zhang, X., Jones, D., & Odgers, B. (2017). Long-term performance of wicking fabric in Alaskan pavements. *Journal of Performance of Constructed Facilities, 31*(2), D4016005. doi: 10.1061/(ASCE)CF.1943-5509.0000936.

Lin, C., & Zhang, X. (2018). Laboratory drainage performance of a new geotextile with wicking fabric. *Journal of Materials in Civil Engineering, ASCE, 30*(11), 04018293. doi: 10.1061/(ASCE)MT.1943-5533.0002476.

Lin, C., Zhang, X., & Han, J. (2019). Comprehensive material characterizations of pavement structure installed with wicking fabrics. *Journal of Materials in Civil Engineering, 31*(2), 04018372. doi: 10.1061/(ASCE)MT.1943-5533.0002587.

Lin, C., Zhang, X., & Presler, W. (2015). *Application of wicking fabric to reduce damage in Alaskan pavements*. Final Project Report to TenCate Geosynthetics (North America), Alaska University of Transportation Center, University of Alaska Fairbanks. doi: https://www.tencategeo.us/media/9479d4ed-ffd8-4d09-85bc-9e6961599aa6/_yZIqg/TenCate%20Geosynthetics/Documents%20AMER/Industry%20Papers/2015-%20Application%20of%20Wicking%20Fabric%20To%20Reduse%20Damage%20In%20Alaskan%20Pavements.pdf.

Miller, J. S., & Bellinger, W. Y. (2014). *Distress identification manual for the Long-Term Pavement Performance Program*. (Report No. FHWA-HRT-13-092). Federal Highway Administration.

National Cooperative Highway Research Program (NCHRP). (2004). *Guide for mechanistic-empirical design of new and rehabilitated pavement structures*.

Powell, W. D., Potter, J. F., Mayhew, H. C., & Nunn, M. E. (1984). *The structural design of bituminous roads*. (TRRL Report LR 1132). Transport and Road Research Laboratory.

Ragnoli, A., De Blasiis, M. R., & Di Benedetto, A. (2018). Pavement distress detection methods: A review. *Infrastructures, 3*(4)*,* 58, 1-19. doi: 10.3390/infrastructures3040058.

Rokade, S., Agarwal, P. K., & Shrivastava, R. (2012). Study on drainage related performance of flexible highway pavements. *International Journal of Advanced Engineering Technology, 3*(1)*,* 334–337.

Shahin, M.Y. (1994). *Pavement management for airports, roads, and parking lots*. (2nd ed.). Springer.

Sikkema, M., & Carpita, J. B. (2014). Wicking geosynthetic used for frost heave prevention Pioneer Mountain Scenic Byway. In *Proceedings of the* 65th *Highway Geology Symposium*. Highway Geology Symposium.

TenCate (2015). *Mirafi H2Ri woven geosynthetic specifications*. Accessed May 1, 2021. doi: https://www.tencategeo.us/media/39ff27e9-96f5-4450-9aaa-bd9c1cce3160/yV_goA/TenCate Geosynthetics/Documents AMER/Product Description Sheets/Woven Product Description Sheets/PDS_H2Ri0417.pdf.

Wang, F., Han, J., Zhang, X., & Guo, J. (2017). Laboratory tests to evaluate effectiveness of wicking geotextile in soil moisture reduction. *Geotextiles and Geomembranes, 45*(1)*,* 8-13. doi: 10.1016/j.geotexmem.2016.08.002.

Webster, S. L., Brown R. W., & Porter, J. R. (1994). Force projection site evaluation using the electrical cone penetrometer (ECP) and the dynamic cone penetrometer (DCP). In *Proceedings of 4th International Conference on the Bearing Capacity of Roads and Airfields*. the University of Minnesota.

Webster, S. L., Grau, R. H., & Williams, T. P. (1992). *Description and application of dual mass dynamic cone penetrometer* (Report No. GL-92-3) [Instruction Report]. U.S. Army Corps of Engineers.

Yuan, H. (2017). *Effectiveness of wicking geotextile in mitigating freeze-thaw problems of aggregate bases with fines* (Master's thesis). University of Kansas. doi: http://hdl.handle.net/1808/25933.

Zhang, X., & Galinmoghadam, J. (2020). *Performance of wicking geotextile on mitigating water pumping issue on I-44 Highway* (Report no. cmr 20-003). Missouri Department of Transportation.

Zhang, X., Presler, W., Li, L., Jones, D., & Odgers, B. (2014). Use of wicking fabric to help prevent frost boils in Alaskan pavements. *Journal of Materials in Civil Engineering, 26*(4)*,* 728-740. doi: 10.1061/(ASCE)MT.1943-5533.0000828.

Zornberg, J. G., Azevedo, M., Sikkema, M., & Odgers, B. (2017). Geosynthetics with enhanced lateral drainage capabilities in roadway systems. *Transportation Geotechnics, 12*, 85-100. doi: 10.1016/j.trgeo.2017.08.008.

K-TRAN

KANSAS TRANSPORTATION RESEARCH AND NEW-DEVELOPMENT PROGRAM

AD ASTRA PER ASPERA

Kansas

Department of Transportation